

# **Tectonic Deformation in the Santorini Volcanic Complex (Greece) as Inferred by Joint Analysis of Gravity, Magnetotelluric and DGPS Observations**

A. Tzanis, S. Chailas, V. Sakkas and E. Lagios

*Section of Geophysics, Department of Geology and Geoenvironment,  
National and Kapodistrian University of Athens,  
Panepistimiopolis, Zografou 157 84, Greece*

**Corresponding Author:** Andreas Tzanis, [atzanis@geol.uoa.gr](mailto:atzanis@geol.uoa.gr)

Athens, September 2019

## ABSTRACT

Tectonic activity is very difficult to study in the Santorini Volcanic Complex as it comprises a cluster of small/awkwardly shaped islands covered by pyroclastic deposits from which tell-tale markers are swiftly erased, while seismicity is generally absent. We address the problem by combining geophysical exploration methods to evaluate the long-term effects of tectonic deformation and time-lapse differential GPS to directly evaluate the magnitude and kinematics of present-day deformation. The former comprise 3-D gravity modelling to investigate the footprint of tectonics on the pre-volcanic Alpine basement and natural-field EM induction to map conductivity anomalies epiphenomenal to fluid circulation in faults. Our analysis identified the following principal tectonic elements:

The *Trans-Santorin Divide* (TSD), a segmented NNW-SSE dextral strike-slip fault splitting the SVC sideways of the line joining Cape Exomytis, the Kammeni Islets and the Oia–Therassia Strait. It is collocated with a major vertical conductive zone and forms a series of dents and depressions in the basement. The *Columbo Fault Zone* (CFZ) is a pair of parallel NE-SW sub-vertical normal-sinistral faults straddling the northern SVC and terminating against the TSD; it may be associated with fluid injection into the shallow crust but appears to have limited effect on crustal conductivity (compared to TSD). The *Anhydros Fault Zone* (AFZ) is detected by its footprint on the basement, as a set of parallel northerly dipping NE-SW faults between the Athinios–Monolithos line and Fira. If it has any heave, it is left-lateral. It does not have distinguishable electrical signature and does not contribute to present-day horizontal deformation. The CFZ and AFZ are antithetic and form a graben containing the volcanic centre of Kammeni Islets.

E-W extension was identified lengthwise of a zone stretching from Cape Exomytis to Athinios and along the east flank of the caldera to Imerovigli. N-S normal faulting confirmed therein, may have contributed to the localization of the east caldera wall. NNE-SSW compression was observed at SW Thera; this may have produced E-W failure and contributed to the localization of the south caldera wall. The footprint of the caldera on the basement is a parallelogram with N-S long and WNW-ESE short dimensions: if the east and south flanks collapsed along N-S normal and E-W inverse failures, then the west and north flanks may have formed analogously. Present-day deformation is localized on the TSD and CFZ: this can only be explained if the former is the synthetic (dextral) Riedel-R shear and the latter the antithetic (sinistral) Riedel-R' shear, generated by N-S  $\sigma_1$  and E-W  $\sigma_3$  principal stress axes. Accordingly, NW-SE right-lateral shearing of the broader area is expected and indicated by several lines of indirect evidence. The geographic extent of this shearing and its role in the regional tectonics of the south Aegean remains to be confirmed and appraised by future research.

Contemporary volcanic centres develop at the interface of the TSD with the CFZ/AFZ graben; volcanism appears to be controlled by tectonics and the SVC to be shaped by tectonic rather than volcanic activity.

## 1. Introduction

The Santorini Volcanic Complex (SVC) is located in the middle of the Hellenic (or Aegean) Volcanic Arc that develops ad retro of the Hellenic Trench; it is located approximately 110km above the subduction of the African oceanic crust beneath the Aegean plate (Fig. 1a), in an area characterized by high-rate extension and severe crustal thinning. The SVC is the central and most significant component of the Santorini Volcanic Field (SVF) that also includes the Christiana and Columbo submarine volcanoes, respectively located to SW and NE of the SVC (Fig. 1b).

As seen in Fig. 1b, the SVF formed along the axis of the Anhydros basin, a NE-SW oriented graben developing between Amorgos Island and the Christiana islets. The SE flank of Anhydros basin is defined by the NE-SW Anhydros Fault Zone (AFZ), which comprises the marginal fault system of a significant basement horst called the Santorini–Amorgos Ridge (Perissoratis 1995). The south-eastern quarter of the SVC, in Thera Island, is dominated by the presence of outcropping basement rocks and comprises part of the Santorini-Amorgos Ridge; the rest of the SVC lies in Anhydros basin. If extrapolated to the SW, the AFZ passes through the Santorini caldera; a branch straddling the centre of the caldera is known as the Kammeni Line and has been associated with NE-SW surface faulting, vent alignment and gas emission (Heiken and McCoy, 1984; Druitt et al., 1989, 1999; Parks et al., 2013). A second tectonic lineament associated with Anhydros basin is the NE-SW Columbo Fault Zone (CFZ, e.g. Druitt et al, 1989, 1999; Mountrakis et al., 1998); it extends along the line Columbo volcano – north Thera where it is defined by a series of cinder cones, tuff rings and NE-SW oriented dykes. Both the AFZ and CFZ were interpreted to comprise major normal fault zones (e.g. Pe-Piper and Piper, 2005) and to have been of primary importance in the development of the SVC. Notably, the largest part of contemporary shallow earthquake activity appears to take place with normal faulting along the Columbo FZ and be sparse elsewhere (Delibasis et al., 1989; Drakopoulos et al., 1996; Bohnhoff et al., 2006; Kolaitis et al., 2007; Dimitriadis et al., 2009), while the bulk of seismic activity associated with the 2011-2012 unrest was concentrated in a short segment of the Kammeni line (Feuillet, 2013; Papadimitriou et al., 2015).

The picture emerging from the above summary is that the SVF is controlled by the apparently extensional tectonics of the Anhydros basin. Based on morphological evidence from shallow seismic profiles and swath bathymetry, Sakellariou et al. (2010) propose that the AFT and CFZ have right-lateral heave. Also based on the short strand exposed at north Thera, other authors also suggest that the CFZ has right-lateral heave (Druitt et al., 1999; Mountrakis et al., 1998; Dimitriadis et al., 2009). However, a series of time-lapse DGPS measurements conducted between 1994 and 2005 revealed a considerably more complex pattern of deformation during a period in which the volcano was inactive (Papageorgiou et al., 2007; Papageorgiou et al., 2010; Lagios et al., 2013): the displacement and velocity fields indicate aseismic, high-rate north-westerly displacement of the south-western half of the SVC (right-lateral motion in a NNW-SSE orientation). Given the rigour of the DGPS method, this evidence suggests that if NE-SW faults like the CFZ have any heave, then it *cannot* be right-lateral. Papageorgiou et al., (2010) went on to propose a model of contemporary tectonic deformation. Given that the neotectonics of the SVC appears to be more complex than generally appreciated, objective of this presentation is to clarify its nature and influence on the evolution of the SVC/SVF. To this effect a rigorous trans-disciplinary approach is implemented, based on different lines of geophysical and geodetic evidence. As will eventually be seen, the analysis will turn out to corroborate and refine the model of Papageorgiou et al. (2010), and also provide insight into why the SVC is the main focus of the SVF.

The geophysical evidence to be used comprises gravity and magnetotelluric observations and modelling.

Gravity data and 3-D modeling techniques shall be used to strip the gravity effect of pyroclastic and extrusive volcanic formations, so as to reconstruct the morphology of the basement and delineate markers of tectonic activity such as fault steps, grabens and horsts. Magnetotelluric data and techniques shall be used to map *epiphenomenal* conductivity anomalies associated with thermal fluid circulation which, in convective hydrothermal systems controlled by concurrent tectonic activity, usually takes place along active faults. A more detailed justification of the applicability of gravity and magnetotelluric methods can be found in Section S1 of the Supplementary Material.

Ground deformation in back-arc volcanoes is associated with tectonic and volcanic processes, namely regional and local scale faulting and/or magma motion. In a heavily tectonized and rapidly deforming crust like that of the south Aegean, when a volcano reposes, large-scale ground deformation is largely the result of tectonic activity while, as will be confirmed herein, fluid transfer in the hydrothermal system with/without self-sealing processes may also contribute. During paroxysmal periods, magmatic processes assume the primary role and large-scale deformation may serve as a precursor to eruptions: the surface is expected to dilate or contract in response to inflationary or deflationary changes in the magma chamber or the emplacement of dykes at the upper echelons of the volcanic field (preferentially occurring along faulting structures). The study of ground deformation may assist in understanding the interplay between tectonic and volcanic processes and provide additional insights into volcanic hazards.

A very accurate tool of monitoring three-dimensional ground deformation is Differential GPS (DGPS): the method is able to resolve absolute or relative displacements of the surface of the Earth with nearly sub-millimetric precision. Applications along the Hellenic Volcanic Arc and the SVC have been numerous and tell-tale (e.g. Lagios et al., 2005; Papageorgiou et al., 2010; Newman et al., 2012; Lagios et al., 2013; Papoutsis et al., 2013; Lagios et al., 2017; references therein). The time-lapse DGPS measurements used herein comprise the longest standing relevant experiment, as they span the period 1994 – 2017 and three phases of the contemporary history of the SVC: before, during and after the 2011–2012 period of unrest (see below). Interim results for the period 1994–2005 have been presented by Papageorgiou et al., (2010) in a context similar to that reported herein, but based on a different processing scheme. Results for the period 1994–2012 have been presented by Lagios et al., (2013) albeit in a different context and style. Herein, we make use of the 1994–2012 data but present it in abbreviated form and in a style suitable for this analysis. We also include DGPS measurements up to the spring of 2017, so as to demonstrate how the SVC crust is recovering from the 2011–2012 unrest. Nevertheless, we emphasize on the period 1994–2005 by calculating and interpreting the strain field, which turns out to be much more informative than displacement or velocity fields, and also confirm our finding by modelling the displacement field with the “GTdef” algorithm (Chen et al. 2009; Feng et al. 2012).

Overall, we demonstrate how the joint analysis of three very different data sets highlights their common causative factor, i.e. local tectonics. We propose a model that demonstrates the influence/control of tectonic processes on the evolution of the SVC and at the same time demonstrate the necessity of using trans-disciplinary approaches in understanding Earth processes.

## **2. Geology, Volcanism and Tectonics**

The SVC comprises five islands: Thera, Therassia and Aspronisi which are arranged as a dismembered ring around a flooded caldera, and Palaea and Nea Kammeni, the post-caldera volcanic centres in which most of the present-day activity is concentrated (Fig. 2). Volcanic activity is dated to at least 1.6Ma BP (Ferrara et al., 1980) and takes place at those parts of the SVC, which lay in the Anhydros basin (see Introduction for details).

The volcanic evolution of the SVC comprises six main stages (Druitt et al., 1989). The early centres of Akrotiri peninsula were followed by the cinder cones of Akrotiri Peninsula; submarine tuffs and tuffites outcropping in SW Thira yield early Quaternary ages (Ferrara et al., 1980; Seidenkrantz and Friedrich, 1993). Subaerial large-scale effusive activity has taken place after 650Ka BP and continues to the present; it includes the Peristeria Volcano followed by the products of a first and second eruptive cycle and, finally, the Kammeni shield. Each eruptive cycle lasted for approximately 180Ka and is generally distinguished on the basis of long-term differentiation in magma composition, beginning with eruption of mafic to calc-alkaline magmas and ending with a major rhyodacitic explosion accompanied by caldera collapse. Over one hundred explosive eruptions have taken place during the last 360Ka (first and second eruptive cycles); twelve of which were Plinian of intensity. Each Plinian eruption discharged volumes of a few to several cubic kilometres and all together formed pyroclastic deposits with a thickness of 200m (Druitt et al., 1989); their products also contain relics of at least five large shield volcanoes. The intervals between the twelve Plinian eruptions vary between 17Ka and 40Ka, averaging to 30Ka. The explosive activity triggered at least four caldera collapses and resulted in the formation of the present-day composite caldera structure (Druitt and Francaviglia, 1992), which is bordered by cliffs as high as 300m and extends to at least 400m below sea level. The last caldera-forming explosion was the renowned Minoan eruption of the late Bronze Age (1645–1500 BCE), which ejected about 30km<sup>3</sup> of dense-rock equivalent material according to Pyle (1990) and over 60km<sup>3</sup> according to Sigurdsson et al., (2006); the vent was located in the vicinity of the Kammeni Islets (Bond and Sparks, 1976). Following the Minoan eruption, volcanic activity was localised in the intra-caldera area with extrusive, effusive and mildly explosive events that produced dacitic lava domes and pyroclastic flows and erected the Palaea- and Nea Kammeni edifices between 197 BCE and 1950 CE (Fouqué, 1879; Washington, 1926; Ktenas, 1927; Reck, 1936; Georgalas, 1953; Georgalas and Papastamatiou, 1953): Palaea and Nea Kammeni islets are subaerial expressions of a submarine dacitic shield measuring approx. 2 km<sup>3</sup> in volume.

The structure of the caldera and its post-Minoan evolution has recently been investigated with marine geophysical surveys. Sakellariou et al., (2012) compare the intra-caldera data with the seismic stratigraphy of Minoan deposits on the seafloor around the island group and indicate that the thickness of the Minoan deposits may locally exceed 100m, although post-Minoan deposits appear to have negligible thickness. Finally, they argue that the Minoan eruption centre was collocated with the present-day Kammeni Islets. Johnston et al., (2015) propose the existence of three distinct volcanoclastic units: modern infilling sediments underlain by shallow marine volcanics associated with the formation of the Kammeni Islets and, finally, down-faulted Minoan pyroclastics deposited during the caldera collapse. Nomikou et al. (2016) argue that the caldera basin was lagoonal and not open to the sea during the main phases of the Minoan eruption, but was flooded right afterwards generating a tsunami due the entry of pyroclastic flows into the sea combined with slumping of submarine pyroclastic accumulations; the inflow of sea water and associated landslides cut a deep, approximately N330° submarine channel located along the strait between Oia and Therassia, which filled the caldera in less than two days while later stage submarine landslides breached the SW walls around Aspronisi islet. Finally, Hooft et al., (2019) generated an intermediate resolution 3-D passive tomographic image of caldera interior, in which the magma chamber responsible for the 2011-2012 crisis is clearly outlined.

The evolution of contemporary volcanic centres in the SVC were profoundly influenced by two NE-SW faults, the Kammeni Line and Columbo Fault Zone respectively (see Introduction). This concerns not only the Kammeni Shield and Islets, but also the submarine Columbo Volcano, located approx. 7 km NE of Cape Columbo (Figs. 1 and 2 respectively). Six pre-historic Plinian eruptions align with the Kammeni

Line, as also do the historic subaerial vents of the Kammeni islets. Independent volcanic centres at North Thera, as is the Megalo Vouno cinder cone, the Kokkino Vouno cinder cone and the Cape Columbo tuff ring define the Columbo Fault (Fouqué, 1879; Reck, 1936). In addition, several dykes located at northern Thera, have a NE-SW orientation, as for instance the one between Mikros Prof. Elias and Megalo Vouno (Heiken and McCoy 1984; Mountrakis et al., 1998). Practically all of the post-Minoan volcanic activity in the SVC takes place between the Kammeni Line and CFZ and is limited to an elongate, 600m-wide zone of N65° apparent strike. This zone was initially associated with the Kammeni Line but its width and orientation seems to have been drafted on the basis of sea-bottom morphology and a single sparker profile (Perissoratis, 1990, 1995); as will be seen, this evidence was incomplete and somewhat misleading. In any case, the strike of the Kammeni Line has been revised and in recent literature it is generally identified with that of the Anhydros FZ (e.g. Sakellariou et al., 2010; Nomikou et al., 2012; Papadimitriou et al., 2015). In Fig. 2, the Kammeni Line has been collocated with the surface projection of the fault segment activated during the 2011-2012 unrest (see Papadimitriou et al., 2015). In the rest of the intra-caldera area, recent marine geophysical research has not detected traces of faulting other than those related to the collapse.

Direct evidence of faulting with strike different than that of the Anhydros basin is found in both geological maps of the SVC (Pichler et al., 1980; Druitt et al., 1999) and is reproduced in Fig. 2. The faults comprise short strands with a general NW-SE orientation, observable mainly at South Thera and on the walls of the caldera. A significant N330° depression between North Thera and Therassia, (the flooding channel of Nomikou et al., 2016), has been considered to bear evidence of normal faulting (IGME, 1995; Perissoratis, 1995), although it has also been interpreted to be an extended NW-SE dyke (Pichler and Kussmaul, 1980), or the result of rotational slumping (Heiken and McCoy, 1984). Papageorgiou et al., (2010) and Lagios et al., (2013) detect aseismic right-lateral motion along an approximately N330° interface located lengthways of the line joining Cape Exomitis – Vlychada in the south, the Kammeni Islets in the centre and the Oia – Therassia strait (flooding channel) in the north. Papageorgiou et al., (2010) dubbed this feature surface “Santorini Fault Zone”, but as it turns out to be the only dislocation surface traversing the entire SVC it will henceforth be referred to as the *Trans-Santorini Divide* (TSD) and will be a focal point of the present study.

As mentioned above, earthquake foci in the vicinity of the SVC are concentrated around the Columbo volcano (Delibasis et al., 1989; Drakopoulos et al., 1996; Bohnhoff et al., 2006; Kolaitis et al., 2007; Dimitriadis et al., 2009; Papadimitriou et al., 2015). The seismotectonic analysis of Columbo earthquakes yielded an extensional stress field of NE-SW orientation (Dimitriadis et al., 2009); this is consistent with the general disposition of Anhydros basin and the focal mechanism of the largest earthquake observed in the South Aegean in the 20<sup>th</sup> century, the  $M_s \approx 7.5$  Amorgos earthquake of 9 July 1956 (Okal, 2009). Earthquakes with foci located within the SVC have always been extremely sparse and continue to be so (see Institute for the Study and Monitoring of Santorini Volcano, <http://www.santorini.net/ismosav>). The only case of systematic micro-earthquake activity recorded within the SVC was during the 2011-2012 volcano-tectonic unrest. During this event, a magma volume of 7–12 Mm<sup>3</sup> was injected at depths of 4–6 km beneath the North Basin of the caldera, with epicentre located on (25.389°E, 36.426°N), approximately 2km north of Nea Kammeni (Lagios et al., 2013). This resulted in significant dilation and radial centrifugal deformation of the northern SVC crust, measuring 30–65mm in both the horizontal and vertical directions (Lagios et al., 2013; Fomelis et al., 2013; Newman et al., 2012). The event was also accompanied by elevated thermal fluid and gas emission (e.g. Parks et al., 2013; Tassi et al., 2013). Earthquakes have been confined to a short and narrow belt along and to the north of the Kammeni Line

trace shown in Fig. 2, and have been intensively studied by several authors (Vallianatos et al., 2013; Konstantinou et al., 2013; Kaviris et al., 2015 and others). In particular, Papadimitriou et al. (2015) have published a very detailed analysis that included 131 individual and nine composite focal mechanisms; the (presumed) NE-SW focal planes of these events are generally sub-vertical and exhibit right-lateral, oblique-normal kinematics. From a tectonics point of view, this result adds to the complexity of assessing present deformation in the SVC, as it appears to be inconsistent with the apparently right-of lateral kinematics the TSD: an interpretation of its origin shall be attempted herein.

### 3. Gravity Observations

Several local gravity surveys have been carried out in the Santorini Volcanic Complex during the past four decades (Fig. 3). The data used herein was compiled by assembling data sets from different sources, re-evaluating it when necessary, homogenizing and commonly referencing to the ISGN71 datum, so as to render them all comparable and compatible for joint analysis. The data include 50 land stations from Yokoyama and Bonasia (1971, 1979), 208 land stations from Budetta et al., (1984), 191 land stations from Vasiliadis (1985), 88 land stations measured by the Authors (UA) and a large number of offshore measurements from the GEODAS data base (NGDC, 2012); gaps between GEODAS measurements were filled using the EGM2008 satellite gravity model computed up to degree 2160 (Pavlis et al. 2008). Detailed information about the primary data and the re-evaluation and homogenization procedures can be found in Section S2 of the Supplementary Material.

The Bouguer anomaly map is shown in Fig. 4. At southwest Thera, it exhibits two elongate ridges clearly configured in the NE-SW and NW-SE directions and exactly correlated with the outcropping pre-volcanic basement. These are flanked by gravity lows at central Thera (to the NW) and Akrotiri peninsula (to the west). The amplitude of the gravity anomalies drops at rates of 4.8 mGal/km to the NW and 5.8 mGal/km to the west, indicating abrupt thickening of the pyroclastic overburden parallel to these directions. Moreover, the orientation and quasi-linear character of these changes are indicative of tectonic origin: the high gravity gradients are approximately collocated with the onshore extensions of major tectonic features mapped by several researchers (Sakellariou et al., 2010; Alexandri et al., 2003; IGME, 1995, and others). The structure of the caldera area is apparently complex. Along the perimeter, one observes a series of local positive anomaly highs (positive valued surfaces with locally positive curvature), possibly indicating the presence of buried Alpine basement formations or remnants of the Skaros and Therassia shields at the east and west of the Kammeni islets (see Budetta et al., 1984). One may also observe local negative highs (negative valued surfaces with locally positive curvature); these appear to be associated with outcropping or/and buried volcanic formations with densities considerably lower than  $2.67\text{g/cm}^3$ , as in the areas of Faros-Akrotiri (Akrotiri volcano) and Mikros Prof. Elias (Peristeria volcano). The interior of the caldera exhibits a SSE-NNW oriented series of local gravity lows (with negative curvatures) extending between the foot of Akrotiri peninsula, the Kammeni islets and the channel (strait) separating Thera from Therassia. Notably – and notwithstanding the lack of rigorous constraints in the North and South basins – the configuration of the anomalies within the caldera is complex and indicates that they have been shaped by synergy of volcanic and tectonic processes.

#### 3.1. Rock Densities and Modelling Procedure

Pyroclastic Formations: Dry density values of Santorini pumice formations have been published by Whitham and Sparks (1986), Adams (1987), Wilson and Houghton (1990), Gardner et al. (1996), Urbanski (2003) and Boyce and Gertisser, (2012); they are generally well under  $1\text{g/cm}^3$ . To complicate

things, Boyce and Gertisser (2012) have shown that pumice densities change with the degree of welding and distance from the source, varying from  $2.2\text{g/cm}^3$  for well welded samples found at distances less than 250m, to as low as  $0.58\text{g/cm}^3$  for un-welded samples found at distances longer than 4km. Measurements conducted on scorias by Adams (1987), Mellors and Sparks (1991) and Gardner et al. (1996) yield an average of  $1.5\text{g/cm}^3$ . As above, the distribution of density is inhomogeneous and considerably higher values have been obtained for some localities: Adams (1987) reports  $2\text{g/cm}^3$  in some pyroclastic breccia and  $2.5\text{g/cm}^3$  in the ignimbrites of the Middle Pumice series of Thera, while Mortazavi and Sparks (2004) report a mean value of  $2.18\text{g/cm}^3$  for the Akrotiri mafic inclusions.

Non-Pyroclastic Formations: Only two sources have been found in the literature and they are only concerned with the dacites of the Kammeni Islets (Shorin, 1980; Briquet and Lancelot, 1984). Both report a broad range of densities reflecting different degrees of hydrothermal alteration. Overall, a density of  $2.4\text{-}2.5\text{g/cm}^3$  can be assumed for the unaltered or slightly altered dacitic material. The dearth of data from non-pyroclastic formations compelled us to conduct direct measurements on samples taken from the Alpine basement and extrusive volcanic formations. The distribution of sampling locations is shown in Fig. 3. Ten large-sized samples were collected in the vicinity of each site and their density was estimated on the basis of the Archimedes principle. The results were grouped according to their source (lithological) formation and the means and standard deviations for each formation are shown in Table 1. It should be borne in mind that density measured on individual samples does not necessarily represent the bulk properties of a geological formation, with particular reference to calc-alkaline rocks due to their emplacement process (high and heterogeneous crack and fracture density) and chemical alteration (heterogeneous distribution of argillization). Accordingly, the values shown in Table 1 should be taken to comprise upper limits.

Modelling was performed with an unpublished algorithm developed by S. Chailas. In this approach, buried three-dimensional geological bodies are approximated by polyhedra of polygonal cross-section, and their gravity effect is calculated by the method of Radhakrishna Murthy et al., (1989, 1990). Because any polyhedron can be defined by an upper and lower boundary surfaces, the shape of any geological body can be determined by using prior information to fix one of the surfaces while adjusting the other. Surface topography, borehole data, other geophysical surveys and surface geology are some obvious sources of prior information. The adjustment of the boundary surface(s) is automated by an iterative procedure derived from Bott (1960). Letting  $\hat{\mathbf{g}}$  denote the matrix of observed gravity anomalies,  $\mathbf{g}(k)$  the matrix of calculated gravity anomalies at the  $k^{\text{th}}$  iteration and  $\Delta\mathbf{g}(k) = \hat{\mathbf{g}} - \mathbf{g}(k-1)$  the corresponding residual anomalies, the adjusted boundary surface  $\mathbf{Z}(k)$  is modified according to the scheme

$$\mathbf{Z}(k) = \mathbf{Z}(k-1) - \frac{\Delta\mathbf{g}(k)}{2\pi G \Delta\rho} \circ \mathbf{W}_Z, \quad k = 2, 3, \dots,$$

where,  $G$  is the universal gravitational constant,  $\Delta\rho$  is the density contrast across  $\mathbf{Z}(k)$ ,  $\mathbf{W}_Z$  is a user-defined matrix of weights and  $\circ$  denotes the Hadamard product. The iterative procedure aims at minimizing the objective function

$$\sum \sum (\hat{\mathbf{g}} - \mathbf{g})^2 \circ \mathbf{W}_G,$$

where  $\mathbf{W}_G$  is a user-defined matrix of weights. The elements of  $\mathbf{W}_Z$  and  $\mathbf{W}_G$  are either 0 or 1. It is thus possible to keep  $\mathbf{Z}(k)$  fixed wherever prior information exists and to isolate and study specific gravity anomalies.

Based on Section 3.1 and Table 1, we assumed that the geological formation densities are uniform, with sea water having  $1\text{g/cm}^3$ , pyroclastic deposits  $1.35\text{g/cm}^3$ , volcanic rocks  $2.3\text{g/cm}^3$  and the Alpine

basement  $2.7\text{g/cm}^3$ . The elements of matrix  $\mathbf{W}_G$  were set to unity throughout. The analysis was carried out in two stages. The first involved stripping of the pyroclastics layer: the upper boundary surface  $\mathbf{Z}_U^{(1)}$  represents the topography and bathymetry (elevation) and could therefore be fixed, while the lower boundary surface  $\mathbf{Z}_L^{(1)}$  was allowed to vary. Moreover, by appropriately structuring the weight matrix  $\mathbf{W}_Z$ , the thickness of the pyroclastic layer  $\mathbf{Z}_U^{(1)} - \mathbf{Z}_L^{(1)}$  was kept fixed and equal to zero at the outcrops of the Alpine basement and volcanic extrusives, while in south Thera,  $\mathbf{Z}_L^{(1)}$  was also constrained by data from boreholes that have penetrated through to the ceiling of the Alpine basement (Fytikas, 1989). The second stage involved stripping of the volcanic rock “layer”. In this case, the output of the first stage, i.e. the lower surface of the pyroclastic layer, was taken to comprise the *fixed* upper surface:  $\mathbf{Z}_U^{(2)} = \mathbf{Z}_L^{(1)}$ . The thickness  $\mathbf{Z}_U^{(2)} - \mathbf{Z}_L^{(2)}$  was again fixed and equal to zero at the outcrops of the Alpine basement, as well as in the vicinity of borehole locations. The final surface  $\mathbf{Z}_L^{(2)}$  was taken to represent the topography of the pre-volcanic Alpine basement, although it may actually comprise the surface of a mosaic of true Alpine and dense ( $\geq 2.7\text{g/cm}^3$ ) igneous rock formations.

The modelling procedure was rather successful, with the second stage analysis yielding a final RMS error of 0.65 mGal, a fractional error of only 5.1% and goodness of fit  $R^2 = 0.96$ . A detailed evaluation of the quality of the model is presented in Section S3 of the Supplement. It should also be noted that due to relative paucity of data, the resolution of surfaces  $\mathbf{Z}_L^{(1)}$  and  $\mathbf{Z}_L^{(2)}$  is marginal in the North Basin although interpretation is still possible due to the relatively coarse discretization scheme. Conversely,  $\mathbf{Z}_L^{(1)}$  and  $\mathbf{Z}_L^{(2)}$  are *not* constrained in the West and South Basin and it is not easy to interpret them with confidence.

### 3.2 Results

Fig. 5a illustrates surface  $\mathbf{Z}_L^{(1)}$ , i.e. the topography of the sub-pyroclastic formations. Fig. 5b illustrates the topography of surface  $\mathbf{Z}_L^{(2)}$ , which we shall conventionally refer to as “the Alpine basement” or “bedrock”. Finally, Fig. 6 illustrates three cross sections that combine the two surfaces. The traces of known and interpreted faults are superimposed on all Figures 5 and 6; it is important to emphasize that the approximate location, geometry and kinematics of interpreted faults has been based on the *joint* analysis of gravity, magnetotelluric and DGPS data. Fig. 5 clearly indicates that the outline of the caldera forms an N-S oriented parallelogram. This geometry can be (and has been) inferred on the basis of surface topography and bathymetry, but has never been explained. Our analysis, by removing the masking effect of the pyroclastic/soft sediment and volcanic overburden, clarifies and pinpoints the boundaries of the “parallelogram” (caldera walls); it will be demonstrated that they are very likely controlled by local tectonics.

As evident in Fig. 5b, in the areas of Akrotiri peninsula, Kammeni islets, Mikros Prof. Elias – Columbo – Megalo Vouno, Therassia and Cape Riva the surface of the Alpine basement is punctuated with localized depressions centred on “sinks” that extend deeper than 1200m. These are interpreted to respectively mark the locations of the pipes and vents through which the Akrotiri, Kammeni, Peristeria, and Therassia–Cape Riva centres have erupted. In addition, an 800m “sink” can be observed in the North Basin, approximately 2km NW of Nea Kammeni and almost at the location at which Lagios et al., (2013) placed the (Mogi point) source of the 2011-2012 unrest. Although this part is not densely covered by gravity observations, the coincidence is still worth noting. Another interesting observation in Fig. 5b is of the presence of “Alpine basement” below southern Therassia. This is consistent with observations of abundant basement fragments from both the Minoan and Cape Riva eruptions in the pyroclastic deposits

of NW Santorini, which suggest the presence of basement near the surface (Druitt, 2014). Note, however, that in Fig. 5b the “basement” also appears to crop out at the base of the cliffs, although there’s no direct evidence to this effect. Because the surface  $\mathbf{z}_L^{(2)}$  in that area is associated with significant residuals (Section S3 of the Supplement), the *apparent* lateral extent of the “outcrop” is probably an artefact of the coarse discretization scheme and the moderate horizontal resolution afforded by the data. Alternatively, this “Alpine basement” may actually be the signature of dense calc-alkaline lavas of the second eruptive cycle, which do outcrop in that location.

A straightforward observation is that in the well-constrained part of central Thera, the sub-pyroclastic basement, which here is identified with the Alpine basement, exhibits a NE-SW trending graben-like structure bounded by the Anhydros Fault Zone (AFZ) to the south and the Columbo Fault Zone (CFZ) to the north. As can be seen in profile BC of Fig. 6, the AFZ appears to have produced a significant imprint by generating north-westerly stepwise depression of the Alpine basement. Notably, the onshore trace of the AFZ determined herein, almost exactly coincides with the continuation of the offshore trace of the AFZ as determined by Sakellariou et al., (2010). The CFZ comprises two major NE-SW oriented faults: the northern fault will henceforth to be referred to as the Cape Columbo Fault (CCF) and the southern fault to be referred to as the Mikros Prof. Elias Fault (MPEF). The approximate locations of these faults have been inferred by other authors who, however, either did not indicate a dip direction, or assumed that CCF is south-dipping and MPEF is north-dipping so as to form a graben between them (e.g. Druitt et al., 1999). The presence of these faults is manifest in the maps of Fig. 5, although they can hardly be identified in the profile BC (Fig. 6). In Section 5.4 we demonstrate that these are indeed present at the respective locations and that they are sub-vertical and south-easterly dipping: this dip direction may appear to be counterintuitive at first, but it is drawn on the basis of the DGPS analysis and as will be argued in Sections 5 and 6, it is the only alternative. It is apparent that the North Basin comprises an almost rectangular NE-SW depression, bounded and controlled by the CFZ – a NE-SW rectangle within a N-S parallelogram so to speak. Finally, one may observe a NE-SW depression between Fira and Imerovigli on one hand and Palea Kammeni on the other, which also includes volcanic pipes and vents: it forms right in the middle of the AFZ-CFZ graben and we interpret this to be the signature of the “Kammeni Line”.

Fault traces with different orientations have been mapped on the Alpine basement of SE Thera (Prof. Elias block): these are N-S, NE-SW, E-W, NW-SE and NNW-SSE. A significant N-S fault segment has been mapped on the western flank of Mt. Gavrilos; it appears to be normal with significant throw to the west. Our analysis not only shows that this segment continues northwards under the pyroclastic overburden, but that it can also be projected along the caldera wall to as far north, as Imerovigli. Indication of east-dipping N-S normal faulting also exists along the western flank of the caldera (marked CW1 and CW2 respectively). The presence of N-S normal faults implies the existence of an operative E-W extensional stress-field component which is confirmed by DGPS data analysis (Section 5.3). As will eventually be argued, the N-S normal faults may comprise second order discontinuities that guided the formation (collapse) of the eastern and western flanks of the caldera. In addition, the presence of E-W extension implies the presence of N-S compression and of *auxiliary* (second order) E-W inverse failure faults that may have contributed to the formation of the northern and southern flanks of the caldera. This point will be revisited and further discussed in Section 6. It is worth pointing out that E-W faults have been mapped on the southern flank of the Prof. Elias block but their sense of slip has never been clarified. Indication of a possible E-W discontinuity also exists along the northern flank of the Prof. Elias block (see below). The NW-SE (approximately N310°) orientation is a rather prominent morphological feature

of the SVC as it comprises the dominant orientational feature of the Alpine basement at SE Thera. The possible nature and significance of this feature will be discussed in Section 6 with the aid of additional observations.

Another prominent feature practically invisible on surface topography and bathymetry, is a series of depressions aligned in a NNW-SSE (approximately N330°) direction lengthwise of the zone joining the area of Vlychada/Cape Exomytis, the Kammeni islets and the Oia Strait (Fig. 5b). This coincides with the Trans Santorin Divide (TSD) of right-lateral dislocation proposed by Papageorgiou et al., (2010). The depressions can be observed both onshore, as in the foot of Akrotiri peninsula, and offshore associated with volcanic pipes and vents as in the Kammeni islets, in the North Basin (approximately 2km NW of Nea Kammeni and next to the source of the 2011-2012 unrest), and along the Oia Strait. The TSD appears to separate the SVC into northeast and southwest halves and is attributed to significant sub-vertical faulting structure(s), whose nature and origin will become apparent in Sections 4 and 5. It is also interesting to point out the existence of a N330° linear feature at north Thera, extending between the northern and southern faults of the CFZ and almost exactly coincident with the coastline and the root of Peristeria Volcano; this is also interpreted to comprise a NNW-SSE sub-vertical fault segment (see Section 5.4 for details). If this line is continued south-eastwards, it is brought to coincide with a fault segment of identical orientation mapped at the SE corner of the Prof. Elias block, near Kamari; this line appears to define the NE flank of the Prof. Elias block and, with synergy of the AFZ, separate the Prof. Elias and Monolithos blocks.

#### **4. Magnetotelluric observations**

The Magnetotelluric (MT) survey was conducted during the summer of 1993 and comprised a total of 37 soundings (Sotiropoulos et al, 1996a,b). Measurements were carried out in the nominal frequency bandwidth 128Hz-100s using Pb/PbCl<sub>2</sub> electrodes, CM11E induction coils and the Short Period Automatic Magnetotelluric system (SPAM) Mk III developed by G.J.K Dawes at the University of Edinburgh (Ritter et al., 1998). Given that SPAM enabled simultaneous multi-station data acquisition, the Magnetotelluric–Telluric measurement procedure was implemented, the physical basis of which is explained in Section S4 of the Supplement. Thus, data was acquired using a 5-component magnetotelluric configuration at one “*base*” and 2-component telluric configurations at multiple nearby “*satellite*” locations; this enabled calculation of impedance tensors at bases and satellites, and magnetic transfer functions at the bases. Given also that a shortage of induction coils prohibited application of remote referencing techniques for the suppression of noise, the estimation of impedance tensors and magnetic transfer functions was performed with the single-site robust statistical procedure of Junge (1990, 1992, 1994; also see Ritter et al., 1998). Robust algorithms may effectively downweight the influence of non-Gaussian noise provided that the population of noise-free data dominates the population of noisy data. Their performance progressively deteriorates as the rate of noise reception increases, and breaks down when the noise can effectively screen the magnetotelluric field. Moreover, single-site robust methods cannot cope with continuous coherent harmonic noise for obvious reasons. In such cases, noisy estimators were removed with a “low-tech” method, namely “expert judgment” and manual deletion.

Subsurface conductivities are high throughout the SVC, due to pervasive lateral sea-water infiltration and intense thermal fluid circulation and diffusion (see below). The resultant weak telluric fields, together with high levels of anthropogenic noise, had detrimental effects in spite of the robust procedure and with particular reference to periods longer than 1s. It turned out that impedance tensors could be estimated for only 18 base/satellite stations and magnetic transfer functions for only 11 bases. As shown in Fig. 7, these

are clustered in the remoter south-west and northern areas of Thera: 11 at the Akrotiri peninsula and 6 at the Oia – Cape Columbo. Data from only two other stations could be salvaged, one Nea Kammeni Islet and one near Vourvoulos. To make matters worse, the original data is damaged beyond recovery, thus eliminating any possibility of reprocessing with more advanced techniques. A rather typical example of observed response functions is presented in Section S6 of the Supplement. On the bright side, the pervasive sea water intrusion and overall low resistivities have prevented the development of an “island effect” since conductivity contrasts are rather low and ocean depths are modest around the SVC.

#### 4.1 Spatial analysis – determination of geoelectric strike

The *spatial analysis* of the magnetotelluric Earth response endeavours to extract information about the configuration of the induced natural EM fields, which in turn depend on the geometry, size and configuration of lateral geoelectric inhomogeneities. Herein, the spatial analysis of impedance tensors implements the Anti-symmetric Singular Value Decomposition (ASVD) proposed by Tzani (2014), which is based on the topology of the SU(2) rotation group and results in a characteristic state – characteristic value analysis of the impedance tensor: at any location on the surface of the Earth, the magnetotelluric induction problem can be formulated as

$$\begin{bmatrix} E_1(\theta_E, \Phi_E, \omega) \\ E_2(\theta_E, \Phi_E + \frac{\pi}{2}, \omega) \end{bmatrix} = \begin{bmatrix} 0 & \zeta_1(\omega) \\ -\zeta_2(\omega) & 0 \end{bmatrix} \cdot \begin{bmatrix} H_1(\theta_H, \Phi_H, \omega) \\ H_2(\theta_H, \Phi_H + \frac{\pi}{2}, \omega) \end{bmatrix},$$

where  $\theta$  and  $\Phi$  are rotation angles,  $\{E_1(\theta_E, \Phi_E), H_1(\theta_H, \Phi_H)\}$  comprises the *maximum characteristic state* of the magnetotelluric field,  $\{E_2(\theta_E, \Phi_E + \pi/2), H_2(\theta_H, \Phi_H + \pi/2)\}$  comprises the *minimum state*,  $E_1$  and  $E_2$  are the eigenvalues of the telluric field and  $H_1, H_2$  the eigenvalues of the total magnetic field. With reference to the experimental coordinate axes  $\{x, y, z\}$ , the angles  $(\theta_E, \Phi_E)$  define a *characteristic* coordinate frame  $\{x_E, y_E, z_E\}$  of the electric field such that  $x_E$  is rotated  $\Phi_E$  clockwise with respect to the  $x$ -axis and the plane  $\{x_E, y_E\}$  is tilted by an angle  $\theta_E$  clockwise with respect to the horizontal  $\{x, y\}$ . Likewise, the angles  $(\theta_H, \Phi_H)$  define the characteristic frame  $\{x_H, y_H, z_H\}$  of the magnetic field such that  $x_H$  is rotated by  $\Phi_H$  clockwise with respect to the  $x$ -axis and the plane  $\{x_H, y_H\}$  is tilted by  $\theta_H$  clockwise with respect to  $\{x, y\}$ . Each characteristic frame contains orthogonal, *linearly polarized* components. In the case of 2-D geoelectric structures,  $\Phi_E = \Phi_H$  and  $\theta_E = \theta_H = 0$ . In 3-D structures it is possible that  $\Phi_E \neq \Phi_H$  and/or  $\theta_E \neq \theta_H \neq 0$ ; the electric and magnetic eigen-fields may not be orthogonal. In 3-D structures the electric and magnetic characteristic frames are not horizontal because the magnetotelluric field is three-dimensional and may be associated with significant gradients. Accordingly, the tilt angles  $\theta_E$  and  $\theta_H$  are measures of the local landscape of the telluric and magnetic field. The projection of the eigenstates on the horizontal plane comprises elliptically polarized components; the normalized projected field vectors will have a major axis equal to  $\cos\theta$  and a minor axis equal to  $\sin\theta$  so that  $b = \tan\theta$  is the *ellipticity* with  $\theta > 0$  implying a counter-clockwise sense of rotation while  $\theta < 0$  a clockwise sense: Ellipticity on the horizontal plane is defined in terms of a rotation in higher dimensional space. It is not straightforward to see in this thrifty presentation, but the essence of this analysis is that it approaches the geoelectric structure as the equivalent of a birefringent material at low frequencies and large scales.

A *typical* example of an impedance tensor processed with the ASVD is provided in Section S6 of the Supplement. Analogous studies of all impedance tensors indicate that the geoelectric structure is overall very conductive and principally 2-D, exhibiting site-specific geoelectric structural trends at periods generally shorter than 0.5s, but rather coherent and spatially extended structural trends at periods longer than 1s. The latter is illustrated by mapping the polarization ellipse of the maximum electric field, which

is shown in Fig. 8 in the form of averages over the interval 1s – 100s (1Hz – 0.01Hz) that contains responses from deeper and larger-scale structural elements (of the order of 2–4 km as will be shown below). Focusing on the configuration of the maximum electric field over the entire study area, we note that the “deeper” structure is generally associated with low to moderate ellipticities, indicating that it is essentially two-dimensional. The azimuth of the maximum electric field in Akrotiri Peninsula is  $343^{\circ}\pm 16.5^{\circ}$ , while in the Oia – Cape Columbo and Vourvoulos areas it is  $244^{\circ}\pm 6.5^{\circ}$ . The directions of the maximum electric fields are almost orthogonal across the Trans-Santorin Divide (also see Sections 3.2, 5.3-4 and Papageorgiou et al., 2010), which indicates that the TSD comprises a major geoelectric interface. This conclusion is corroborated by the “holistic” approach to the determination of large-scale geoelectric structural trends proposed by Banks and Wright (1998), which is based on the *simultaneous* analysis of all impedance tensor observations. The relevant analysis is presented in Section S7 of the Supplement and yields a “regional” geoelectric strike of approx.  $N335^{\circ}\pm 12.26^{\circ}$  which is very comparable to the strike determined by analysis of individual impedance tensors, as well as to the strike of the TSD.

The Magnetic Transfer Function (MTF) is the second pillar of the spatial analysis of natural field electromagnetic data. Herein, the MTF is used in its Induction Vector (IV) representation, the definition of which is given in Section S4 of the Supplement. A *typical* example of IV is given in Section S6 of the Supplement. For simplicity and brevity, and with hindsight that the structure is predominantly 2-D, we shall only use the Real IV drawn in the Parkinson convention in which it *points toward* current concentrations (conductivity interfaces, e.g. Rokityansky, 1982). Fig. 8 illustrates the configuration of the Real IVs throughout the SVC, in the form of averages over the interval 1s – 100s (response of the deeper/larger-scale structural elements). An immediate first observation is that the mean azimuth of the in SW Thera and to the *west* of the TSD is  $N56^{\circ}\pm 10^{\circ}$ . This is almost orthogonal to the general orientation of the maximum electric field. In addition, individual vectors are generally transverse to the local maximum electric fields and point toward the TSD. On the other hand, the mean azimuth of the Real IV *east* of the TSD is  $N206^{\circ}\pm 11^{\circ}$ . This is comparable to the longitudinal direction of the maximum electric field and individual vectors point toward the TSD. The spatial properties of the Real IV indicate that the TSD comprises an elongate conductive interface with dike-like characteristics.

The regional geoelectric strike, the configuration of the maximum electric field and the configuration of the Real Induction Vectors, all point toward the existence of a  $N330^{\circ}$ - $N340^{\circ}$  elongate conductor along the TSD, which electrically separates the SVC in a south-western half in which induction is compatible with the TE mode over the conductive side of a quasi-2D interface, and a north-eastern half where induction appears compatible with the TM mode over the resistive side of a quasi-2D interface. The existence of such a structure is altogether possible because the TSD is located on a NNW-SSE notch of the surface of the Alpine basement (Fig. 8); this, in turn, is quite suggestive of a sub-vertical active fault associated with intense circulation of hydrothermal fluids. At North Thera, the maximum electric field is not linearly polarized and the polarization ellipses and real induction vectors are not exactly parallel as typically expected of true 2-D geoelectric configurations. We interpret this effect in terms of fluid circulation and diffusion associated with the Columbo Fault Zone that generates a distributed low conductivity zone exhibiting a weakly 3-D or, equivalently, quasi-2D electric structure in which the *primary* activity takes place in the NW-SE direction associated with the TSD.

In concluding this section we also note that the absence of significant conductivity in some faults related to the Anhydros Basin, as for instance at central Thera, is a good indicator of low-level circulation in these faults. Interestingly enough, part of the Kammeni Line activated during the 2011-2012 crisis and the process presumably involved fluid injection from below (Papadimitriou et al., 2015; Vallianatos et al.,

2013). If so, this fluid was *not* present prior to the crisis according to the magnetotelluric data, which goes on to show that the activation of the Kammeni Line was very likely a short-term dynamic effect.

## 4.2 Quantitative interpretation

The dearth of longer period data combined with the rather awkward distribution of usable magnetotelluric stations prevents the quantitative determination of large-scale geoelectric structures. The only area in which measurements are available in numbers and spacing sufficient to warrant two-dimensional inversion is the Akrotiri peninsula. This was carried out along a 4.3km profile of approx. W-E orientation between site 091 (approx. 1.5km east of Faros) and site 121 at the foot of the peninsula (Fig. 7). Joint TE/TM mode inversion was conducted with the algorithm of Rodi and Mackie (2001), assuming that the maximum impedance (maximum electric field) in that area corresponds to TE mode induction. In all cases a discretized homogenous half-space was used as starting model; the discretization scheme is apparent in Fig. 9. Topography was also taken into consideration although we only illustrate results for elevations below sea level. Several inversions with different regularization factors were carried out before a final model was declared. The quality of the solution is marginal in terms of objective metrics: while  $E\{\chi^2\} = 348$ , the observed value of the metric was almost twice as high ( $\chi^2 \cong 664$ ). Nevertheless, the fractional error is only 6.77% and the goodness of fit  $R^2 = 0.93$ . As additionally argued in Section S8 of the Supplement, the data is rather adequately fitted in terms of “expert judgement”. Accordingly, the solution is deemed fit for interpretation.

The resistivity model is presented in Fig. 9. It is apparent that the structure is very conductive ( $< 3\Omega\text{m}$ ) from just below sea level to approximately 0.5km. In the eastern half of the section the thickness of the conductive layer compares well with the thickness of the pyroclastic overburden. It follows that the shallow conductor can be identified with the pyroclastic layer which is rather porous and susceptible to pervasive sea-water infiltration. A second significant observation is that at depths greater than 0.5 km, the areas between sites 091 – 103 at the west side of the profile and 133 – 121 at the east side, both appear to be associated with sub-vertical conductive zones of less than  $6\Omega\text{m}$ . The eastern of those is located at the foot of Akrotiri peninsula and possibly marks the east margin of the TSD; it is consistent with TSD being a sub-vertical fault in which low resistivities develop as an epiphenomenon of high hydraulic permeability. The western sub-vertical conductor may have a similar interpretation but further inference is difficult due to lack of corroborating evidence.

In a final note, at depths below 3km the structure is not resolvable and the solution reduces to a weakly inhomogeneous half-space, presumably because the very high near-surface conductivity severely attenuates the magnetotelluric field and reduces penetration. It appears that such limitations extend over the entire island of Thera, as can easily be verified by one-dimensional inversions in the Oia – Cape Columbo and Vourvoulos areas; detailed results are not presented herein for the sake of brevity but a typical example is provided in Section S9 of the Supplement. It is clear that the magnetotelluric data cannot penetrate to the depths of major volcanic elements, such as the magma chamber which is located at depths greater than 5km (Lagios et al., 2013; Newman et al., 2012). Accordingly, all qualitative and quantitative results refer to interfaces buried at depths between 0.5 and 3 kilometres, the sub-vertical two-dimensional geometry of which is compatible that of tectonic faults functioning as fluid circulation zones.

## 5. DGPS Observations

A GPS network comprising 18 (and as of 2011 twenty) re-occupiable stations has been established in the SVC (Fig. 7) and was intermittently measured in numerous campaigns since 1994. To ensure stability,

stations have generally been established on firm (non-pyroclastic) rock formations and their layout was designed so as to maximize performance. Dual-frequency geodetic receivers mounted on surveying tripods were used for measurements (WILD type SR299, SR399 and AX1200Pro, Trimble, Ashtech). The data was processed with the Bernese v4.2 software (Beutler et al., 2001) for the campaigns up to 2005, and v5.0 (Dach et al., 2007) for the campaigns since 2011. GPS satellite ephemerides and satellite and station clock data produced by the International GNSS Service were used to calculate daily coordinates and tropospheric parameters. Station 7 was selected for local reference on the basis of geological criteria, as it is located on the Alpine basement (Upper Triassic limestone). Station 7 is tied to the ITRF2008 frame of reference using data from a number of IGS Reference Frame Stations in Europe (<http://www.epncb.oma.be>), and was operated continuously during all campaigns. The data acquisition procedure is standardized and the same for all campaigns but the data of each campaign was processed separately. In each campaign, the satellite (“roving”) stations were occupied at least twice for at least 24 and up to 92 hours per occupation period, with all measurements conducted using a sampling rate of 15s. For each satellite station, positioning solutions from all occupational periods of the same campaign were combined in order to enhance the statistical rigour of the final (solved) coordinates. In this way, RMS errors of about 1.0–5.3 mm for the horizontal and 2.0–8.1 mm for the vertical component of the displacement could be typically achieved at the 90% confidence level. The results are presented in the form of a displacement field relative to Station 7.

### 5.1 Period 1994 - 2005

The DGPS was re-occupied eight times between 1994 and 2005; details can be found in the work of Lagios et al. (2013) and Papageorgiou et al. (2010, 2007). A remarkable outcome of these surveys is that the deformation rate was linear in almost all stations. This allowed the displacement rate (velocity) at each station to be computed directly from the slope of the best fitting linear trend, which is the form in which this data set has been presented in the previous work. Herein we use post-2005 data that includes non-linear effects due to the 2001-2012 unrest. Accordingly and for the sake of comparison we shall present the 1994-2005 data only in the form of a net displacement field.

The cumulative vertical displacements relative to Station 7 are listed in Table 2 and show subsidence at Nea Kammeni islet, (Stations 15, 22 and 45), as well as at the tip of Akrotiri peninsula (Station 2). Notably, in Nea Kammeni subsidence appears to increase toward the TSD, from  $-14.8 \pm 0.35$  mm at the northwest (Station 15) to  $-61.9 \pm 0.35$  mm at the southeast (Station 45). The rest of the network detects unevenly distributed uplift which is less than 9mm at Therassia (Stations 56, 57) and Akrotiri peninsula (Station 6), and maximizes along the NW coast of Thera ( $>36$  mm at Stations 27 and 33).

The cumulative horizontal displacements relative to Station 7 are also listed in Table 2 and illustrated in Fig. 10 (blue arrows); they are *significant* in the majority of the stations and indicate a complex kinematic pattern. The west side of the TSD exhibits significant motion to the NNW ( $N321^\circ$  on average), with more than 30mm of cumulative displacement observed at Akrotiri peninsula (Stations 2 and 4) and more than 20mm at Therassia (Stations 56 and 57). The east side of the TSD exhibits net westward horizontal displacement. This is significant at the north (Oia – Columbo areas) where an average of 21mm in the  $N289^\circ$  direction is observed at Stations 26, 29 and 33. Stations located near the eastern rim of the caldera (12, 18 and 43) on average exhibit relatively small ( $<11$  mm) westward ( $\sim N269^\circ$ ) displacement. The differences observed between the former and latter groups of stations indicate differential motion across dislocation surfaces with significant heave, which we presume comprise the Columbo Fault Zone (CFZ). Finally, Station 27 (Monolithos) is apparently *sui generis* exhibiting 15.8mm of SE-ward ( $N124^\circ$ )

displacement, almost *antiparallel* to the sense of motion observed west of the TSD. At Nea Kammeni the horizontal displacement changes from the NW to the SE, from 14mm at N262° and N244° at Stations 15 and 22 respectively, to 21mm at N212° at Station 45. In combination with the vertical displacement data this shows that Nea Kammeni actively tilts to the SW as one moves toward the TSD. This behaviour may imply that the TSD forms a sharp boundary immediately to the west of Nea Kammeni – or between Nea and Palea Kammeni as the terrain appears to indicate.

## 5.2 Periods 1994 – 2012 and 1994 – 2017

The period between 2011 and 2012 is marked by a volcano-tectonic crisis, for which details can be found in Papadimitriou et al. (2015), Lagios et al. (2013), Parks et al. (2013), Newman et al. (2012) and others. A magma volume of 7–12 Mm<sup>3</sup> was injected at depths of 4–6 km beneath the North Basin, with its epicentre located at (25.389°E, 36.426°N), approximately 2km N-NW of Nea Kammeni (Lagios et al., 2013). Between September 2011 and June 2012, the injection caused dilation of the crust and non-linear, radial centrifugal deformation of the order of 30–65mm in both the horizontal and vertical directions (Fig. 11, magenta arrows). At the south of the SVC the horizontal displacement was easterly and significantly smaller (12–29 mm). When referred to ITRF2008, the deformation assumed a radially symmetric centrifugal pattern. The strain field exhibited an almost isotropic extensional pattern centred on the North Basin (for details see Lagios et al., 2013). This had a profound effect on the cumulative displacement since 1994, as listed in Table 2 and illustrated in Fig. 10 (green arrows). East of the TSD, it resulted in counter-clockwise rotation of displacement vectors by 20°-30°, including Nea Kammeni, with the notable exception of Station 45. Conversely, significant clockwise rotation was observed west of the TSD, ranging from approx. 30°-50° in the Oia–Columbo area, to more than 90° in stations located near the caldera rim (where very small displacement was observed prior to the crisis).

The dilation decelerated and ceased after June 2012 and has actually reversed as of December 2012. As evident in Table 3 and Fig. 11 (black arrows), between years 2013 and 2017 the crust appears to be *deflating*: at the north of the SVC, displacement occurs in a radial centripetal mode (Stations 56, 57, 26, 29, 43, SANT). However, at Nea Kammeni (Stations 5, 22 and 45) the motion is the same as during 1994–2005 and at central Thera (Stations 18, 27, 55) it is south-easterly; this may indicate residual local activity which we attribute to the Kammeni–Fira line (see below). At any rate, deflation dominates crustal deformation and continues to mask tectonic effects. In comparison to the period 1994–2012, the deflation has caused small clockwise rotation of displacements west of the TSD and overall counter-clockwise rotation east of the TSD (Fig. 11, red arrows): the cumulative displacement observed during 1994–2017 appears to be slowly returning to the pre-crisis state.

## 5.3 Tectonic Implications

As previously indicated by Papageorgiou et al. (2010) and Lagios et al. (2013), the overall kinematic patterns observed in the period 1994–2005 can best be explained in terms of tectonics rather than pre-eruptive or other volcanic activity. This was consistent with the then reposed state of the SVC: no volcanic activity was reported before, during and immediately after the measurements. In addition, deformation due to intrusive activity is generally expected to exhibit distinctive symmetric centrifugal/outward or centripetal/inward patterns, as actually observed during and after the 2011-2012 unrest. Furthermore, intrusive processes during 1994–2005 can be ruled out by the absence of any companion activity (e.g. seismicity, elevated gas emissions, increased hydrothermal flux etc.).

Overall, it would appear that in terms of structure, the SVC comprises two major blocks separated by the

Trans-Santorin Divide: the western in which the vertical displacement is small or negative and the horizontal displacement significant in the N320°-N330° direction, and the eastern in which vertical displacement is significant throughout, but horizontal displacement only in the vicinity of the Columbo Fault Zone (N290° direction), but rather small elsewhere (in the E-W direction). At any rate, the uneven pattern of the vertical and horizontal deformation clearly indicates that the mechanisms producing it are complex and involve more than single fault activity. The observed displacement field allows for the determination of the strain tensor in the vicinity of the DGPS stations. This exercise was conducted with the “grid-strain” method and software of Pesci and Teza (2007) and the results are presented in Fig. 12.

In the area of Cape Columbo the principal mode of deformation is NW-SE extension, in consistence with the tectonic and volcano-tectonic activity recently observed around the Columbo submarine volcano (Dimitriadis et al., 2009). However, as one moves toward and crosses the TSD, the direction of extension rotates clockwise and a NE-SW horizontal compressive component develops, progressively growing in amplitude and matching or exceeding the amplitude of extension at Therassia (Stations 56 and 57). Taken together with the displacement field and strain configuration, this appears to signify a transition from NE-SW oblique-slip extensional fault kinematics in the Columbo Fault Zone, to NNW-SSE right-lateral fault kinematics in the TSD. It is also important to emphasize that if there is heave associated with CFZ at all, it can *only* be *left-lateral*; this is contrary to several published accounts (e.g. Druitt et al., 1999; Dimitriadis et al., 2009; Papadimitriou et al., 2015) and will be elaborated in Sections 5.4 and 6.

In central-west Thera (Fira – Imerovigli) and along the rim of the caldera, the direction of extension is practically W-E. The transition from NW-SE to W-E extension is swift and takes place just south of the CFZ. In the south of Thera, the direction of extension is also W-E in the vicinity of the N-S west-dipping normal fault of Mt. Gavrilos, both along its exposed and buried segments. As also mentioned in Section 3, Mt. Gavrilos fault can be projected northwards along the rim of the caldera and up to Imerovigli. Accordingly, it is compelling to note that the direct observation of W-E extension across the mapped and inferred segments of Mt. Gavrilos fault should be more than coincidence.

As one proceeds westwards from Mt. Gavrilos to Faros, the direction of extension becomes WNW-ESE, while very significant N-S to NNE-SSW compression develops and intensifies across the TSD, maximizing at Faros on the west side of the TSD. Together with the displacement field, this implies NNW-SSE right-lateral kinematics for the TSD. It also implies that if NE-SW faults have, then it can only be left-lateral (e.g. Anhydros FZ). Finally, the NNE-SSW compression is almost exactly normal to the E-W faults mapped at the south of the Prof. Elias block, as well as to the southern rim of the caldera. This again indicates that the southern flank of the caldera may have formed along *auxiliary* inverse (compressive) faulting structures.

## 5.4 Modelling

The plausibility of the tectonic model derived in Section 5.3 is tested by simulating the ground deformation observed during 1994-2005 and, specifically, if it can be explained with some configuration of NW-SE dextral strike-slip faults coincident with the Trans-Santorin Divide and NE-SW sinistral-normal faults coincident with the Columbo FZ. The displacement field generated by such fault configurations was quantified with the “GTdef” inversion algorithm (Chen et al., 2009; Feng et al., 2012), which implements Okada’s (1985) formulation of fault-dislocation. Although this approach has been developed for earthquakes, it is warranted to use because if material properties are assumed to be linear, the only difference between earthquakes and aseismic creep is the rate of moment release: in Okada’s (1985) formulation this is not an issue.

The basic fault model is shown in Fig. 13 - 16 and comprises:

- (i) One oblique-slip fault labelled AB in Fig. 13 representing the TSD and having  $\varphi=N331^\circ$  and  $\delta=85^\circ$  with tolerances of  $\pm 5^\circ$  in  $\varphi$  and  $\pm 10^\circ$  in  $\delta$  and a total length of 16km (from Vlychada, through the Nea and Palaea Kammeni channel to exactly east of Therassia). The net slip along the fault plane was constrained by the maximum displacements observed along the TSD during 1994-2005. The strike-slip component was allowed to vary between 10mm left-lateral and 30mm right lateral and the dip-slip component allowed to vary between 0mm and 20mm down-dip (normal fault).
- (ii) A zone comprising two parallel oblique-slip faults labelled CD and EF in Fig. 13, respectively representing the Cape Columbo (CCF) and Mikros Prof. Elias (MPEF) faults; they both have  $\varphi=N47^\circ$ ,  $\delta=80^\circ$ , tolerances of  $\pm 3^\circ$  in  $\varphi$  and  $\pm 5^\circ$  in  $\delta$  and total lengths of 9km. The net slip was also constrained by the maximum displacements observed in the vicinity of the CFZ, but the strike-slip component was allowed to vary between 30mm left-lateral and 30mm right-lateral, while the dip-slip component from 30mm up-dip (thrust) to 30mm down-dip (normal).

In all cases, a tensile tolerance of  $\pm 1$ mm was allowed but did not affect the results, and the faults were assigned a width of 6km. This is the approximate depth of the magma chamber activated during the 2011-2012 crisis (Lagios et al., 2013), as well as the approximate floor of earthquake activity at the SVC (e.g. Papadimitriou et al., 2015); thus, it is taken to comprise the local limit of the schizosphere presumably because the thermal regime does not allow for rate-and-state friction processes to extend below.

The distribution of slip on (real) fault planes is expected to be non-uniform, therefore all model faults were discretized into arrays of rectangular tiles and each tile was allowed to slip on its own. In order to obtain physically meaningful results the tiles cannot be allowed to slide independently; instead, adjacent tiles are required to slip coherently so as to ensure smooth variation of slip across the fault plane. This can be done by introducing a regularization (smoothing) factor  $k$ , which determines the degree of dependence between adjacent tiles and controls the roughness of the fault model. The higher the regularization factor, the more uniform is the distribution of slip on the fault plane and, usually, the worse the misfit between observed and calculated displacements. Because a solution with realistic slip distribution must be associated with sufficiently low misfit, we were faced with a severely non-unique problem. Given the distribution of the DGPS stations and their average spacing of 2-3 km, we attempted to determine a good-as-possible discretization scheme via checkerboard resolution tests. After numerous trials with different tiling schemes, variants of the basic fault model configuration and regularization factors, we found a best fitting scheme in which fault AB ( $\varphi \approx N331^\circ$ ,  $\delta \approx 85^\circ$ ) was discretized into an array of  $2 \times 2$  km tiles and faults CD and EF ( $\varphi \approx N47^\circ$ ,  $\delta \approx 80^\circ$ ) discretized into arrays of  $2.25 \times 2$  km tiles; the three faults were located as per Fig. 13 and  $k=1000$ . The errors associated with observed displacement vectors were taken into consideration. In this configuration, alternating values of zero (black) and one (white) metres of slip were assigned to each tile (Fig. 14a) and the expected displacement at each GPS station was calculated. The DGPS network was able to adequately recover the distribution of slip in almost all tiles and depths up to 4km (Fig. 14b). The resolution decreased at greater depths in faults AB but *not* in CD and EF, which is very significant as will be seen below.

Using the above model/discretization scheme we obtained multiple solutions with a broad range of regularization factors and adopted the one yielding an acceptable RMS misfit (8mm) at the inflection of the curve tracing the trade-off between model roughness and misfit: it turned out that this was again  $k=1000$ . Fig. 13a illustrates the observed (black) and calculated (red) horizontal displacement vectors and Fig. 13b the corresponding vertical displacement vectors. It is apparent that the fit is excellent for the

horizontal component and fair for the vertical, especially at north Thera. In the horizontal displacement field on which our attention is mainly focused, there is only one notable discrepancy at Station 12 (Imerovigli), attributable to local effects related to the geotechnical characteristics of the ground on which the station was founded; we consider this to be the only alternative since the simulation of the displacement vectors at the immediately adjacent Stations 18 and 43 is excellent.

Fig. 15 illustrates the distribution of slip on the three fault planes as seen from Fira. In fault AB, slip is evidently patchy. Between 10 and 16km along strike, the sense of slip is dominantly right-lateral and concentrated on the lower half of the fault plane (2-6 km). Between 6 and 10km along strike, dislocation is mainly dip-slip and limited to the top 2 km of the fault plane. The lower half of the fault plane appears to not slide at all. This is the area where the fault straddles the Kammeni Shield and the shallow source of the observed vertical displacement indicates that subsidence should rather be attributed to the volcanic nature of the Shield and, possibly, its interaction with the Kammeni line. Finally, between 0 and 6km along strike the dominant mode of dislocation is right-lateral and concentrated between 2 and 4km down-dip. In faults CD and EF the net slip is significant (up to 50mm) and normal left-lateral (oblique-slip). At the south-west end of the fault plane, dislocation is uniformly thrust left-lateral possibly due to interaction with fault AB. However, as one moves away from point C, the sense of motion changes (rotates) so that between 2.25 and 9km along strike, the lower two-thirds of the hanging wall slip in a normal left-lateral sense. The upper third of the fault plane exhibits small uplift associated with very small left-lateral heave. In EF, the sense of slip is very peculiar. In the lower third and of the fault plane slip is *exactly* as per fault CD; counting from left to right and from top to bottom, the central part of the plane exhibits a very peculiar “shear” to be explained below, between tiles (2,2) which slides in a dextral oblique-normal sense and (3,2) which slides in a sinistral oblique-inverse sense; the first half of the top third of the fault plane (0-4.5km) does not slide at all and the second half repeats the shear pattern of the central part in reverse. Given that resolution is excellent (Fig. 14b), such complex and peculiar behaviour can be attributed to combination of coarse discretization combined with local interplay between tectonic and volcanic processes, as will be elaborated below.

The coarse discretization scheme yields valuable information but also begets a lot of questions as to the origin of complexity in the dislocation patterns. To redress, we have also performed inversions with a finer discretization scheme in which all planes were tiled into  $1 \times 1$  km arrays. This fails the checkerboard test but as will clearly be seen, interpretation is possible *and* valid by comparison to the model of Fig. 15. Fig. 16 illustrates the distribution of slip on the finer discretized fault planes as obtained with a regularization factor  $k=1000$ ; the quality of the solution can be studied in Section S10 of the Supplement. In fault AB the distribution of slip is essentially identical with its coarser discretized counterpart (Fig. 15). Nevertheless, the finer discretization allows one to observe that between 11km and 14km along strike, a concave patch of slight left-lateral dislocation in the upper half of fault plane may signify the interaction between AB and CD/EF. Moreover, between 0 and 6km along strike, slip appears to be considerably more smoothly and evenly distributed on the fault plane. In the finer discretized version of fault CD (Fig. 16), the distribution of slip is practically the same as in its coarser discretized counterpart (Fig. 15), but a “focal point” with a rather peculiar dislocation around it, appears at tile (5,2). The finer discretized version of fault EF yields some interesting features. The sense of slip in the lower half fault plane is almost uniformly normal left-lateral, in the upper half it is rather diverse: between 3-6km along strike and 1-4km down-dip, dislocation exhibits another “focal point” with a clear pattern of *divergence* around tile (5,3), while the top row of tiles (0-1km depth) exhibits *uplift* of mainly *inverse-dextral* sense. The divergence of slip with respect to tile EF(5,3) suggests that *outward* pressure is exerted from that region.

If true, this can hardly be of tectonic nature and we suggest that it is caused by injection of thermal fluids venting upwards from a deeper source. Furthermore, if thermal fluids are injected via a sub-vertical NW-SE plane connecting the focal point EF(5,3) and CD(5,2), and then spread laterally at depths of the order of 2–3 km, their effect might also explain the split nature of dislocation between the upper and lower halves of CD and EF. Accordingly, we conclude that the shallow (<3km) deformation effected by these faults (Columbo FZ), is strongly influenced by fluid injection, while at greater depths deformation is most likely controlled by tectonic activity and exhibits almost uniform normal-sinistral dislocation. This may explain the scarce superficial evidence of right-lateral faulting previously reported by a number of authors (e.g. Druitt et al., 1999; Dimitriadis et al., 2009; Sakellariou et al., 2010). Perhaps not surprisingly, the line(s) joining tiles EF(5,3) and CD(5,2) are NNW-SSE oriented, almost coincident with the coastline and apparently located within the (inferred) pipe of the Peristeria volcano (Fig. 5b/ Section 3.2). It is thus plausible that the Peristeria lavas erupted through a NNW-SSE fissure bracketed by the CFZ and associated with the TSD family of faults.

The tectonic model considered in this Section is simple and incomplete, but amply demonstrates that the surface displacement field observed during 1994-2005 can be explained by tectonic activity expressed through dominantly right-lateral NNW-SSE faults and normal left-lateral NE-SW faults, plus a component of volcanic origin expressed by fluid injection at the north of the SVC.

## 6. Discussion and Conclusions

The localization, development and evolution of arc volcanism are generally modulated by regional tectonics, with particular reference to rapidly deforming realms such as the South Aegean Sea. The Santorini Volcanic Complex (SVC) is a central and characteristic feature of the Hellenic Volcanic Arc. Understanding the dynamics that shape its evolution should be important for understanding its localization and significance in the geodynamic setting of the south Aegean region, let alone that it may be valuable in the analysis of regional earthquake and volcanic hazards.

Tectonic activity in the SVC is very difficult to assess with standard techniques such as geological mapping, remote sensing/ photogrammetry, terrain analysis and seismological/seismotectonic analysis. The SVC's complicated and catastrophic volcanic history has produced a cluster of small and awkwardly shaped islands, covered by soft and easily erodible pyroclastic deposits from which all tell-tale tectonic features are quickly removed. In addition, earthquakes are generally absent except for periods of crisis, and then confined to small areas. Herein we attempt to bypass these difficulties by geophysical exploration and satellite positioning methods. Specifically, we use 3-D gravity modelling to strip the effect of igneous rock formations and expose the footprint of tectonic activity on the hard (pre-volcanic) Alpine basement, as well as natural field electromagnetic methods to detect elongate *epiphenomenal* electrical conductivity anomalies associated with convective circulation of thermal fluids in fault planes. Time-lapse differential GPS is used to extract direct evidence about the kinematics and dynamics of contemporary crustal deformation. The findings of each of these methods are detailed in Sections 3-5. Herein we focus on the discussion and correlation of *jointly* identified features as highlighted in Fig. 17.

The **Trans-Santorin Divide (TSD)** develops lengthwise of the (straight) line joining the areas of Vlychada/Cape Exomytis, the Kammeni islets and the Oia – Therassia strait. In the topography of the Alpine basement the TSD appears as a series of dents and depressions aligned in an approximately N330° direction. At depths greater than 500m, the TSD is collocated with a major vertical conductive zone which is apparently associated with fluid circulation. The contemporary surface deformation pattern identifies the TSD as a vertical, segmented, right-lateral dislocation surface. All three lines of evidence

point to TSD being a significant aseismic dextral strike-slip fault that splits the SVC into NE and SW halves. In the area of the Oia strait (Oia – Therassia channel), the TSD is very conveniently located so as to account for the localization of the landslides that caused the breach and guided the inflow of sea water right after the formation of the Minoan caldera (Nomikou et al., 2016). Faulting features with kinematic characteristics analogous to TSD may also exist in eastern Thera, as attested to by the displacement observed at GPS station 27 and the configuration of the magnetotelluric field at MT station 171. If so, these would be buried between the Prof. Elias and Monolithos blocks and also develop along the caldera wall between Mts. Mikros Prof. Elias and Megalo Vouno. Modelling of the gravity data indicates that such faults may be associated with the extrusion of Peristeria Volcano lavas while modelling of DGPS data indicates that together with the CFZ, they may facilitate injection of fluids into the first few kilometres of the crust.

The **Columbo Fault Zone** develops in a NE-SW direction between Mts. Mikros Prof. Elias and Megalo Vouno at the north-eastern half of the SVC (north Thera) and terminates against the TSD. It comprises a pair of parallel sub-vertical – south-westerly dipping normal-sinistral faults: the Cape Columbo Fault to the north and the Mikros Prof. Elias fault to the south. The CFZ may be associated with thermal fluid injection into the shallow crust, possibly occurring at depths of 2-3 km via a TSD-like fissure located approximately beneath the coastline (caldera wall) and within the pipe of the Peristeria Volcano. Onshore, the CFZ does not appear to have a clear signature in the gravity field. Offshore, however, it appears to have formed a significant NE-SW depression in the Alpine basement, which develops beneath the North Basin and apparently terminates on the TSD. In addition, the CFZ appears to have limited effect on the electrical conductivity of the SVC crust, at least in comparison to the TSD.

The **Anhydros Fault Zone**: This is a very significant NE-SW system that forms the NW flank of the Santorini – Amorgos Ridge; it has been identified by previous research off the northeast coast of Thera Island and is thought to traverse the SVC. In Thera Island, the onshore presence of the AFZ is confirmed only by its footprint on the Alpine basement, where it is seen to comprise a set of parallel, north-westerly dipping faults located between the Athinios–Monolithos line and Fira. In addition, the morphological characteristics of the Alpine basement in the area of the Akrotiri Volcano indicate that the AFZ may have had a role in the extrusion of the Akrotiri lavas. Given the distribution of magnetotelluric measurements, the AFZ does not appear to have some effect on the electrical conductivity structure, meaning that it is probably *not* associated with active circulation. It also appears to insignificantly contribute to the observed horizontal displacement field, which can be entirely explained by the TSD and CFZ faults (Section 5.4). The latter two observations indicate that the AFZ may not be active at present or in the recent geological past.

The CFZ and AFZ have antithetic throws and thus generate a graben-like structure that contains the volcanic centre of the Kammeni islets. Notably, the focal mechanism of the 1956 Amorgos earthquake as re-evaluated by Okal et al., (2009), indicates nearly normal faulting with either a small component of right-lateral slip on a fault dipping gently to the SSE ( $\varphi=39^\circ$ ;  $\delta=25^\circ$ ;  $\lambda=246^\circ$ ), or left-lateral slip on a fault plane dipping more steeply to the NNW ( $\varphi=245^\circ$ ;  $\delta=67^\circ$ ;  $\lambda=281^\circ$ ). The latter is compatible with the geometrical characteristics of the AFZ observed herein, as well as by previous research (e.g. Sakellariou et al., 2010). It is also consistent with the AFZ being normal-sinistral: in Sections 5.3 and 5.4 we concluded that given the observed kinematics of the TSD and CFZ, if NE-SW faults in the vicinity of the SVC have any heave, it can only be left-lateral.

The strain field computed for the period 1995-2005 indicates E-W extension lengthwise of a zone stretching from Cape Exomytis to Athinios port and along the east flank of the caldera, up to Imerovigli (Section 5.3/ Fig. 12). This calls for N-S normal faulting. The only significant N-S faulting feature hitherto charted on the SVC is a short west-dipping segment mapped along the eastern flank of Mt. Gavrilos. The gravity data not only confirms that it is normal, but also that it extends as far north as Athinios Port and that it can be projected along the caldera wall up to Imerovigli. At south Thera and along the Akrotiri peninsula, significant NNE-SSW compression is inferred and expected to associate with E-W to WNW-ESE *auxiliary* tectonic features. Given the stress/strain characteristics of that area, compression does not prevail, but also does not entirely go away. Accordingly, it may not generate typical (slip-accommodating) inverse faults, but may generate localized process zones that weaken the crustal material and facilitate collapse during catastrophic events such as caldera formation. In the area of Akrotiri peninsula there is no distinguishable electrical signature, hence no active fluid circulation associated with the purported E-W faults which would appear to comprise passive secondary features.

As can be seen in both Fig. 15 and 16, the distribution of slip is rather patchy in the models of TSD and CFZ: some patches exhibit very high and some very low slip rates. This is *normal*, if not *expected* behaviour of active faults. The patchy slip distribution at depth is translated to smaller but still significant displacement rates at the surface of the Earth which, anyhow, constitute objective observables consistent with the geodynamic setting of the South Aegean, as well as with very recent DGPS observations in the broader area of the SVC (Doxa et al., 2019); let us not overlook that the South Aegean, is one of the world's fastest spreading regions. The high slip rates at depth are also consistent with the absence of significant seismicity. Earthquakes are generated by stick-slip processes and for one to occur, the fault must first have stuck at depth. The SVC is an active volcano and the depth of the brittle-ductile transition is definitely shallower than 5-6km. In combination with intense thermal fluid circulation, the "stick" part of the "stick-slip" process is expected to be diminutive.

The arrangement of NNW-SSE right-lateral (TSD) and NE-SW normal left-lateral faults (CFZ) is summarized in Fig. 17 and provides rigorous constraints on the contemporary tectonics of the SVC and its vicinity. Together with the strain field (Section 5.3), it can be explained *only* if the NNW-SSE faulting direction comprises the synthetic (dextral) Riedel-R shear and the NE-SW direction the antithetic (sinistral) Riedel-R' shear. Inasmuch as this configuration of R and R' faulting directions can only be generated by an approximately N-S oriented  $\sigma_1$  and E-W oriented  $\sigma_3$  principal stress axes, the presence of *auxiliary* E-W compressional and N-S extensional failure is also expected and supported by direct (DGPS) and indirect (geophysical) evidence.

The N-S and E-W faulting directions are easier to observe in the hard rock formations of south Thera, but should also appear elsewhere in the SVC. The footprint of the caldera on the Alpine basement is a parallelogram with N-S long side and WNW-ESE short side. If the east flank of the caldera has formed by collapse along secondary westerly dipping N-S normal faults, it stands to reason that the west flank has formed by collapse along easterly dipping N-S normal faults located between capes Faros and Simantiri in NE Therassia, approximately as in Fig. 5 and 19 (CW1 and CW2). Similarly, collapse along the WNW-ESE short side of the parallelogram should have been guided by WNW-ESE "inverse faults" along the northern coast of Akrotiri peninsula, possibly between capes Skaros and Simantiri and along the south coast of north Thera (Oia area). Quite apparently, the caldera "parallelogram" is distorted in the area of the North Basin by the action of the CFZ. It is also plausible that the CFZ-AFZ graben may have had a role in forming the broad channel between Faros (Akrotiri peninsula) and Therassia, at the west side of the TSD.

The observed configuration of active faulting and principal strain/stress axes can only be driven by NW-SE right-lateral shearing of the broader SVC area, as also indicated by a line of “circumstantial” evidence. The latter includes the presence of charted NW-SE faults at southeast Thera, as well as prominent anisotropic morphological characteristics of the Alpine basement such as the NW-SE elongation of the Prof. Elias block and the almost perfect alignment of the Prof. Elias block, Kammeni islets and Therassia (Fig. 5). The shape of the caldera could be included in this evidence, in the sense that the “calderic parallelogram” may be understood as a “calderic rectangle” deformed by clockwise shearing. Finally, one may point to the anisotropic morphology of the whole (subaerial and submarine) Volcanic Complex (Fig. 1b). The exact geographical extent the NW-SE dextral shear, as well as its role and contribution to the regional tectonic and kinematic setting of the south Aegean Sea cannot be determined with the present data, or in the context of the present analysis.

Let us continue by briefly discussing and “reconciling” some significant aspects of “established ken”, with the results and conclusions presented herein. We begin by pointing out that hitherto, the CFZ was taken to comprise a dextral-normal fault zone based on evidence obtained at the surface (e.g. Druitt et al., 1999), or by shallow marine surveys (e.g. swath bathymetry as in Sakellariou et al., 2010). It was also thought that that the south boundary of the CFZ (Mikros Prof. Elias fault) was NW dipping and that together with the Cape Columbo fault, formed a local tectonic graben. Based on direct kinematic evidence, we have found that this cannot be true and the material caught between these faults cannot form a graben. It can, however, form a tilted block if the long-term vertical displacement on CCF is relatively larger than that on MPEF. At the same time, in Section 5.4 we have argued that fluid injection in the first few kilometres of the crust may generate *anomalous* near-surface dextral dislocation, consistently with the observations reported in previous studies which have apparently been based on incomplete evidence and were therefore *not* wrong. If true, this exemplifies the necessity of multi-parametric broadband evidence and the degree of caution required in dealing with complex tectono-volcanic deformation.

Another line of direct evidence in apparent contradiction with our results is the right-lateral dislocation computed for the majority of focal mechanisms of small earthquakes observed in the segment of the Kammeni Line activated during the 2001-2012 unrest (Papadimitriou et al., 2015). As above, we suggest that the contradiction is only apparent. The activated fault segment is almost exactly bounded by the major tectonic elements detected herein: The Mikros Prof. Elias fault to the north, the N-S caldera boundary (fault) to the east, the north boundary of the AFZ to the south and the TSD to the west. The activation occurred in response to dilation due to magma injection at depths of 4–6 km beneath coordinates (25.389°E, 36.426°N), approximately 2km north of Nea Kammeni in the North Basin (Lagios et al., 2013). Given this setting, it is straightforward to see that dilation pushed the footwall to the NE. We postulate that this effect, together with fluid injection and associated degradation of the mechanical strength of the activated fault segment, is adequate to explain the right-lateral dislocations as a *temporary* effect of volcanic, *not* tectonic activity. If true, this also exemplifies the level of caution needed in interpreting complex tectono-volcanic domains.

Our findings, especially those implied for the broader tectonic setting of the SVC, are not entirely consistent with “established ken” which posits that the NE-SW faults of the Anhydros basin are principally normal and exhibit small right-lateral heave (e.g. Tsampouraki-Kraounaki and Sakellariou, 2017; Sakellariou and Tsampouraki-Kraounaki, 2018; references therein). As repeatedly pointed out above, the international literature *does not* provide direct seismological or DGPS evidence about the kinematics of the faults related to the Basin; whatever information exists in favour of the “established ken”, is partial at best, (e.g. shallow marine surveys). On the other hand, in a very recent study of the S.

Aegean area based on 47 permanent GNSS stations, Doxa et al. (2019) have shown that the Cyclades region undergoes complex distributed block deformation and that the kinematics of the Anhydros basin are certainly normal and most likely associated with a small left-lateral heave, consistently with our model of the SVC. This line of evidence also suggests that the SVC belongs to a counter-clockwise rotating block that occupies the SW sector of the Cyclades and includes all major volcanic fields (SVC, Christiana and Milos). This is also consistent with our proposed tectonic model of the SVC. Accordingly, it appears that the tectonics and kinematics of the South Aegean region is quite more complex than hitherto acknowledged and the jury may still be out in regard to their specific nature.

In a final comment, our work provides clues to the “solution” of the so called "granite space problem in Santorini. This concerns the mechanism by which space is created for *viscous* magma to intrude and occupy large volumes of the crust (e.g. Hutton, 1996). In reality, the “space problem” is not exactly a problem because it is now understood, more or less, how magma can easily and quickly flow up vertical cracks and through small incremental intrusions, form large igneous bodies (e.g. Stevenson, 2009; Petford et al., 2000). It appears, thus, that the “solution” of the problem in Santorini is that magma ascends through the space created by active tectonics, and more effectively so in the vicinity of weak zones and space created by the interaction of active faults: all contemporary volcanic centres are associated with intersections of the *sub-vertical* R and R' faulting directions, with particular reference to the Kammeni islets at the junction of the TSD with the CFZ/AFZ graben and the epicentre of the 2011-2012 unrest which was located at the junction of the TSD with the CFZ. Given also the possible contribution of tectonics (faulting) in the formation of the caldera, it appears that SVC volcanism is controlled by tectonics and the Complex is physically shaped by tectonic rather than volcanic activity.

## 7. Acknowledgments

We sincerely appreciate insightful discussions with Dr Haralambos Kranis (National and Kapodistrian University of Athens). We are grateful to Prof. Dr Tim Druitt (University Clermont Auvergne) for valuable comments and recommendations. We are also grateful to Dr Dimitris Sakellariou of the Hellenic Centre for Marine Research for his constructive criticism that helped us improve this paper. Figures 8, 10-13 and 17 were created with version 5.4.2 of the GMT software package (Wessel et al., 2013).

## References

- Adams, N., 1987. The Thera Volcano (Santorini/Greece) - lithological, volcanological and geochemical development, PhD Thesis, Eberhard-Karls-Universität Tübingen, Germany, 241pp (in German); doi: 10.1594/PANGAEA.771548.
- Alexandri, M., Papanikolaou, D., Nomikou, P., and Ballas, D., 2003. Santorini volcanic field – New insights based on swath bathymetry. Abstracts IUGG 2003, Sapporo, Japan.
- Amante, C. and Eakins, B.W., 2009. ETOPO1 1 Arc-Minute Global Relief Model: Procedures, Data Sources and Analysis. NOAA Technical Memorandum NESDIS NGDC-24. National Geophysical Data Center, NOAA; doi: 10.7289/V5C8276M.
- Armijo, R., Lyon-Caen, H., Papanastassiou, D., 1992. East-West extension and Holocene normal-fault scarps in the Hellenic Arc. *Geology* 20, 491–494.
- Banks, R.J. and Wright, D., 1998. Telluric analysis of distributed magnetotelluric impedance measurements, *Annales Geophys., Suppl. 1 to v16*, C275; XXIII EGS Gen. Assembly, Nice, France, 20-24 April 1998.
- Basili R., Kastelic V., Demircioglu M.B., Garcia-Moreno D., Nemser E.S., Petricca P., Sboras S.P. et al., 2013. The European Database of Seismogenic Faults (EDSF) compiled in the framework of the Project SHARE. <http://diss.rm.ingv.it/share-edsf>, doi: 10.6092/INGV.IT-SHARE-EDSF.

- Beutler, G., Bock, H., Brockmann, E., Dach, R., Fridez, P., Gurtner, W., Hugentobler, U., Ineichen, D., Johnson, J., Meindl, M., Mervart, L., Rothacher, M., Schaer, S., Springer, T. and Weber, R., 2001. Bernese GPS Software Version 4.2 edited by U. Hugentobler, Schaer S. & Fridez P., Astronomical Institute, University of Berne, Switzerland.
- Bohnhoff, M., Rische, M., Meier, Th., Becker, D., Stavrakakis, G. and Harjes H-P., 2006. Microseismic activity in the Hellenic Volcanic Arc, Greece, with emphasis on the seismotectonic setting of the Santorini-Amorgos zone. *Tectonophysics*, 423, 17-33.
- Bond, A. and Sparks, R.S.J., 1976. The Minoan Eruption of Santorini, Greece, *Journal of the Geological Society*, 132, 1-16; doi: 10.1144/gsjgs.132.1.0001.
- Boyce, J. A. and Gertisser, R., 2012. Variations in welding characteristics within the Plinian air-fall deposit of the Middle Pumice eruption, Santorin, Greece, *J. Volcanol. Geoth. Res.*, 221–222, 71–82.
- Bott, M.H.P., 1960. The use of rapid computing methods for direct interpretation of sedimentary basins, *Geophys. J. Royal Astr. Soc.*, 3, (1), 63-67.
- Briqueu, L. and Lancelot, J.R., 1984. A geochemical study of Nea-Kameni hyalodacites (Santorini volcano, Aegean island arc). Inferences concerning the origin and effects of solfataras and magmatic evolution. *J. Volcanol. Geoth. Res.*, 20, 41—54; doi: 10.1016/0377-0273(84)90065-9
- Budetta, G., Condarelli, D., Fytikas, M., Kolios, N., Pascale, G., Rapolla, A., Pinna, E., 1984. Geophysical prospecting on the Santorini Islands. *Bulletin Volcanologique*, 47(3), 447-466.
- Chen, T., Newman, A.V., Feng, L. and Fritz, H.M., 2009. Slip Distribution from the 1 April 2007 Solomon Islands Earthquake: A Unique Image of Near-Trench Rupture, *Geophys. Res. Lett.*, 36, L16307, doi: 10.1029/2009GL039496.
- Dach, R., Hugentobler, U., Fridez, P., Meindl, M., 2007. Bernese GPS Software Version 5.0. Astronomical Institute, University of Bern, Bern.
- Delibasis, N., Chailas, S. and Lagios, E., 1989. Surveillance of Thera Volcano-Microseismicity Monitoring. Proc. 3rd Intern. Congress “Thera and the Aegean World”, 2, Sept. 3-9, Santorini, Greece, 109-206.
- Dimitriadis, I., Karagianni, E., Panagiotopoulos, D., Papazachos, C., Hatzidimitriou, P., Bohnhoff, M., Rische, M. and Meier, T., 2009. Seismicity and active tectonics at Coloumbo Reef (Aegean Sea, Greece): Monitoring an active volcano at Santorini Volcanic Center using a temporary seismic network, *Tectonophysics*, 465 (2009) 136–149; doi: 10.1016/j.tecto.2008.11.005.
- Doxa C., Sakkas V., Tzani A. and Kranis H., 2019. Contemporary Kinematics of the South Aegean Area Detected with Differential GNSS Measurements, Proceedings, 15th Int. Congress of the Geol. Soc. Greece, Athens, 22 -24 May, 2019 in Bull. Geol Soc. Greece, Sp. Pub. 7 Ext. Abs. GSG2019-328, pp 175-176; <https://ejournals.epublishing.ekt.gr/index.php/geosociety/issue/view/1265>.
- Drakopoulos, J., Makropoulos, C., Stavrakakis, G., Panagiotopoulos, D., Papanastasiou, D., Hatzidimitriou, P., Papazachos, C., Vargemesis, G. and Savvaidis, A., 1996. Seismic monitoring of Santorini Volcano: Seismological network and processing of the seismological data. *Santorini Volc. Lab.*, II, 15.
- Druitt, T. H., 2014. New insights into the initiation and venting of the Bronze-Age eruption of Santorini (Greece), from component analysis. *Bulletin of Volcanology* 76, 794; doi: 10.1007/s00445-014-0794-x.
- Druitt, T.H., Edwards, L., Mellors, R.M., Pyle, D.M., Sparks, R.S.J., Lanphere, M., Davies, M. and Barreiro, B., 1999. Geological Map of the Santorini Islands, 1:20000. Geological Society of London, Memoir 19, 178p.
- Druitt, T.H. and Francaviglia, V., 1992. Caldera formation on Santorini and the physiography of the islands in the late Bronze Age, *Bull. Volcanol.*, 54, 484- 493.
- Druitt, T.H., Mellors, R.A., Pyle, D.M. and Sparks, R.S.J., 1989. Explosive volcanism on Santorini, Greece, *Geological Magazine*, 126, 95–126.
- EMODnet Bathymetry Consortium (2016): EMODnet Digital Bathymetry (DTM). <https://doi.org/10.12770/c7b53704-999d-4721-b1a3-04ec60c87238>

- Feng, L., Newman, A.V., Protti, J.M., González, V., Jiang, Y. and Dixon, T.H., 2012. Active deformation near the Nicoya Peninsula, northwestern Costa Rica, between 1996 and 2010: Interseismic megathrust coupling, *J. Geophys. Res.*, 117, B06407, doi: 10.1029/2012JB009230.
- Ferrara, G., Fytikas, M., Guiliano, O. and Marinelli, G., 1980. Age of the formation of the Aegean active volcanic arc. In Doulas C. (ed), *Thera and the Aegean World II*, The Thera Foundation, London, vol. 2, 37-41.
- Feuillet, N., 2013. The 2011–2012 unrest at Santorini rift: stress interaction between active faulting and volcanism. *Geophys. Res. Lett.* 40 (14), 3532–3537; doi: 10.1002/grl.50516.
- Foumelis, M., Trasatti, E., Papageorgiou, E., Stramondo, S. and Parcharidis, I., 2013. Monitoring Santorini volcano (Greece) breathing from space, *Geophys. J. Int.*, 193 (1), 161–170; doi: 10.1093/gji/ggs135.
- Fouqué, F., 1879. *Santorin et ses éruptions*. Masson et Cie., Paris, 440p.
- Fytikas, M., Karydakis, G., Kavouridis, Th., Kolios, N., Vougioukalakis, G., 1989. Geothermal Research on Santorin. In: ‘Thera and the Aegean World III’, Volume Two: ‘Earth Sciences’, Proceedings of the Third International Congress. Santorin, Greece, 3-9 September 1989. Publisher: Thera Foundation (1990) ISBN: 0950613371”, 241 – 249.
- Gardner J.E., Thomas R.M.E., Jaupart C., Tait S., 1996. Fragmentation of magma during Plinian volcanic eruptions. *Bulletin of Volcanology*, 58, 144–162.
- Georgalas, G., 1953. L' éruption du volcan de Santorin en 1950. *Bull. Volcanol.*, 13, 39-55.
- Georgalas, G., Papastamatiou, J., 1953. L' eruption du volcan du Santorin en 1939-41; L' éruption du dome Fouqué. *Bull. Volcanol.*, 13, 3-18.
- Heiken, G. and McCoy, F., 1984. Caldera development during the Minoan eruption, Thera, Cyclades, Greece. *J. Geophys. Res.*, 89, 8441-8462.
- Hooft E.E.E., Heath B.A., Toomey D.R., Paulatto M., Papazachos C.B., Nomikou P., Morgan J.V. and Warner M.R., 2019. Seismic imaging of Santorini: Subsurface constraints on caldera collapse and present-day magma recharge. *Earth and Planetary Science Letters* 514, 48–61; doi: 10.1016/j.epsl.2019.02.033.
- Hutton, D.H.W., 1996. The ‘space problem’ in the emplacement of granite, *Episodes*, 19 (4), 114-119.
- I.G.M.E., 1995. Surficial sediment map of the bottom of the Aegean Sea, Scale 1:200,000: Santorini sheet, IGME, Athens, Greece.
- Johnston, E.N., Sparks, R.S.J., Nomikou, P., Livanos, I., Carey, S., Phillips, J.C, and Sigurdsson, H., 2015. Stratigraphic relations of Santorini’s intracaldera fill and implications for the rate of post-caldera volcanism, *Journal of the Geological Society*, 172, 323-335; doi: 10.1144/jgs2013-114
- Junge, A., 1990. Robust estimation of bivariate transfer functions. In Haak, V. and Homilius, H. (eds), *Protokoll Kolloquium Elektromagnetische Tiefenforschung*, pp. 75-86, DGG, Hornburg, Germany (in German)
- Junge, A., 1992. On the effective number of degrees of freedom in magnetotelluric transfer function estimation. In Haak, V. and Rodemann, H. (eds), *Protokoll Kolloquium Elektromagnetische Tiefenforschung*, pp. 139-158, DGG, Borkheide, Germany (in German)
- Junge, A., 1994. Induced telluric fields – new observations in North Germany and the Bramwald, *Habilitation Thesis*, Faculty of Physics, University of Göttingen, Germany (in German).
- Kaviris, G., Papadimitriou, P., Kravvariti, Ph., Kapetanidis, V., Karakonstantis, A., Voulgaris, N., and Makropoulos, K., 2015. A detailed seismic anisotropy study during the 2011–2012 unrest period in the Santorini Volcanic Complex, *Physics of the Earth and Planetary Interiors*, 238, 51-88; doi: 10.1016/j.pepi.2014.11.002.
- Kolaitis A., Papadimiriou P., Kassaras I. and Makropoulos K., 2007. Seismic observations with broadband instruments at Santorini Volcano, *Bull. Geol. Soc. Greece*, 40 (3), 1150-1161; <http://geolib.geo.auth.gr/digeo/index.php/bgs/article/view/4675/4487>.
- Konstantinou, K.I., Evangelidis, C.P., Liang, W.-T., Melis, N.S. and Kalogeras, I., 2013. Seismicity, Vp/Vs and shear wave anisotropy variations during the 2011 unrest at Santorini caldera, southern Aegean, *J. Volcanol. Geoth. Res.* 267, 57-67; doi: 10.1016/j.jvolgeores.2013.10.001.
- Ktenas, K., 1927. L' eruption du volcan des Kammenis (Santorin) en 1925, II, *Bull. Volcanol.*, 4: 7-46.

- Lagios, E., Sakkas, V., Novali, F., Ferretti, A., Damiata, B.N. and Dietrich, V.J., 2017. Reviewing and Updating (1996–2012) Ground Deformation in Nisyros Volcano (Greece) Determined by GPS and SAR Interferometric Techniques (1996–2012). In: *Dietrich, V.J. and Lagios, E. (eds), "Nisyros Volcano: The Kos - Yali - Nisyros Volcanic Field"*, Active Volcanoes of the World, Springer Verlag, 285–301; doi: 10.1007/978-3-319-55460-0
- Lagios, E., Sakkas, V., Novali, F., Belloti, F., Ferretti, A., Vlachou, K. and Dietrich, V., 2013. SqueeSAR™ and GPS ground deformation monitoring of Santorini Volcano (1992–2012): Tectonic implications, *Tectonophysics*, 594, 38–59; doi: 10.1016/j.tecto.2013.03.012.
- Lagios, E., Sakkas, V., Parcharidis, Is. And Dietrich, V., 2005. Ground deformation of Nisyros Volcano (Greece) for the period 1995–2002: Results from DInSAR and DGPS observations, *Bull. Volcanol.* 68, 201–214; doi: 10.1007/s00445-005-0004-y.
- Mellors, R.A., Sparks, R.S.J., 1991. Spatter-rich pyroclastic flow deposits on Santorin, Greece. *Bulletin of Volcanology*, 53, 327–342.
- Mortazavi, M. and Sparks, R. S. J., 2004. Origin of rhyolite and rhyodacite lavas and associated mafic inclusions of Cape Akrotiri, Santorin: the role of wet basalt in generating calcalkaline silicic magmas. *Contributions to Mineralogy and Petrology* 146, 397–413.
- Mountrakis, D., Pavlides, S., Chatzipetros, A., Meletidis, S., Tranos, M., Vougioukalakis, G. and Kiliass, A., 1998. Active deformation in Santorini. In: Casale R., Fytikas M., Sigvaldarsson G. & Vougioukalakis G. (eds): *The European laboratory volcanoes*. European Commission, EUR 18161, 13–22.
- National Geophysical Data Center (2012) GEODAS Marine trackline geophysics – Gravity, bathymetry, seismic, geophysical data.
- Newman, A.V., Stiros, S., Feng, L., Psimoulis, P., Moschas, F., Saltogianni, V., Jiang, Y., Papazachos, K., Panagiotopoulos, D., Karagianni, E., Vamvakaris, D., 2012. Recent geodetic unrest at Santorin Caldera, *Geophys. Res. Lett.*, 39, L06309; doi: 10.1029/2012GL051286.
- Nomikou, P., Carey, S., Papanikolaou, D., Croff Bell, K., Sakellariou, D., Alexandri, M. and Bejelou, K., 2012. Submarine volcanoes of the Columbo Volcanic Zone NE of Santorini Caldera, Greece, *Glob. Planet. Change*, 90–91, 135–151; doi: 10.1016/j.gloplacha.2012.01.001.
- Nomikou, P., Druitt, T.H., Hübscher, C., Mather, T.A., Paulatto, M., Kalnins, L.M., Kelfoun, K., Papanikolaou, D., Bejelou, K., Lampridou, D., Pyle, D.M., Carey, S., Watts, A.B., Weiß, B. and Parks, M.M., 2016. Post-eruptive flooding of Santorini caldera and implications for tsunami generation, *Nature Communications*, 7, 13332, doi: 10.1038/ncomms13332.
- Okada, Y., 1985. Surface deformation due to shear and tensile faults in a half-space, *Bull. Seism. Soc. Am.* 75, 1135–1154.
- Okal, E.A., Synolakis, C.E., Uslu, B., Kalligeris, N. and Voukouvalas, E., 2009. The 1956 earthquake and tsunami in Amorgos, Greece, *Geophys. J. Int.*, 178 (3), 1533–1554; doi: 10.1111/j.1365-246X.2009.04237.x
- Papadimitriou, P., Kapetanidis, V., Karakonstantis, A., Kaviris, G., Voulgaris, N. and Makropoulos, K., 2015. The Santorin Volcanic Complex: A detailed multi-parameter seismological approach with emphasis on the 2011–2012 unrest period. *Journal of Geodynamics*, 85, 32–57; doi: 10.1016/j.jog.2014.12.004
- Papageorgiou, E., Tzanis, A., Sotiropoulos, P. and Lagios, E., 2010. DGPS and Magnetotelluric constraints on the contemporary tectonics of the Santorin Volcanic Complex, Greece. *Bull. Geol. Soc. Greece*, 43, 344–356; doi: 10.12681/bgsg.11186.
- Papageorgiou, E., Lagios, E., Vassilopoulou, S. and Sakkas, V., 2007. Vertical and horizontal ground deformation of Santorini Island deduced by DGPS measurements, *Bull. Geol. Soc. Greece*, 40 (3), 1219–1225; <http://geolib.geo.auth.gr/digeo/index.php/bgsg/article/view/4681/4493>.
- Papoutsis, I., Papanikolaou, X., Floyd, M., Ji, K.H., Kontoes, C., Paradissis, D. and Zacharis, V., 2013. Mapping inflation at Santorini volcano, Greece, using GPS and InSAR, *Geophys. Res. Lett.*, 40, 267–272; doi: 10.1029/2012GL054137.
- Parks, M.M., Caliro, S., Chiodini, G., Pyle, D.M., Mather, T.A., Berlo, K., Edmonds, M., Juliet Biggs, J., Nomikou, P. and Raptakis, K., 2013. Distinguishing contributions to diffuse CO<sub>2</sub> emissions in volcanic areas from magmatic degassing and thermal decarbonation using soil gas <sup>222</sup>Rn–δ<sup>13</sup>C

- systematics: Application to Santorin volcano, Greece. *Earth and Planetary Science Letters*, 377–378, 180-190; doi: 10.1016/j.epsl.2013.06.046.
- Pavlis, N.K., Holmes, S.A., Kenyon, S.C. and Factor, J.K., 2008. An Earth Gravitational Model to Degree 2160: EGM2008. EGU General Assembly 2008, Vienna, Austria, April 13-18.
- Pe-Piper, G. and Piper, D.J.W., 2005. The South Aegean active volcanic arc: relationships between magmatism and tectonics. *Developments in Volcanology*, 7, 113-133; doi: 10.1016/S1871-644X(05)80034-8.
- Perissoratis, C. 1995. The Santorin volcanic complex and its relation to the stratigraphy and structure of the Aegean arc, Greece, *Marine Geology*, 128, 37–58.
- Perissoratis, C., 1990. Marine Geological Research on Santorin: Preliminary Results. In: Hardy D.A., Keller J., Galanopoulos, V.P., Flemming, N.C. and Druitt, T.H. (eds), *Thera and the Aegean World III*, The Thera Foundation, London, vol. 2, 305 – 311.
- Pesci, A., Teza, G., 2007. Strain rate analysis over the central Apennines from GPS velocities: the development of a new free software. *Bollettino di Geodesia e Scienze Affini*, 56, 69–88.
- Petford N., Cruden A.R., McCaffrey K.J. and Vigneresse J.L., 2000. Granite magma formation, transport and emplacement in the Earth's crust, *Nature*, 408 (6813), 669-73; doi: 10.1038/35047000.
- Pichler, H. and Kussmaul, S., 1980. Comments on the geological map of the Santorini Islands. In: Doulas, C. (ed.) *Thera and the Aegean World II*, The Thera Foundation, London, 413-427.
- Pichler, H., Guenther, D. and Kussmaul, S., 1980. *The Geological Map of Greece, Thira Island*, Inst. Geol Min. Exploration, Athens 1980.
- Pyle, D.M., 1990. New estimates for the volume of the Minoan eruption. In: Hardy D.A., Keller J., Galanopoulos, V.P., Flemming, N.C. and Druitt, T.H. (eds), *Thera and the Aegean World III*, The Thera Foundation, London, vol. 2, 113-121
- Radhakrishna Murthy, I.V., Rama Rao, P. and Ramakrishna, P., 1989. Gravity Anomalies of Three-dimensional Bodies with Variable Density Contrast, *Pure Appl. Geophys.*, 130(4), 711-719.
- Radhakrishna Murthy, I.V., Rama Rao, P. and Jagannardha Rao, S., 1990. The density difference and generalized programs for two and three-dimensional gravity modelling, *Computers and Geosciences*, 16(3), 277-287.
- Reck, H., 1936. *Santorini. - Der Werdergang eines Inselvulcans und sein Ausbruch 1925 - 1928*. Dietrich Reimer, Berlin, 3 vols.
- Ritter, O., Junge, A. and Dawes, G.J.K, 1998. New equipment and processing for magnetotelluric remote reference observations. *Geophys. J. Int.*, 132, 535-548; doi: 10.1046/j.1365-246X.1998.00440.x
- Rodi, W. and Mackie, R.L., 2001. Nonlinear conjugate gradients algorithm for 2-D magnetotelluric inversion, *Geophysics*, 66, 174–187.
- Rokityansky, I.I., 1982. *Geoelectromagnetic investigation of the Earth's crust and mantle*, Springer, Berlin, pp. 286-288.
- Sakellariou D., and Tsampouraki-Kraounaki K., 2019. Plio-Quaternary extension and strike-slip tectonics in the Aegean, in: J. Duarte (Ed.), *Transform Plate Boundaries and Fracture Zones*, Chapter 14, pp. 339-374; doi: 10.1016/B978-0-12-812064-4.00014-1; ISBN: 978-0-12-812064-4; Elsevier 2019.
- Sakellariou D., Rousakis G., Sigurdsson H., Nomikou P., Katsenis I., Croff Bell K.L. and Carey S., 2012. Seismic stratigraphy of Santorin's Caldera: A contribution to the understanding of the Minoan eruption. *Proceedings, 10th Hellenic Symposium on Oceanography and Fisheries*, 7-11 May 2012, Athens, Greece; 9pp.
- Sakellariou D., Sigurdsson H., Alexandri M., Carey S., Rousakis G., Nomikou P., Georgiou P. and Ballas, D., 2010. Active tectonics in the Hellenic volcanic arc: The Kolumbo submarine volcanic zone. *Bull. Geol. Soc. Greece*, XLIII, 2, 1056-1063; doi: 10.12681/bgs.11270.
- Seidenkrantz, M. and Friedrich, W.L., 1993. Santorini, part of the Hellenic arc: age of the earliest volcanism documented by foraminifera. *Bull. Geol. Soc. Greece*, 28 (3), 99-115; <http://geolib.geo.auth.gr/digeo/index.php/bgs/article/view/7073/6830>.
- Shorin, H., 1980. Zersetzung von Kalk-Alkali-Gesteinen im rezenten Fumarolengebiet auf Nea Kameni/Santorin / Griechenland. *Geologische Rundschau*, 69, 226-244.

- Sigurdsson, H., Carey, S., Alexandri, M., Vougioukalakis, G., Croff, K., Roman, C., Sakellariou, D., Anagnostou, C., Rousakis, G., Ioakim, C., Gogou, A., Ballas, D., Misaridis, T. and Nomikou, P., 2006). Marine Investigations of Greece's Santorini Volcanic Field. *Eos*, 87 (34), 337–342; doi: 10.1029/2006EO340001
- Sotiropoulos P., Galanopoulos D., Lagios E. and Dawes G.J.K., 1996a. An Audio-Magnetotelluric (AMT) survey on Santorini Volcano, Greece. In Proc., 2<sup>nd</sup> Workshop on European Laboratory Volcanoes, May 2-4, Santorin, Greece, 281-295.
- Sotiropoulos P., Galanopoulos D., Lagios E. and Dawes G.J.K., 1996b. One-Dimensional Magnetotelluric modelling of Thera Volcano, Greece. 1st Congress of Balkan Geophysical Society, Sept. 23-27, Athens, Greece.
- Stevenson C., 2009. The relationship between forceful and passive emplacement: The interplay between tectonic strain and magma supply in the Rosses Granitic Complex, NW Ireland, *Journal of Structural Geology*, 31 (3), 270-287; doi: 10.1016/j.jsg.2008.11.009
- Tassi, F., Vaselli, O., Papazachos, C.B., Giannini, L., Chiodini, G., Vougioukalakis, G.E., Karagianni, E., Vamvakaris, D. and Panagiotopoulos, D., 2013. Geochemical and isotopic changes in the fumarolic and submerged gas discharges during the 2011–2012 unrest at Santorini caldera (Greece), *Bull. Volcanol.*, 75, 711-726; doi: 10.1007/s00445-013-0711-8.
- Tsampouraki-Kraounaki K. and Sakellariou D., 2017. Strike-slip deformation behind the Hellenic subduction: The Amorgos Shear Zone, South Aegean Sea. Proc. 8th International INQUA Meeting on Paleoseismology, Active Tectonics and Archeoseismology, p.392-395
- Tzanis, A., 2014. The Characteristic States of the Magnetotelluric Impedance Tensor: Construction, analytic properties and utility in the analysis of general Earth conductivity distributions. [arXiv:1404.1478](https://arxiv.org/abs/1404.1478) [physics.geo-ph]. Accessed, September 2019.
- Urbanski, N.A., 2003. Eruption dynamics during Plinian eruptions: Insights from the stratigraphic variations of deposit structures and pumice textures of the Minoan eruption (Santorin, Greece) and the Laacher See eruption (East Eifel, Germany). PhD Thesis, Christian-Albrechts-Universität, Kiel, 162 pp.; URL: <http://oceanrep.geomar.de/id/eprint/31078> (accessed May 2018).
- Vallianatos, F., Michas, G., Papadakis G. and Tzanis, A., 2013. Evidence of non-extensivity in the seismicity observed during the 2011-2012 unrest at the Santorini volcanic complex, Greece. *Natural Hazards and Earth System Science*, 13, 177-185; doi: 10.5194/nhess-13-177-2013.
- Vasiliadis, K. C., 1985. Geophysical Survey of Thira Island (Santorin) in the frame of the Geothermal program of IGME. Internal Report., 10 pp. (in Greek).
- Washington, H. S., 1926. Santorini eruption of 1925. *Bull. Geol. Soc. Am.*, 37: 349 -384.
- Wessel, P., Smith, W.H.F., Scharroo, R., Luis, J.F. and Wobbe, F., 2013. Generic Mapping Tools: Improved version released, *EOS Trans. AGU*, 94, 409-410; doi: 10.1002/2013EO450001.
- Whitham, A.G. and Sparks, R.S.J., 1986. Pumice. *Bulletin of Volcanology*, 48, 209-223.
- Wilson, C..J.N. and Houghton, B.F., 1990. Eruptive mechanisms in the Minoan Eruption: evidence from pumice vesicularity. In: Hardy, D.A. (ed.), *Thera and the Aegean World III*, vol. 2, “The Thera Foundation”, London, 122-128.
- Yokoyama, I. and Bonasia, V., 1971. A preliminary gravity survey on Thera Volcano, Greece. *Acta Sci.* 1st Congr. Volcano Thera, 328-336.
- Yokoyama, I., Bonasia, V., 1979. Gravity anomalies on the Thera Islands. In C. Doulmas, (ed.). *Thera and the Aegean World I*, 147-150.

**TABLE 1**

**Table 1:** Summary of measured density values of non-pyroclastic formations measured for the purposes of the present study. The description and codes of the lithological formations are after Druitt et al. (1999).

<b>FORMATION*</b>	<b>Description</b>	<b>Density (g/cm<sup>3</sup>)</b>
<b>Alpine Basement</b>		
Metapelites (Mp)	Mt. Prof Elias	2.61 ± 0.050
Limestones of Prof. Elias (MI)	Marbles Mt. Prof Elias	2.71 ± 0.020
<b>Volcanic Extrusives</b>		
Peristeria Volcano (av3)	Basaltic/ andesitic lavas, tuffs and breccia	2.45 ± 0.050
Akrotiri Rhyodacites (rl)		2.1 ± 0.030
Middle Tuffs (ap4a)	Red Scoria	1.805 ± 0.100
Middle Tuffs (ap4b)	Lava flow	2.475 ± 0.050
Skaros lava shield (as2)	basaltic to andesitic lava flows	2.55 ± 0.050
Oia lavas (ao)	Andesitic lavas	2.35 ± 0.050

**TABLE 2**

**Table 2:** The East ( $\Delta E$ ), North ( $\Delta N$ ) and up ( $\Delta U$ ) components of displacement relative to Station 7, detected by the GPS network of the Division of Geophysics, NKUA, over the periods 1994-2005 and 1994-2012.

ID	Longitude E (°)	Latitude N (°)	1994 - 2005						1994 - 2012					
			$\Delta E$ (m)	$\sigma_{\Delta E}$	$\Delta N$ (m)	$\sigma_{\Delta N}$	$\Delta U$ (m)	$\sigma_{\Delta U}$	$\Delta E$ (m)	$\sigma_{\Delta E}$	$\Delta N$ (m)	$\sigma_{\Delta N}$	$\Delta U$ (m)	$\sigma_{\Delta U}$
2	25.3591	36.3572	-0.0238	0.0024	0.031	0.0029	-0.0159	0.0067	-0.07	0.0028	0.0326	0.0033	-0.0232	0.0077
4	25.3967	36.3560	-0.0175	0.0040	0.0202	0.0042	0.0087	0.0094	-0.0501	0.0042	0.018	0.0044	-0.0013	0.0099
5	25.3967	36.4064	-	0.0023	-	0.0028	-	0.0059	-0.0383	0.0015	-0.0584	0.0017	-0.0251	0.0039
6	25.4175	36.3571	-0.02	0.0031	0.0051	0.0035	0.0217	0.0083	-0.0382	0.0031	-0.0027	0.0035	0.0072	0.0084
7	25.4516	36.3669	0	-	0	-	0	-	0	-	0	-	0	-
12	25.4221	36.4326	-0.016	0.0022	-0.0037	0.019	0.0224	0.0485	-	-	-	-	-	-
15	25.3998	36.4102	-0.014	0.0013	-0.0019	0.0016	-0.0148	0.0035	-0.0252	0.0015	-0.0297	0.0017	0.0093	0.0039
18	25.4312	36.4131	-0.0042	0.0012	0.0009	0.0014	0.0377	0.0033	0.0324	0.0020	0.0226	0.0022	0.0496	0.0052
22	25.4003	36.4084	-0.0129	0.0034	-0.0064	0.0040	-0.0224	0.0092	-0.0313	0.0018	-0.0419	0.0020	0.0014	0.0046
26	25.4039	36.4626	-0.0243	0.0018	0.005	0.0024	0.0232	0.0053	-0.0378	0.0017	0.1474	0.0019	0.0605	0.0042
27	25.4790	36.4073	0.0131	0.0014	-0.0089	0.0018	0.0387	0.0038	0.0278	0.0025	0.0047	0.0029	0.0249	0.0065
29	25.3836	36.4617	-0.0186	0.0012	0.0091	0.0014	0.0248	0.0031	-0.0756	0.0013	0.1678	0.0015	0.0517	0.0034
33	25.4214	36.4728	-0.0166	0.0014	0.0063	0.0018	0.037	0.0038	-0.042	0.0023	0.1281	0.0027	0.0346	0.0060
43	25.4237	36.4529	-0.0104	0.0012	-0.001	0.0014	0.0349	0.0031	0.0089	0.0017	0.1107	0.0020	0.0625	0.0044
45	25.3967	36.4041	-0.0113	0.0013	-0.0179	0.0016	-0.0619	0.0035	-0.0406	0.0015	-0.0733	0.0017	-0.0478	0.0039
56	25.3446	36.4338	-0.0132	0.0019	0.0129	0.0023	0.0068	0.0051	-0.1541	0.0021	0.0985	0.0024	0.0289	0.0054
57	25.3451	36.4296	-0.0107	0.0019	0.018	0.0023	0.0096	0.0051	-0.1597	0.0021	0.0857	0.0024	0.0337	0.0054
99	25.4386	36.3464	-0.0033	0.0020	0.0018	0.0023	0.0122	0.0054	-0.018	0.0019	0.0038	0.0022	0.0024	0.0052
SANT	25.4226	36.4336	-	-	-	-	-	-	0.0253	0.0031	0.0757	0.0022	0.0695	0.0051

**TABLE 3****Table 3:** The East ( $\Delta E$ ), North ( $\Delta N$ ) and up ( $\Delta U$ ) components of the displacement relative to Station 7, over the periods 2005-2012 and 1994-2017.

ID	Longitude E (°)	Latitude N (°)	2005 - 2012						1994 - 2017					
			$\Delta E$ (m)	$\sigma_{\Delta E}$	$\Delta N$ (m)	$\sigma_{\Delta N}$	$\Delta U$ (m)	$\sigma_{\Delta U}$	$\Delta E$ (m)	$\sigma_{\Delta E}$	$\Delta N$ (m)	$\sigma_{\Delta N}$	$\Delta U$ (m)	$\sigma_{\Delta U}$
2	25.3591	36.3572	-0.0462	0.0028	0.0016	0.0033	-0.0073	0.0074	-0.0596	0.0024	0.0447	0.0029	-0.0341	0.0068
4	25.3967	36.3560	-0.0326	0.0029	-0.0022	0.0034	-0.01	0.0077	-0.0413	0.0040	0.0234	0.0042	-0.0229	0.0095
5	25.3967	36.4064	-		-		-		-0.038	0.0023	-0.0659	0.0028	-0.0647	0.0060
6	25.4175	36.3571	-0.0182	0.0024	-0.0078	0.0028	-0.0145	0.0062	-0.0173	0.0030	0.0011	0.0035	-0.0078	0.0083
7	25.4516	36.3669	0	-	0	-	0	-	0	-	0	-	0	-
12	25.4221	36.4326	-	-	-	-	-	-	-	-	-	-	-	-
15	25.3998	36.4102	-0.0112	0.0046	-0.0278	0.0055	0.0241	0.0123	-0.0328	0.0013	-0.0361	0.0016	-0.0139	0.0036
18	25.4312	36.4131	0.0366	0.0026	0.0217	0.0030	0.0119	0.0069	0.0358	0.0012	0.009	0.0014	0.0438	0.0033
22	25.4003	36.4084	-0.0184	0.0046	-0.0355	0.0056	0.0238	0.0126	-0.0387	0.0034	-0.047	0.0040	-0.0216	0.0092
26	25.4039	36.4626	-0.0135	0.0034	0.1424	0.0040	0.0373	0.0085	-0.0428	0.0018	0.1282	0.0024	0.0556	0.0053
27	25.4790	36.4073	0.0147	0.0033	0.0136	0.0040	-0.0138	0.0088	0.0474	0.0014	-0.0098	0.0017	0.0200	0.0039
29	25.3836	36.4617	-0.057	0.0028	0.1587	0.0033	0.0269	0.0072	-0.0763	0.0012	0.1409	0.0014	0.0441	0.0032
33	25.4214	36.4728	-0.0254	0.0035	0.1218	0.0041	-0.0024	0.0092	-0.0356	0.0014	0.1108	0.0018	0.0331	0.0038
43	25.4237	36.4529	0.0193	0.0027	0.1117	0.0032	0.0276	0.0072	0.0004	0.0012	0.0983	0.0014	0.0626	0.0031
45	25.3967	36.4041	-0.0293	0.0027	-0.0554	0.0031	0.0141	0.0071	-0.0411	0.0013	-0.0772	0.0016	-0.0893	0.0035
56	25.3446	36.4338	-0.1409	0.0030	0.0856	0.0036	0.0221	0.0079	-0.1413	0.0019	0.0905	0.0023	0.0138	0.0051
57	25.3451	36.4296	-0.149	0.0036	0.0677	0.0045	0.0241	0.0095	-0.1457	0.0019	0.0839	0.0023	0.0109	0.0051
99	25.4386	36.3464	-0.0147	0.0033	0.002	0.0037	-0.0098	0.0083	-0.0014	0.0020	0.0001	0.0023	-0.0175	0.0054
SANT	25.4226	36.4336	0.0413	0.0034	0.0794	0.0041	0.0471	0.0071	0.0204	0.0019	0.0639	0.0021	0.0611	0.0051

**FIGURE 1**

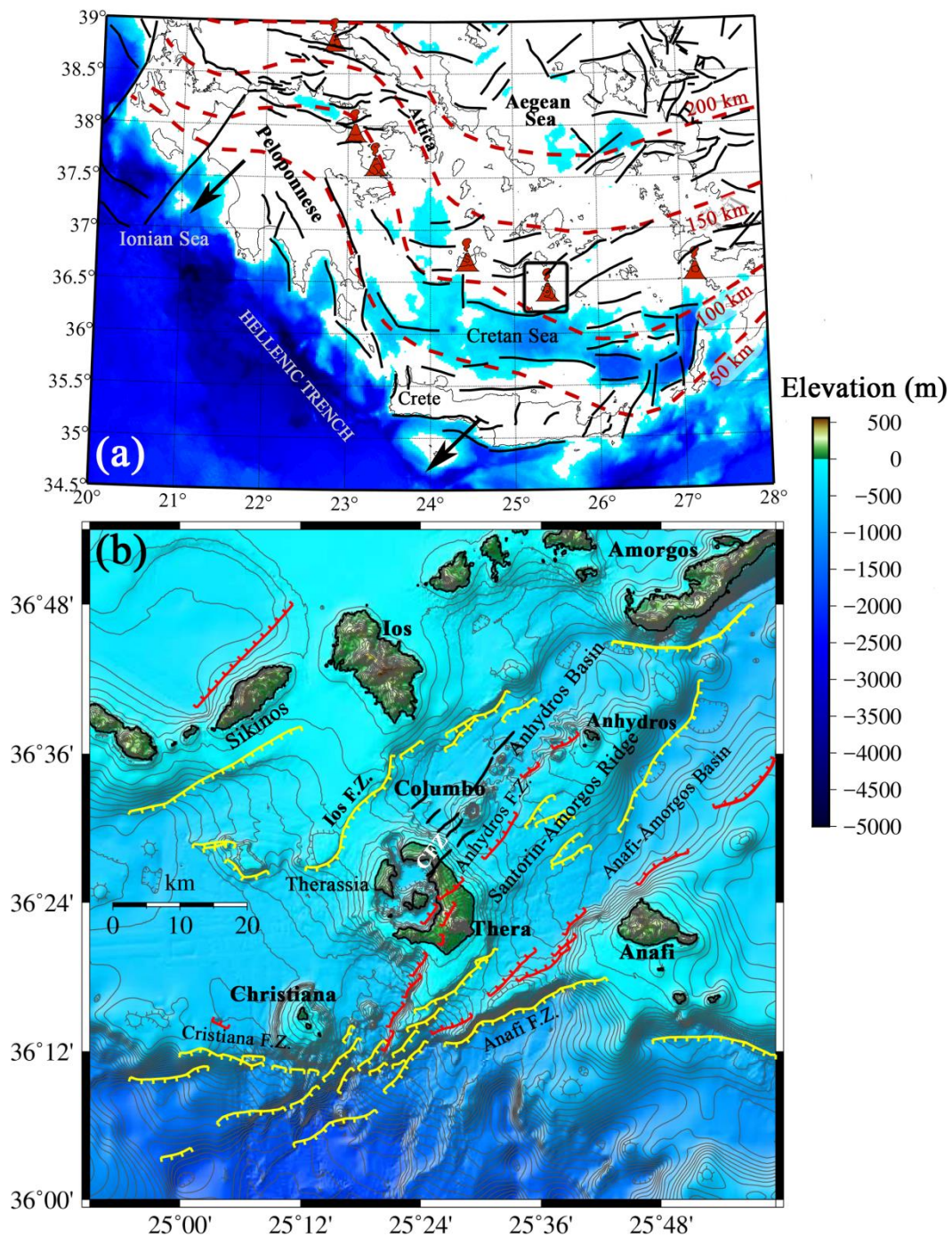


**Figure 1:** (a) Location of the Santorini Volcanic Complex (rounded rectangle) in the Hellenic Subduction System. Volcanic fields are indicated with “smoking volcano” symbols. Black arrows indicate the motion of the Aegean plate relative to the African. Red dashed lines indicate the 50, 100, 150 and 200 kilometre iso-depths of the subducting slab; black solid lines indicate main faults; both data sets were extracted from the SHARE database (Basili et al., 2013). Bathymetry was extracted from the ETOPO1 database (Amante and Eakins, 2009). (b) Tectonic setting of the broader SVC area. Southerly dipping faults are shown in yellow; northerly dipping faults in red; sub-vertical faults in black (Sections 5.4 and 6). Fault data collected from Armijo et al., (1992), Sakellariou et al., (2010), Nomikou et al., (2012) and Feuillet, (2013). The bathymetry was extracted from the EMODNet (2016) data base.

**FIGURE 2**

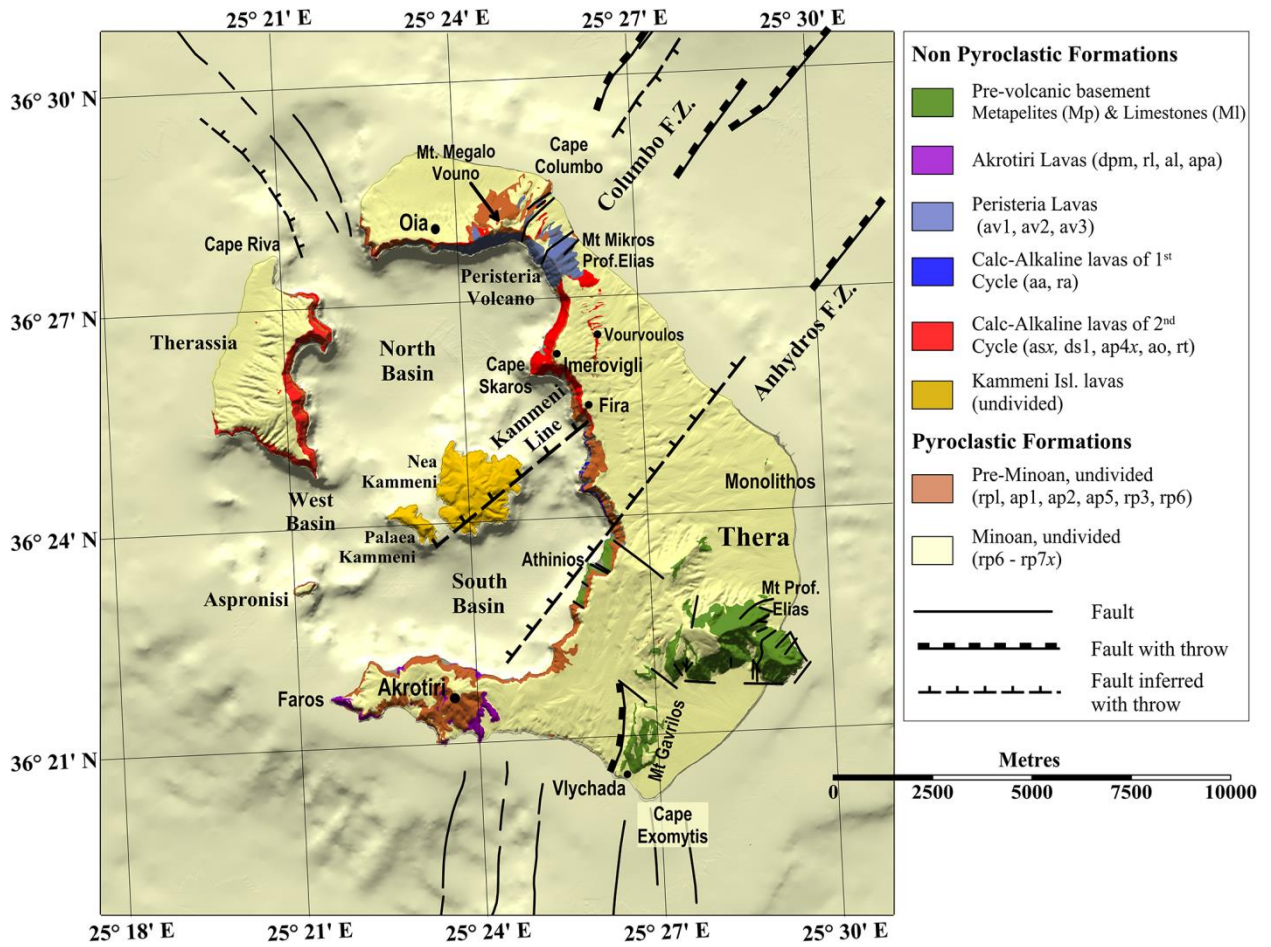


**Figure 2:** Surface geology of the Santorini Volcanic Complex superimposed on a fine (20m grid spacing) digital elevation model. The outlines of geological formations and the litho-stratigraphic codes in the legend were taken from *Druitt et al., (1999)*. Faults and tectonic lineaments have been extracted from *Druitt et al., (1999)*, *IGME (1995)*, *Sakellariou et al., (2010)* and *Papadimitriou et al., (2015)*.

**FIGURE 3**

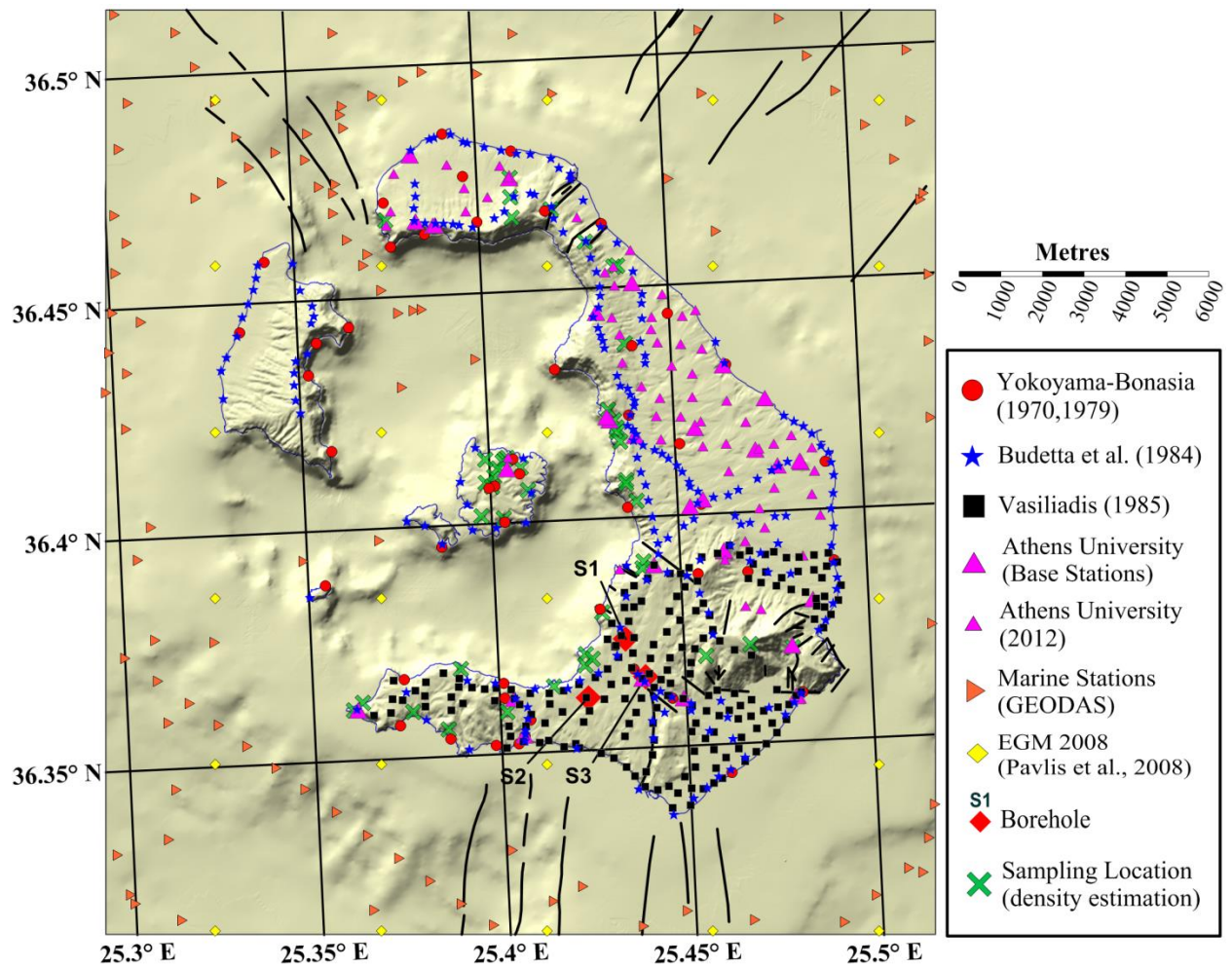


**Figure 3:** Distribution of gravity observations and density sampling sites over the SVC.

**FIGURE 4**

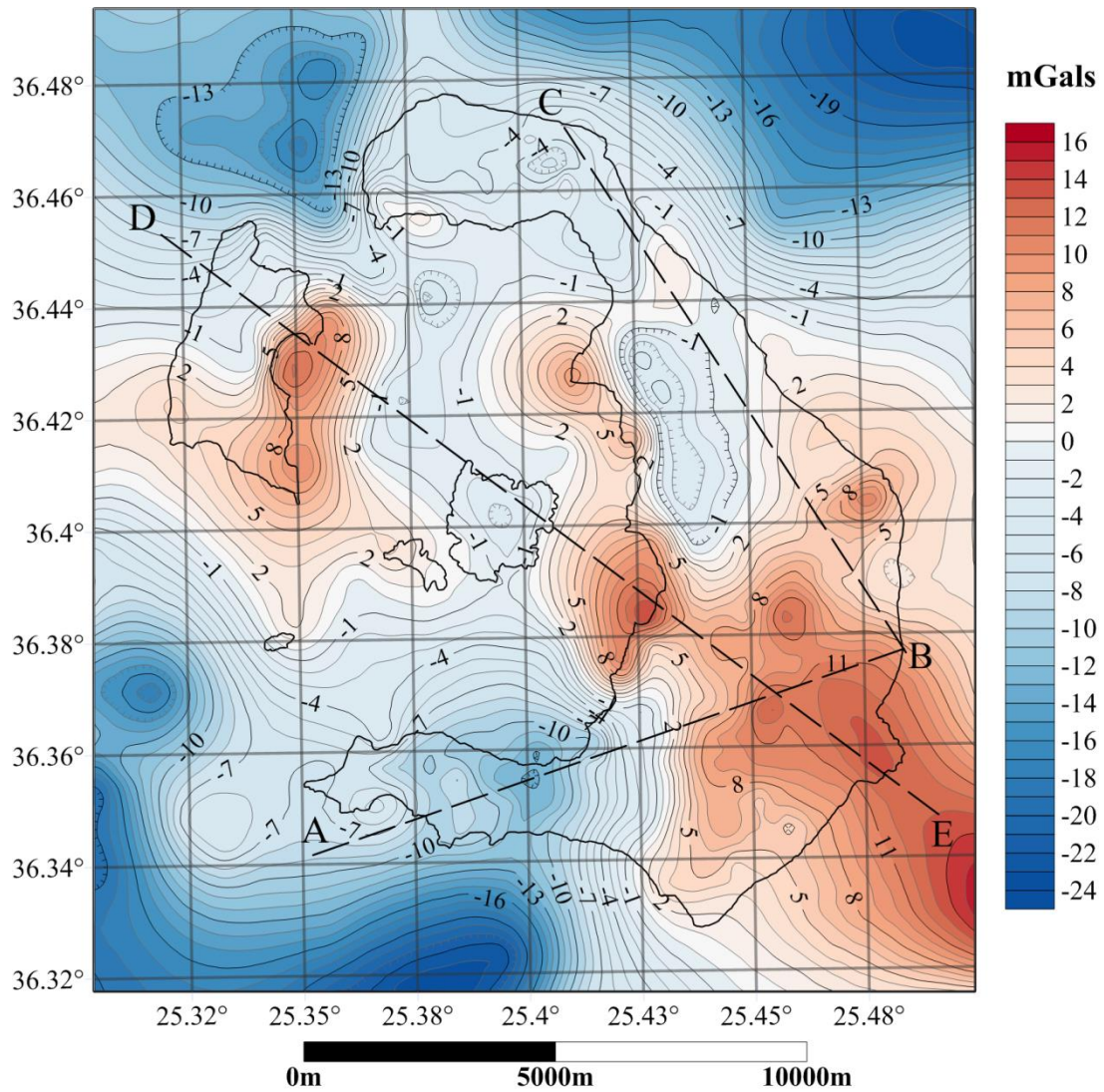


**Figure 4:** Filtered Gravity Anomaly Map of the Santorini Volcanic Complex. The dashed lines indicate the locations of profiles AB, BC and DE shown in Fig. 6.

**FIGURE 5a**

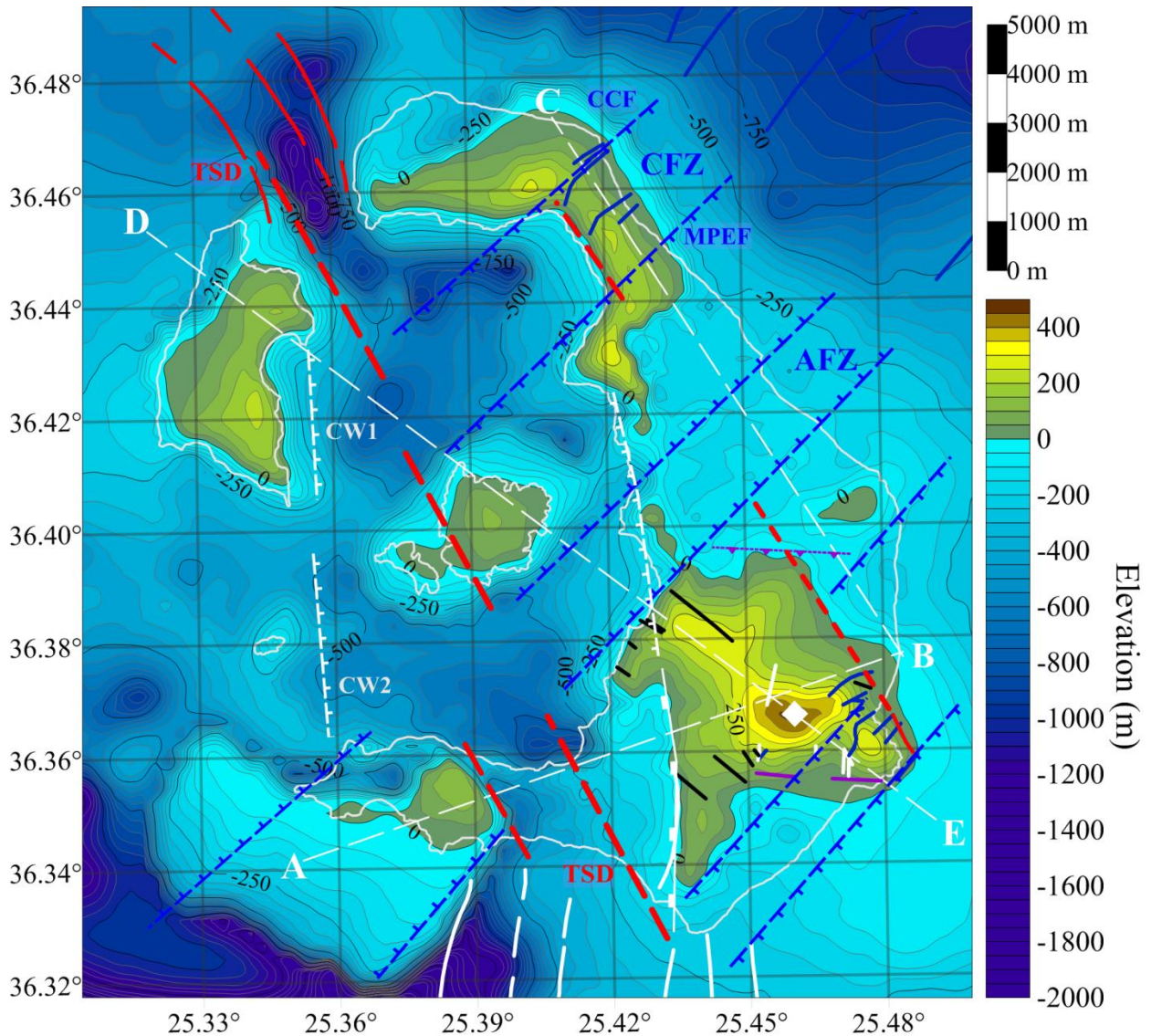


**Figure 5a:** Composite presentation of the topography of the *sub-pyroclastic basement*. Known faults are shown with solid lines. Inferred (interpreted) faults are shown with broken lines; throw/dip direction is also shown when it can also be inferred. All faults are colour-coded according to their orientation: NW-SE faults in black, NNW-SSE faults in red, N-S faults in white, NE-SW faults in blue and E-W faults in purple. Long-dashed white lines indicate the locations of profiles AB, BC and DE shown in Fig. 6. **CFZ:** Columbo Fault Zone; **CCF:** Cape Columbo Fault; **MPEF:** Mikros Prof. Elias Fault; **AFZ:** Anhydros Fault Zone; **TSD:** Trans-Santorin Divide; **CW1** and **CW2** indicate the (conjectured) boundary faults of the west flank of the caldera.

**FIGURE 5b**

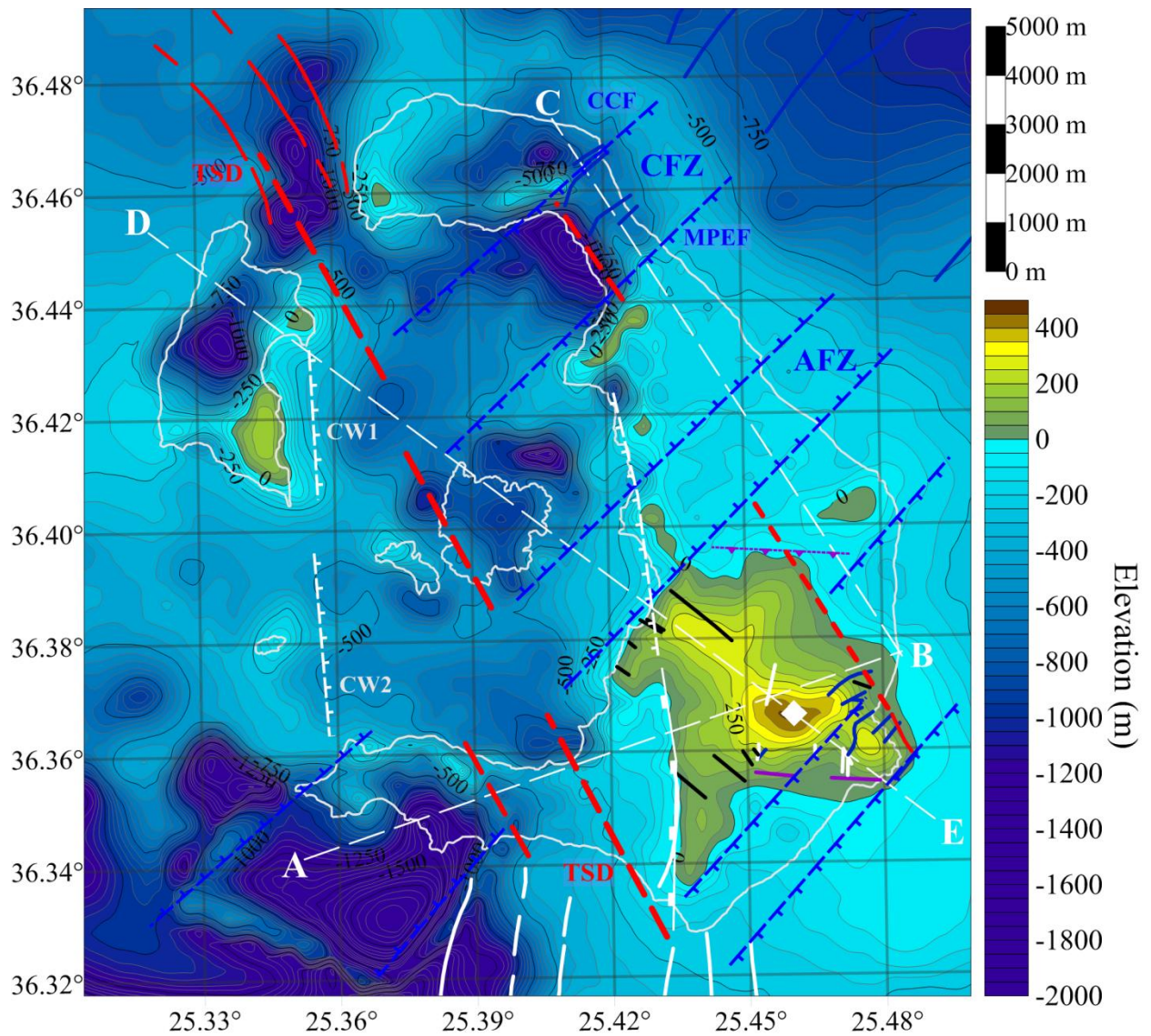


**Figure 5b:** As per Fig. 5a, but for the topography of the *pre-volcanic Alpine basement*.

**FIGURE 6**

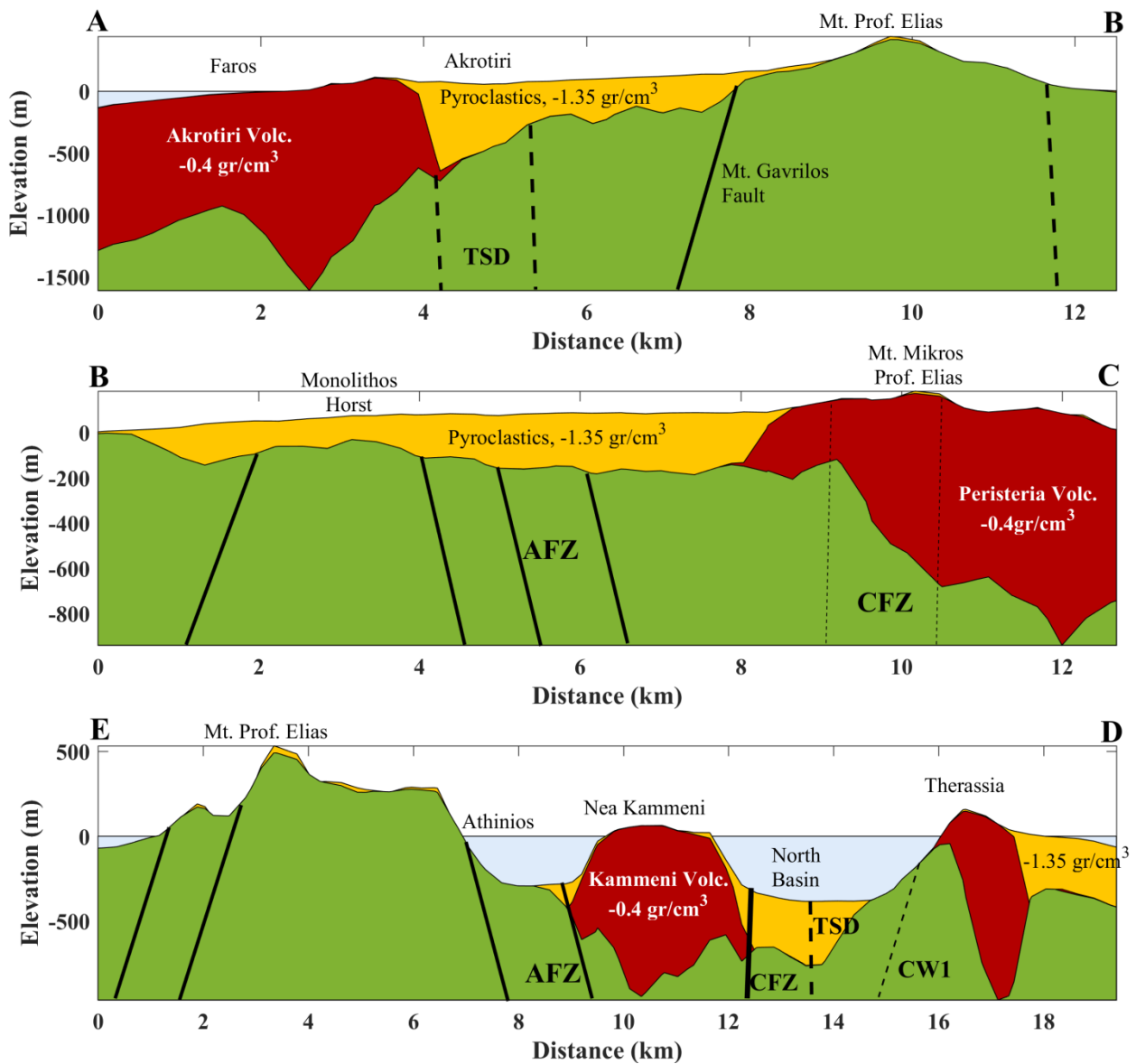


**Figure 6:** Cross-sections indicating the morphology and thickness of the pyroclastic (orange) and volcanic (brick red) rock formations along the profiles AB, BC and ED shown in Fig. 5, as well as the topography of the pre-volcanic Alpine basement (green). The approximate locations of inferred faults and fault zones are indicated with black solid or broken lines. **CFZ:** Columbo Fault Zone; **AFZ:** Anhydros Fault Zone; **TSD:** Trans-Santorin Divide; **CW1** indicates the purported west caldera boundary fault.

**FIGURE 7**

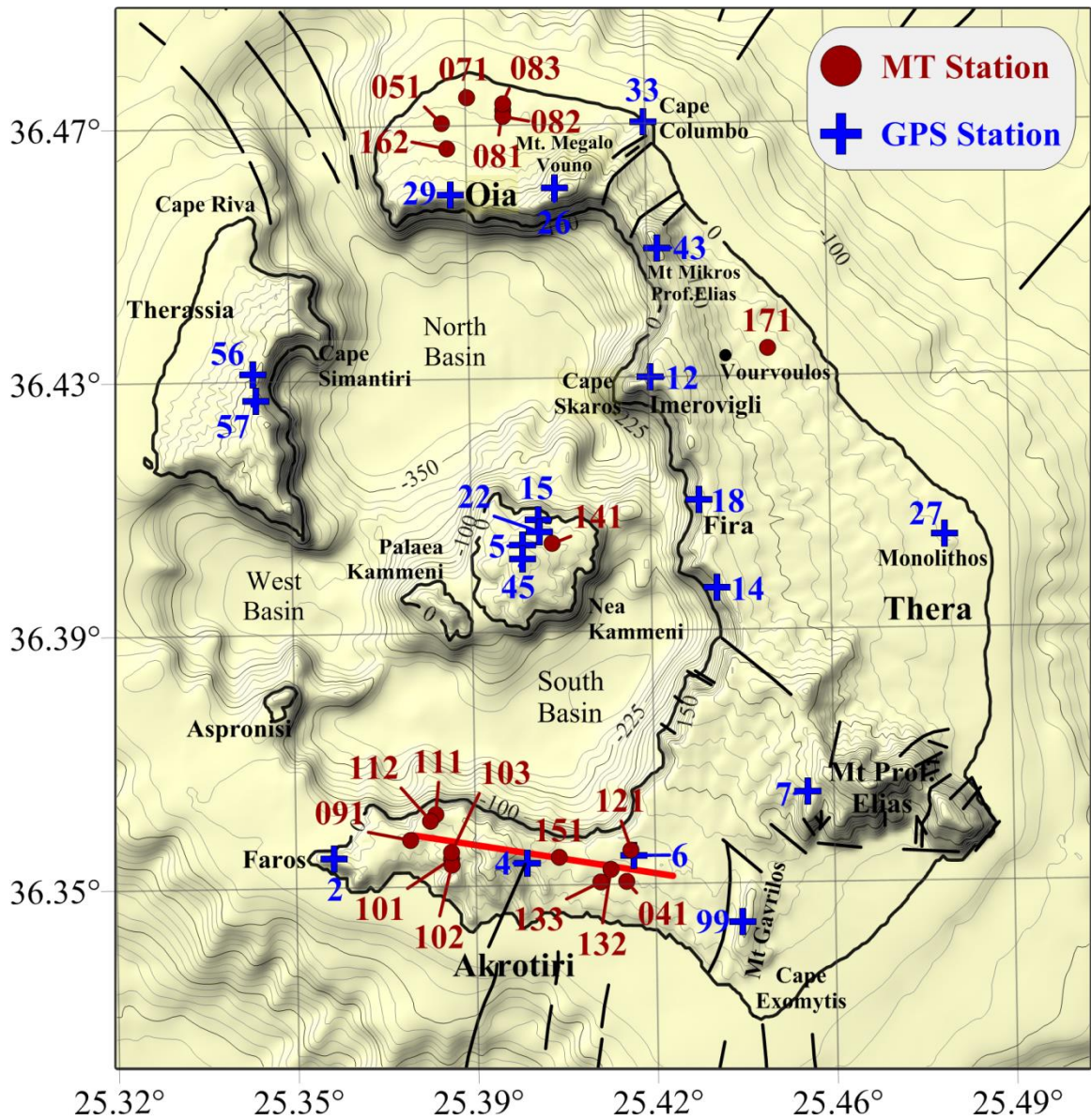


**Figure 7:** Distribution of magnetotelluric sounding sites and DGPS stations. The thick W-E red line at Akrotiri peninsula marks the location of the geoelectric cross section shown in Fig. 10.

**FIGURE 8**

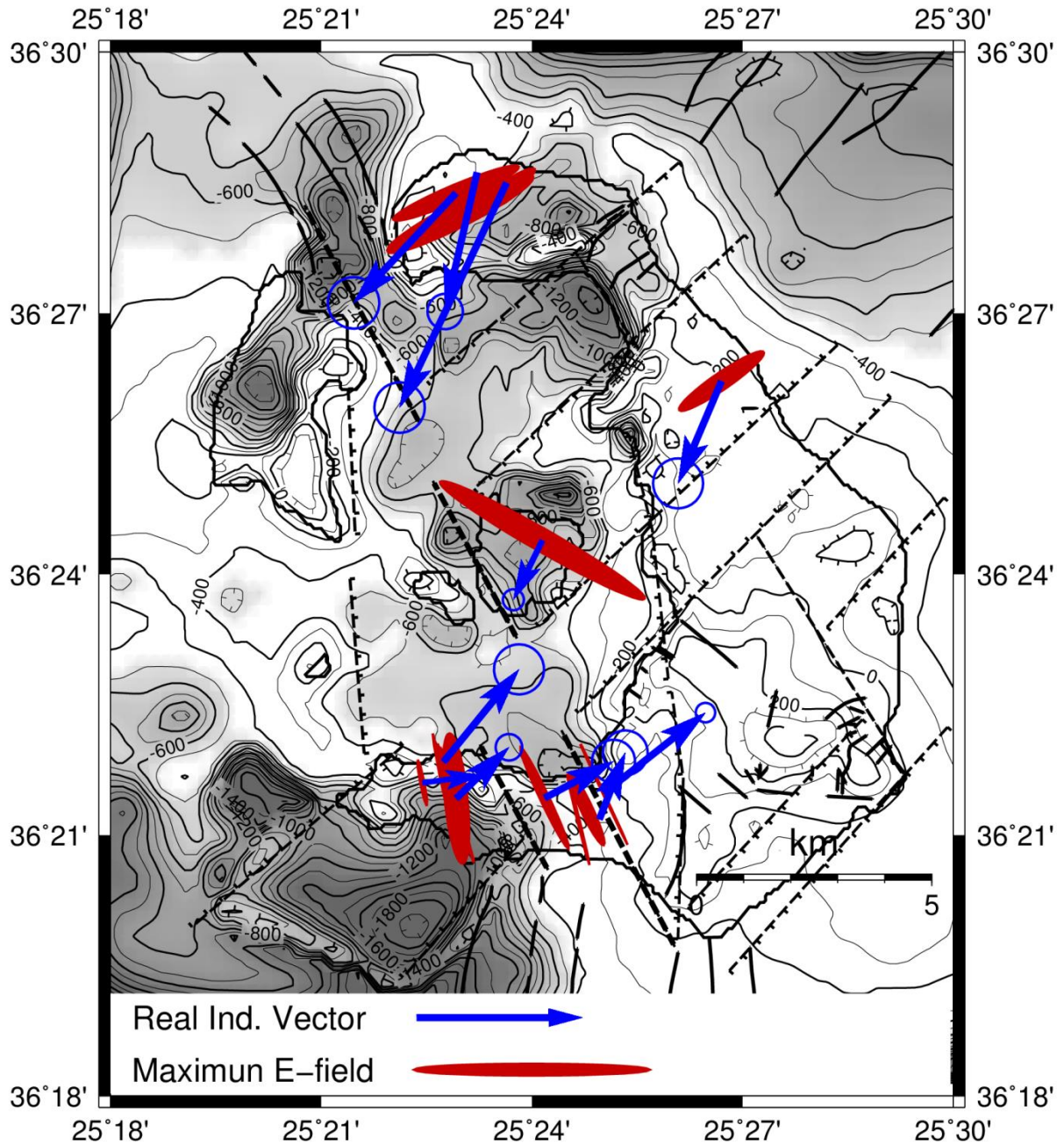


**Figure 8.** Configuration of the polarization state of the maximum electric field (red ellipses) and the Real Induction Vectors (blue arrows); both are shown as averages over the bandwidth 1–100s and are superimposed on the model of the Alpine basement (see Fig. 5b). Solid black lines indicate the traces of mapped (known) faults. Dashed lines mark the traces of inferred faults with throw/dip direction indicated/inferred when possible (see Sections 3 and 5).

**FIGURE 9**

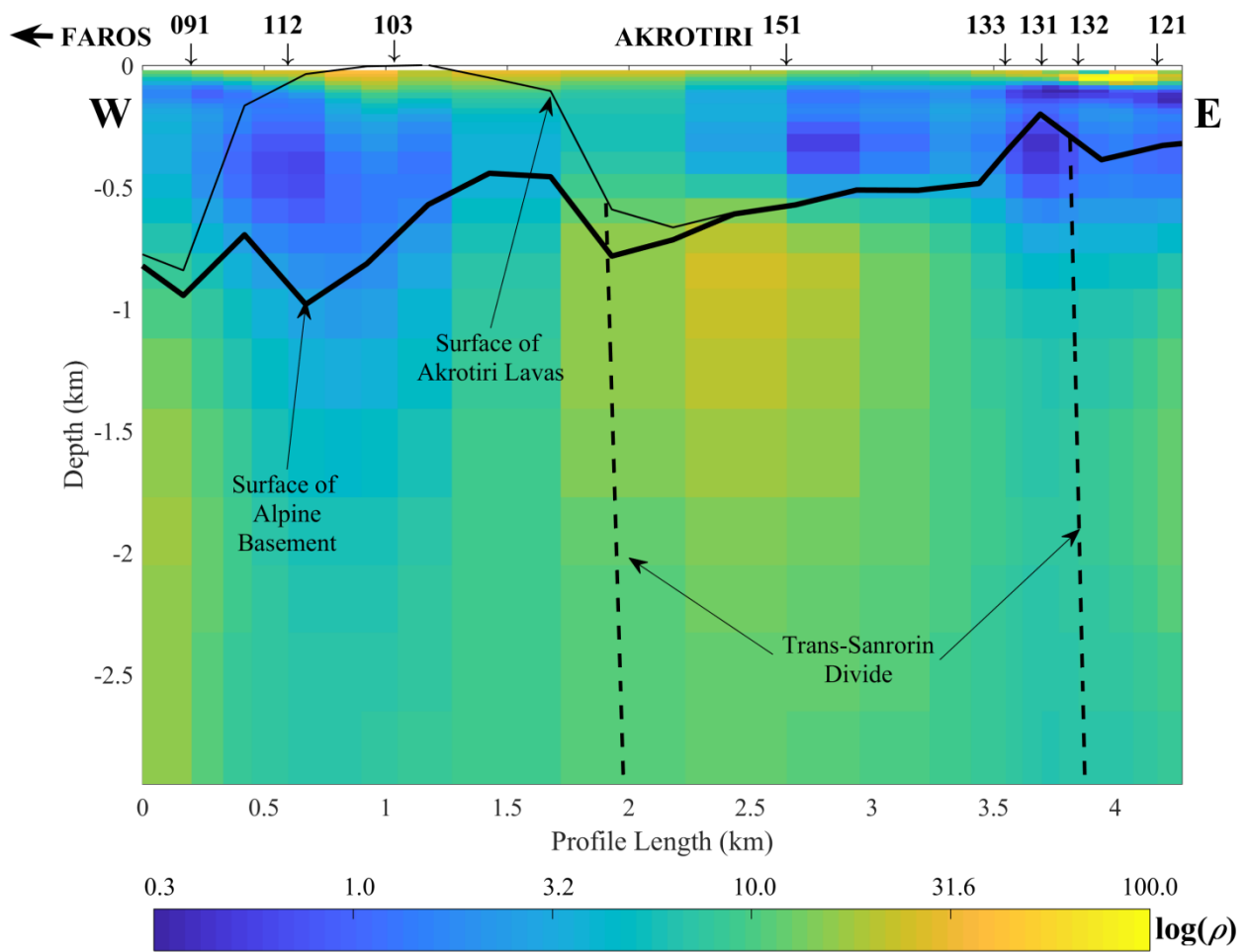


**Figure 9:** West-East geoelectric image of the top three kilometres along the Akrotiri peninsula, obtained with two-dimensional inversion of Magnetotelluric data. Depths refer to the mean sea level.

**FIGURE 10**

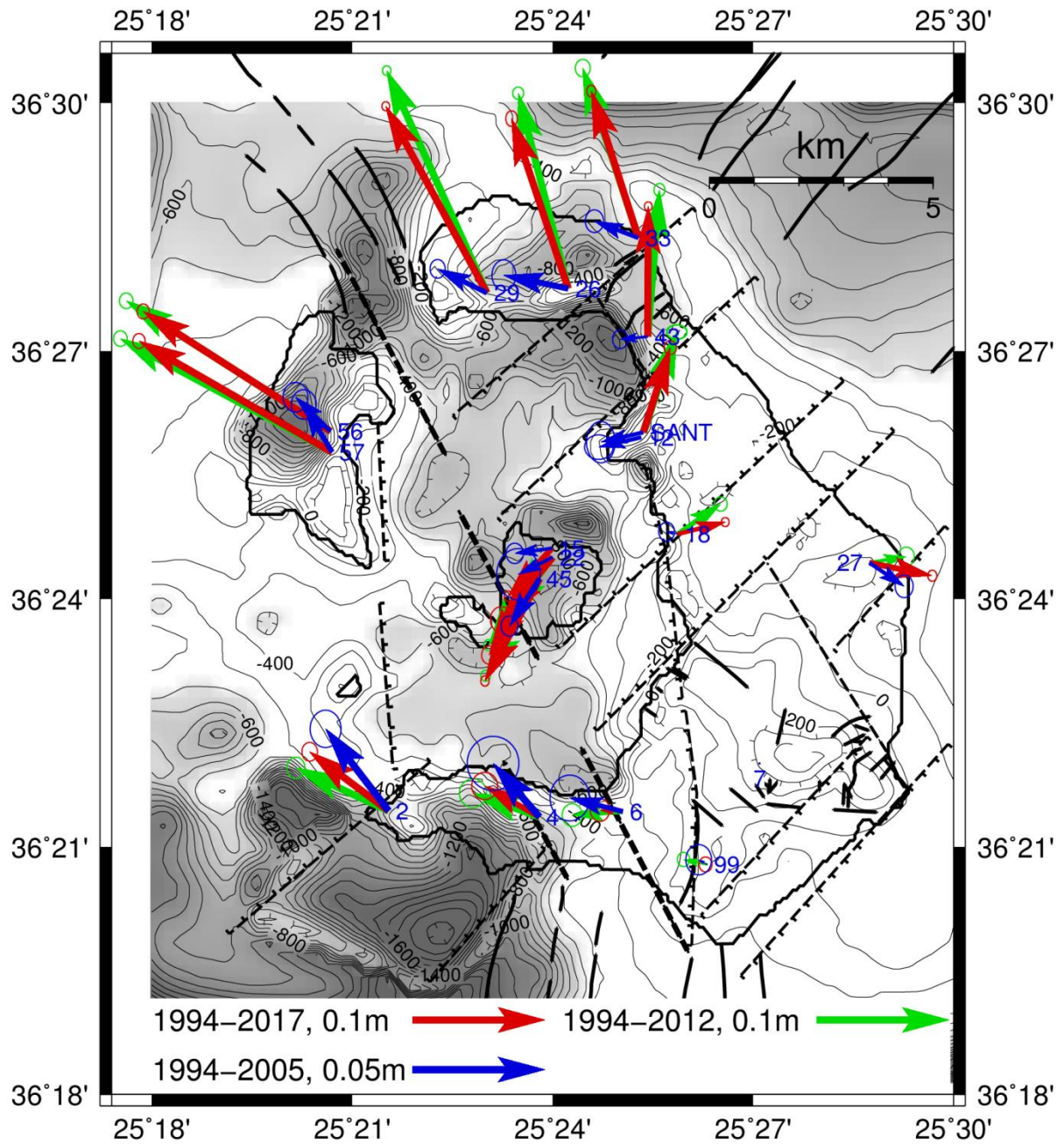


**Figure 10.** The horizontal displacement field relative to Station 7, measured over the periods 1994-2017 (red arrows), 1994-2012 (green arrows) and 1994-2005 (blue arrows). The displacement vectors are superimposed on the model of the surface of the Alpine basement (Fig. 5b). Solid black lines indicate the traces of mapped (known) faults. Dashed lines mark the traces of inferred faults with throw/dip direction indicated/ inferred when possible (see Section 3).

FIGURE 11

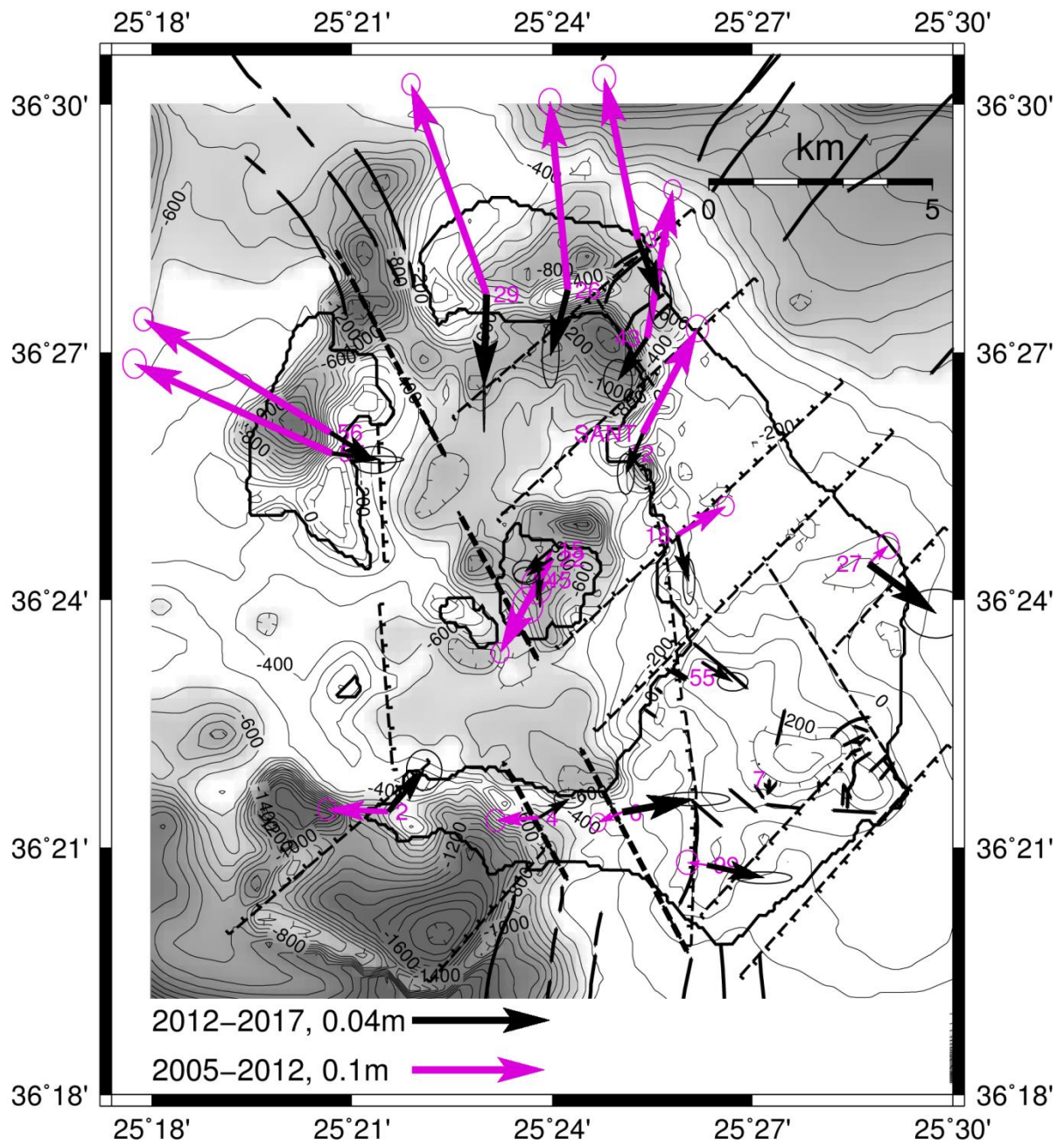
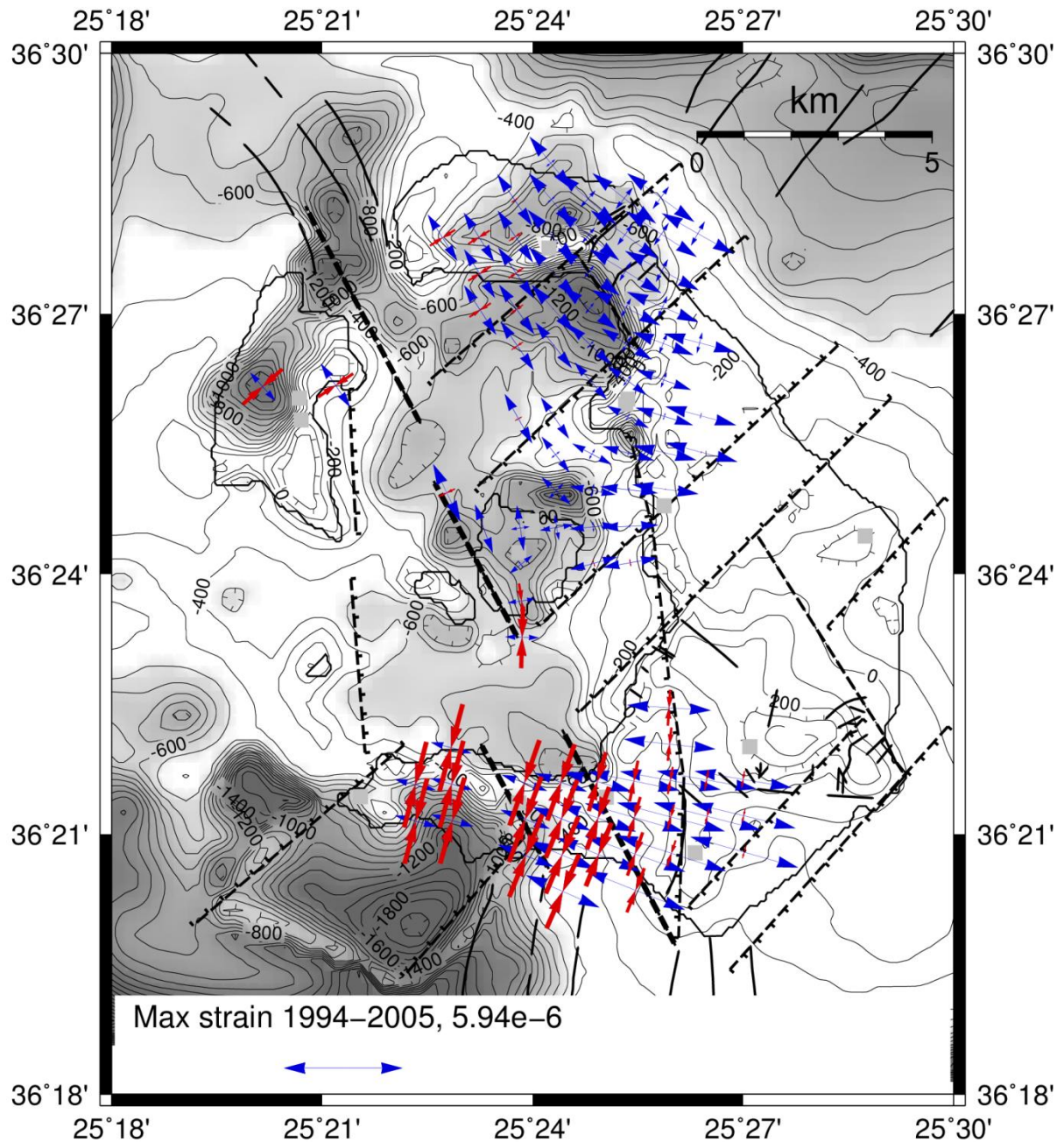


Figure 11: As per Fig. 10 but for periods 2012-2017 (black) and 2005-2012 (magenta arrows)

**FIGURE 12**



**Figure 12:** The horizontal components of the strain tensor in the vicinity of the DGPS stations, determined on the basis of the displacement field during the period 1994-2005. Blue arrows denote extension and red arrows compression. The strain crosses are superimposed on the model of the Alpine basement (see Fig. 5b). Solid black lines indicate the traces of mapped (known) faults. Dashed lines mark the traces of inferred faults with throw/dip direction indicated when possible.

**FIGURE 13**

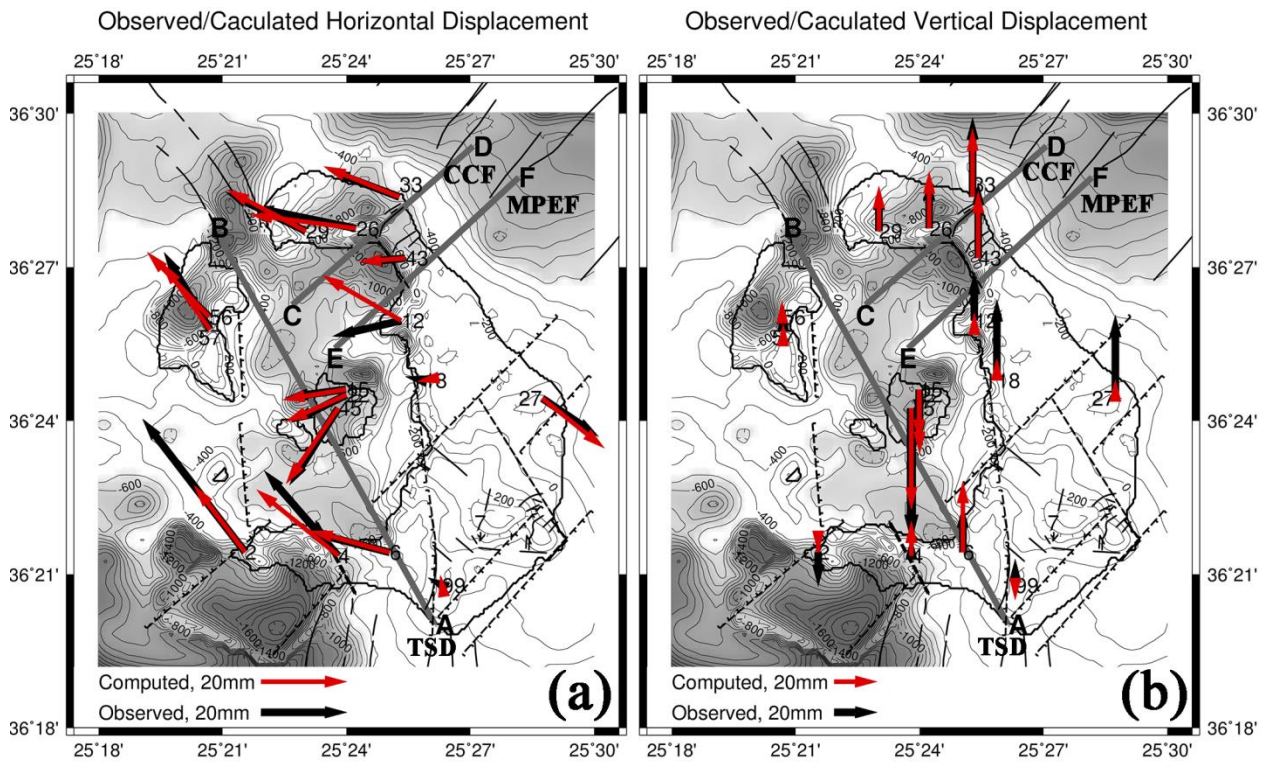


**Figure 13:** Observed (black) and computed (red) displacement vectors for (a) the horizontal and (b) the vertical displacement field over the period 1994-2005 and relative to Station 7. The computed (red) displacement field is due to the combined action of faults AB (TSD), CD (CCF) and EF (MPEF). Displacement vectors are superimposed on the model of the surface of the Alpine basement. Solid black lines indicate the traces of mapped (known) faults. Dashed lines mark the traces of inferred faults with throw/dip direction indicated when possible.

**FIGURE 14**

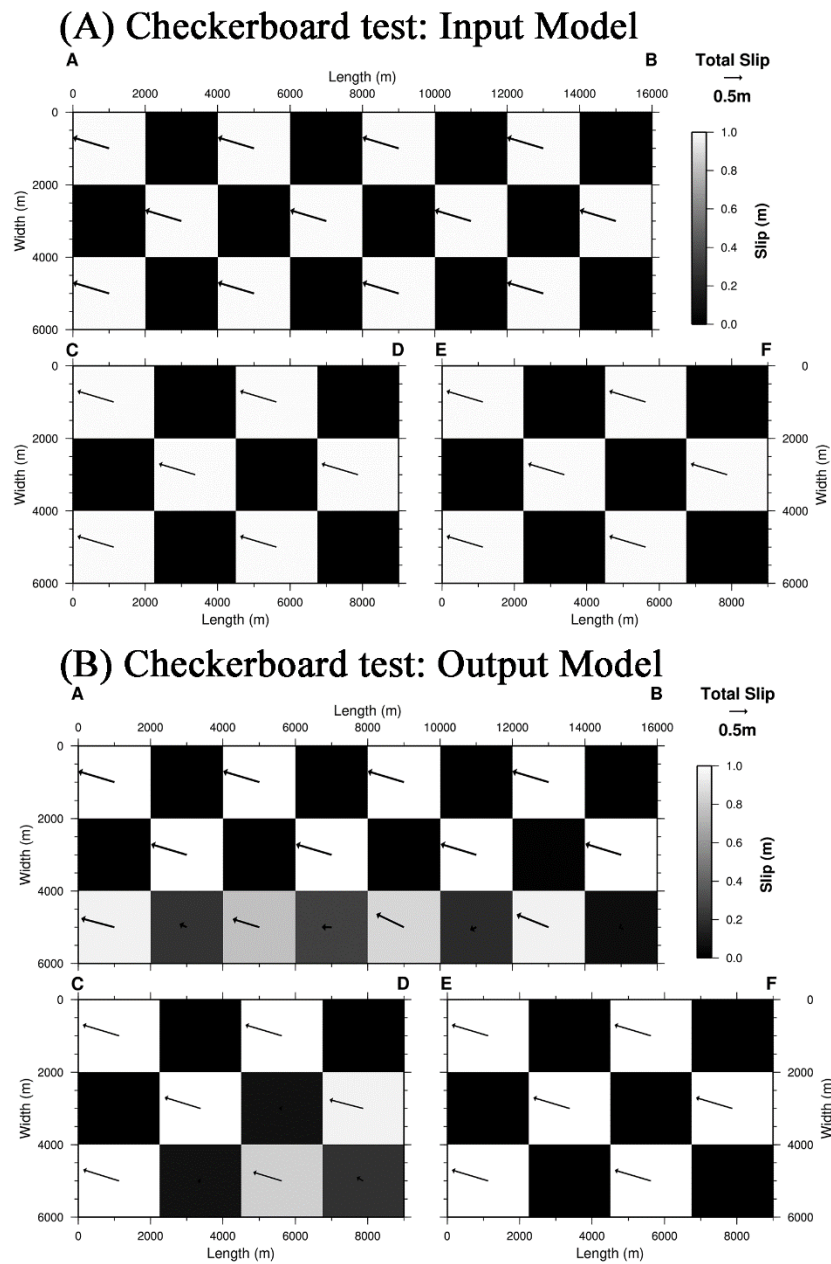


**Figure 14:** Resolution of the fault model shown in Fig. 13. **(a)** The input comprises fault AB discretized into an array a  $2 \times 2$  km tiles and faults CD and EF discretized into arrays of  $2.25 \times 2$  km tiles. Alternating values of zero (black) and one (white) metres of slip were assigned to each tile. **(b)** The output (recovered) slip model obtained with a regularization factor of  $k=1000$ .

**FIGURE 15**

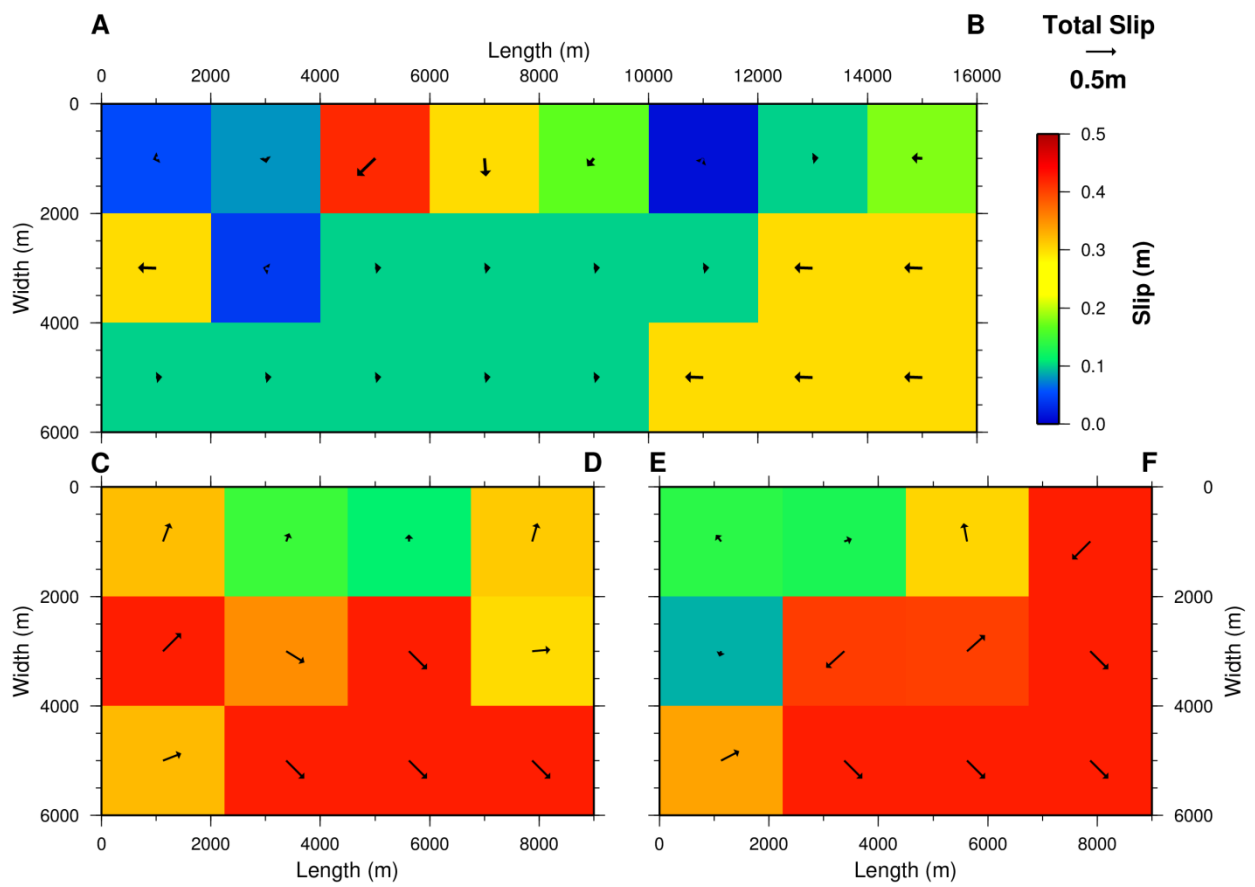


**Figure 15:** The distribution of slip on the fault planes AB (representing the TSD) and CD/EF (representing the CCF) as seen from a vantage point at Fira. All faults are discretized as per Fig. 14.

**FIGURE 16**

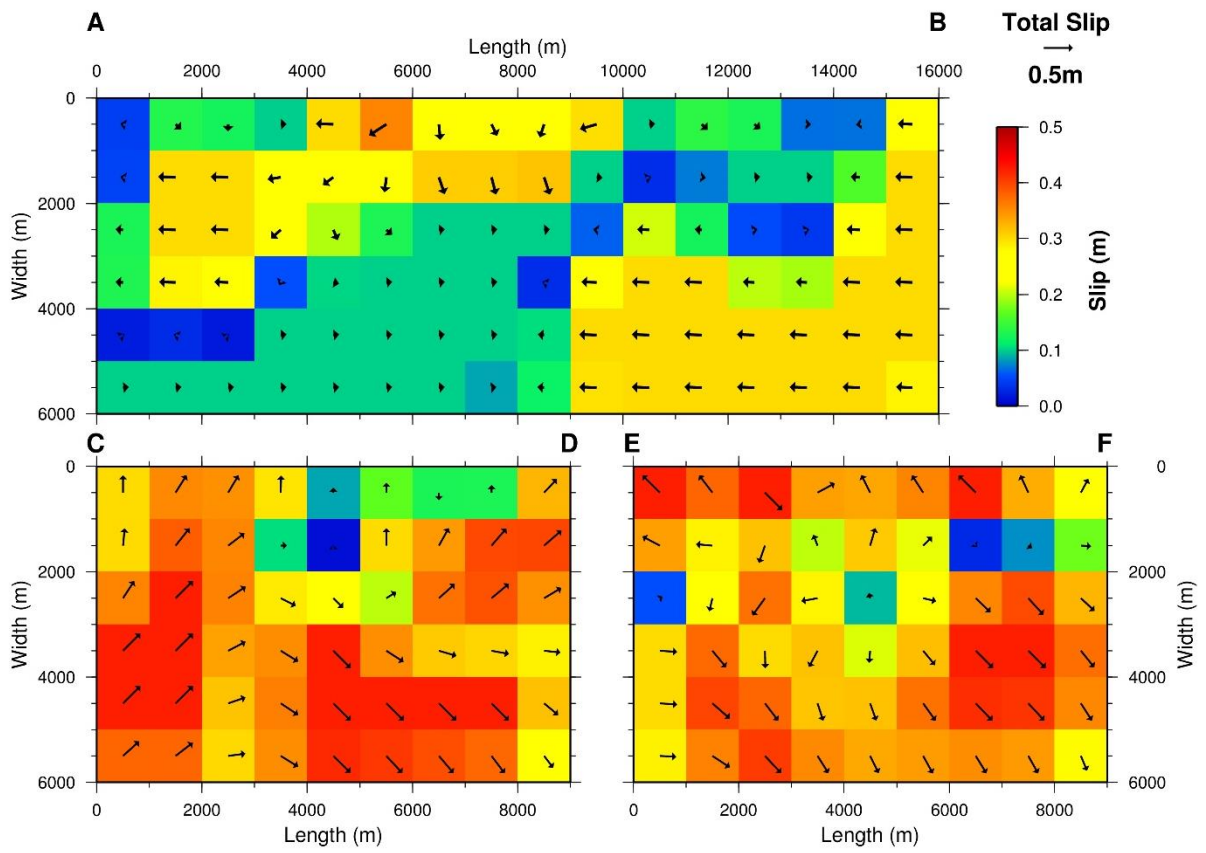


**Figure 16:** As per Fig. 15 but with all faults discretized into arrays of 1×1 km tiles.

**FIGURE 17**

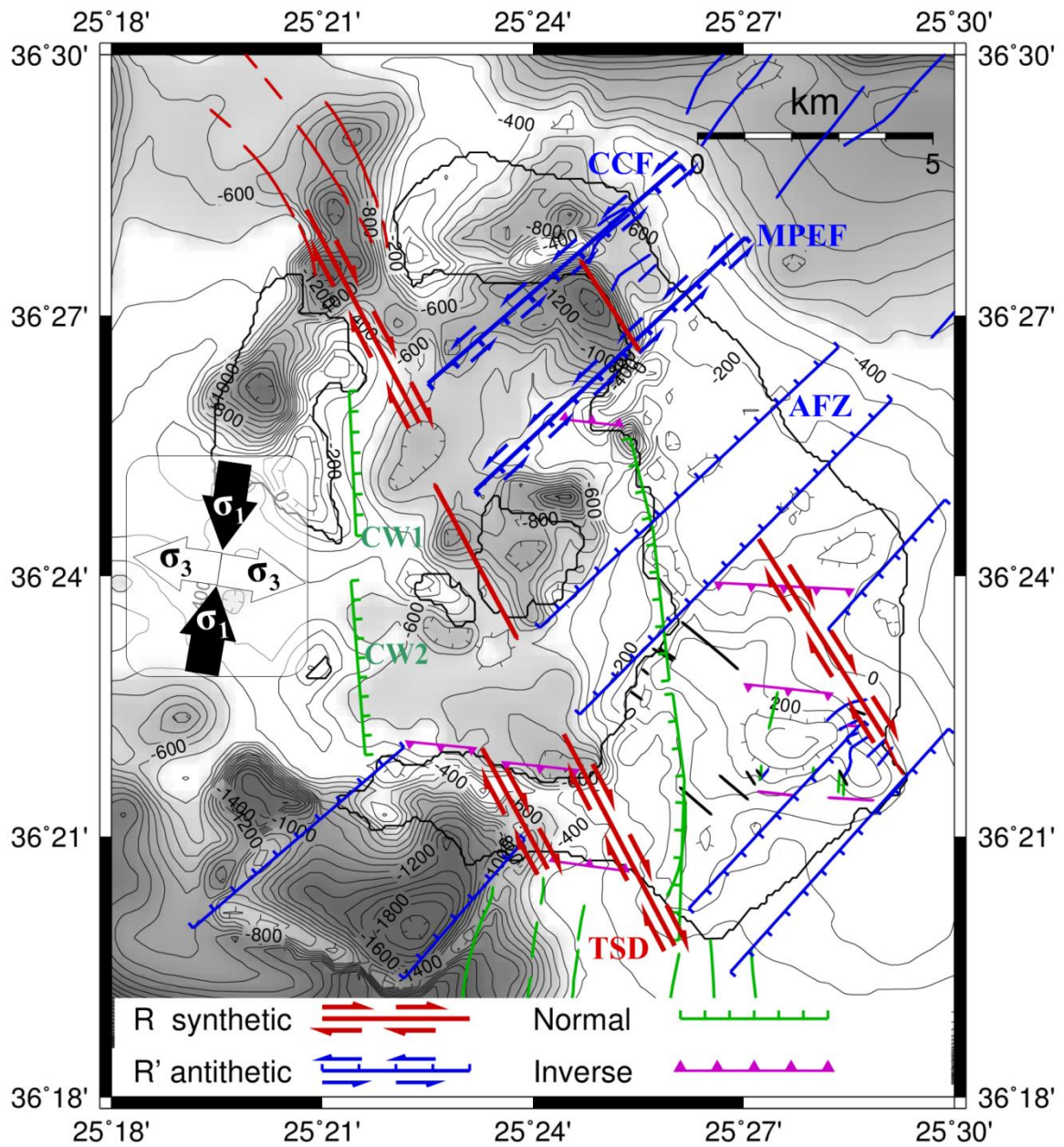


**Figure 17.** The horizontal stress field ( $\sigma_1/\sigma_3$ ), and the principal (R/R') and secondary (normal/inverse) tectonic and kinematic elements of the SVC as determined by the present analysis. They are all superimposed on the model of the surface of the Alpine basement.

# **SUPPLEMENTARY INFORMATION**

## **Tectonic Deformation in the Santorin Volcanic Complex (Greece) as Inferred by Joint Analysis of Gravity, Magnetotelluric and DGPS Observations**

A. Tzanis, S. Chailas, V. Sakkas and E. Lagios

*Section of Geophysics, Department of Geology and Geoenvironment,  
National and Kapodistrian University of Athens,  
Panepistimiopolis, Zografou 157 84, Greece*

**Corresponding Author:** Andreas Tzanis, [atzanis@geol.uoa.gr](mailto:atzanis@geol.uoa.gr)

**Short Title:** Tectonics of Santorini volcano, Greece

Athens, February 2019

# CONTENTS

S1. APPLICABILITY OF GRAVITY AND MAGNETOTELLURIC EXPLORATION METHODS IN THE DETECTION OF TECTONIC ACTIVITY. ....	3
S2. GRAVITY DATA SOURCES AND HOMOGENIZATION PROCEDURE .....	4
S3. RESIDUALS ANALYSIS OF THREE-DIMENSIONAL GRAVITY MODELLING. ....	6
S4. THE MAGNETOTELLURIC – TELLURIC METHOD AND THE INDUCTION VECTORS: BRIEF INTRODUCTION. ....	8
S5. CHARACTERISTIC STATES OF THE MAGNETOTELLURIC IMPEDANCE TENSOR: FORMULATION .....	10
S5.1 Rotation Matrices.....	11
S5.2 Decomposition .....	12
S5.3 The characteristic states of the Impedance Tensor. ....	13
S5.4 Nature of the eigen-fields .....	15
S5.5 Elliptical polarization .....	16
S6. CHARACTERISTIC STATE ANALYSIS AND INDUCTION VECTORS OF A TYPICAL MAGNETOTELLURIC SOUNDING. ....	17
S7. REGIONAL GEOELECTRIC STRIKE BY SIMULTANEOUS ANALYSIS OF THE IMPEDANCE TENSOR ENSEMBLE ...	19
S8. RESIDUALS ANALYSIS OF 2-D MAGNETOTELLURIC MODELLING AT AKROTIRI PENINSULA. ....	21
S9. TYPICAL EXAMPLE OF 1-D INVERSION AT NORTH THERA. ....	22
S10. DGPS MODELLING: MISFIT OBTAINED FOR THE $1 \times 1$ KM DISCRETIZATION SCHEME. ....	23
S11. ADDITIONAL REFERENCES .....	25

## **S1. Applicability of Gravity and Magnetotelluric Exploration Methods in the Detection of Tectonic Activity.**

It is trivial knowledge, that tectonic activity imprints the surface of the earth with discontinuities detectable by direct observation and/or by the analysis of digital elevation models or aerial and satellite images. This approach is severely handicapped in the SVC because most of its surface is covered by layers of pyroclastic formations produced by the Minoan (1645–1500 BCE) and earlier explosive activity, which are easily eliminated by surface processes (weathering and erosion). Nevertheless, markers of tectonic activity should still be preserved in the hard rocks of the pre-volcanic Alpine basement and should be detectable by geophysical prospection methods. The application of seismic methods is not recommended, not only because of high costs, but also because they are ineffective in dispersive pyroclastic formations that abound with voids and small scatterers. Gravity prospection methods have an advantage, both in terms of costs and because of their sensitivity to lateral changes in the distribution of subsurface material densities. In the case of the SVC, the density contrast between the thick but light pyroclastic, heavier volcanic and heavy Alpine basement formations is very significant. Accordingly, given an adequate distribution of observations and appropriate 3-D interpretation tools, it is possible to strip the gravity effect of pyroclastic layers and extrusive volcanic, reconstruct the morphology of the non-pyroclastic basement and map the more significant imprinted effects of tectonic activity (fault steps, graben and horst structures).

The reason why observations of the geoelectric structure can image tectonic processes are traced to the epiphenomenal development of electrical conductivity anomalies in response to faulting. Within the schizosphere, (brittle upper crust), faulting generates permeable rock either directly within the fault zone, (fault gouge, breccia and mylonite), or around it as a result of repeated cycles of loading/ unloading and elasto-plastic deformation (damage). The presence of water in the immediate neighbourhood of the fault zone is very important factor for tectonic processes, as it influences creep and/or stability. Around the fault, tectonically induced (secondary) permeability resulting from micro- and meso-scale fracturing, and crack interconnection is generally aligned with the fault; the more extensive the damage, the higher the conductivity. Healing processes are expected to close cracks and reduce conductivity, unless they are kept open by continuous accumulation of deformation, either seismic or aseismic. Geothermal (hydrothermal) areas and volcanic domains in the upper crust are environments deserving special attention. The electrical conductivity of near surface rocks arises from the fluid content of interconnected pore space (liquid fraction) and depends on the salinity of the pore fluids, the temperature and the presence of clay minerals which may increase the salinity of pore fluids and thus electrical conductivity by several orders of magnitude. The liquid fraction will certainly increase in the neighbourhood of fluid circulation zones, as also will the fraction of clay minerals. In convective geothermal systems, especially those controlled by concurrent tectonic activity, circulation conduits are usually identified with the dominant active fault systems through which fluids are transported from the deep feeder reservoirs or heat sources. This is also true for all geological situations associated with active circulation of subterranean waters.

## S2. Gravity Data Sources and Homogenization Procedure

Several local gravity surveys have been carried out in the Santorin Volcanic Complex during the past four decades, as illustrated in Fig. 3 of the main article. The data set used herein was constructed by assembling, re-evaluating when necessary and homogenizing the data of these surveys, as described below:

- **Yokoyama and Bonasia (1971; 1979)** produced the first coarse gravity anomaly maps of the area based on 50 onshore observations distributed over the entire SVC, and made a preliminary interpretation of the low Bouguer anomaly amplitudes associated with the caldera. Bouguer gravity corrections were performed with a density of  $2.5 \text{ g/cm}^3$  for the 1971 field campaign and  $2.4 \text{ g/cm}^3$  for the 1979 campaign. Terrain corrections were calculated up to a maximum radius of 15km using the standard 1:50,000 scale topographic and 1:150,000 bathymetric maps of the Hellenic Army Geographical Service. Observations were referred to Potsdam Datum through a base station established at the port of Athinios.
- **Budetta et al., (1984)** compiled a considerably more detailed anomaly map based on 208 onshore observations distributed over the entire SVC. Bouguer gravity corrections were effected with a density of  $2.1 \text{ g/cm}^3$  for stations founded on pyroclastic formations and  $2.600 \text{ g/cm}^3$  for stations founded on basement outcrops. Terrain corrections were calculated up to the zone *K* of the Hammer scheme (approx. 10km). Observations were referred to the Potsdam Datum through the base station of Yokoyama and Bonasia. Their analysis concluded that the Bouguer anomaly data comprised a long wavelength component representing the interface between the Alpine basement and the overlying volcanic products, and a short wavelength component representing the positive gravity effect of lava intrusions and the non-submerged part the pre-volcanic Alpine basement.
- **Vasiliadis (1985)** produced a set of 191 stations limited to the southern half of Thera Island. A standard Bouguer density of  $2.67 \text{ g/cm}^3$  was adopted for gravity corrections. There is no specific information about the calculation of terrain corrections. Observations were referred to the Potsdam Datum through a Base Station established in the port of Fira.
- **The University of Athens (UA)** data set is dual: The first set comprises 32 very well constrained and positioned base stations of a micro-gravimetric network established to monitor the Santorin volcano (Lagios et al, 1988; Lagios et al, 1989; Lagios et al, 1995; Chailas and Lagios, 1996). The second set comprises a set of 56 stations measured in an attempt to fill large gaps left by previous surveys at central and northern Thera. Both sets were referred to IGSN71 Datum through a base station established at Monolithos.
- **Offshore data:** A set of gravity observations comprising absolute values of *g* and free-air anomaly data was extracted from the GEODAS data base (NGDC, 2012). Gaps between the GEODAS gravity measurements were filled using the EGM2008 satellite gravity model (Pavlis et al. 2008) computed up to degree 2160.

Owing to its nature, the UA microgravimetric network and relevant data set is by far the most reliable and can thus be used for reference. The network shares the base stations of Fira and Athinios ports (Potsdam Datum) with the other three onshore data sets. Accordingly, it was straightforward to tie these bases with the Monolithos IGSN71 base and by appropriately shifting the respective gravity observations, to refer all data sets to the UA microgravimetric network and the IGSN71 datum. Terrain corrections were (re)calculated up to a radius of 167 km around each gravity station; this was done with an inner disk of

radius 1500m, an inner annulus between 1.5 and 22km and an outer annulus between 22 and 167km. A detailed Digital Elevation Model (DEM) with 20 m grid spacing was used for the inner disk, based on the 1:5000 scale maps of the Hellenic Army Geographical Service and the digitized map of Alexandri et al. (2003). A 50m spacing version of the DEM was used for the inner annulus and a 1km spacing version for the outer annulus. Curvature corrections were included in the computations. The new gravity anomalies were re-calculated using the standard Bouguer density of  $2.67 \text{ g/cm}^3$ .

Using the above homogenisation procedure, the gravity data from the different sources was rendered comparable and compatible for joint analysis. The Bouguer anomaly map is shown in Fig. S1, where the NE-SW oriented depression of Anhydros Basin, amidst which develops the Santorin Volcanic Complex, is clearly observable.

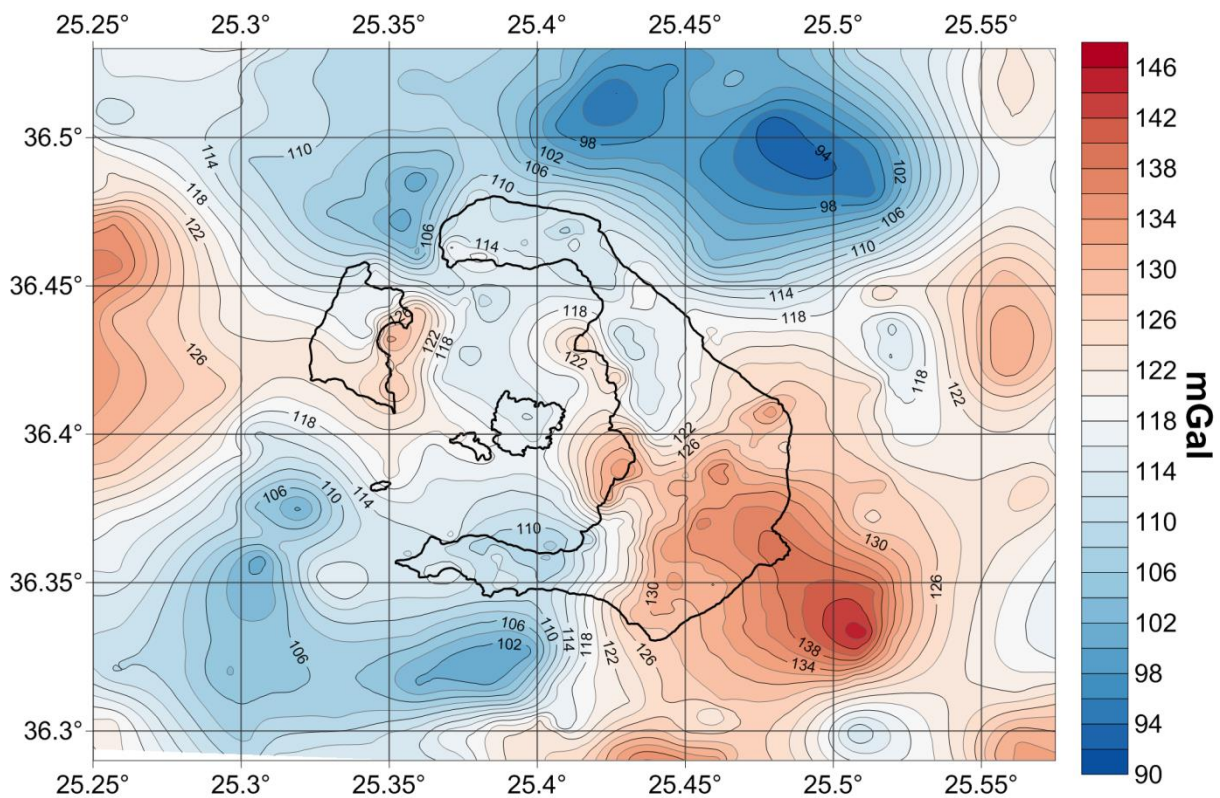


**Figure S1:** Unfiltered Bouguer Gravity Anomaly Map of the Santorin Volcanic Complex.

In a final step, an elliptical 2-D high pass filter was applied in order to isolate the gravity “signal” of the SVC; this filter had a major axis azimuth of  $020^\circ$  and ramps between 70-75km along the major axis and 25-20km along the minor. The filtered Bouguer anomaly map is shown in Fig. 4 and discussed in Section 2 of the main article.

### S3. Residuals Analysis of Three-Dimensional Gravity Modelling.

The modelling procedure described in Section 3.2 of the main article was rather successful, with the second stage analysis yielding a final RMS error of 0.65 mGal, a fractional error of only 5.1% and goodness of fit  $R^2 = 0.96$ . The quality of the model can be studied in Fig. S2. As evident in Fig. S2a, significant residuals can be observed only in the perimeter of major volcanic formations at Akrotiri, Therassia and north Thera (Peristeria volcano). Fig. S2b shows an analysis of the distribution of the residuals returned by the second stage analysis. Only 20.5% of the residuals are larger than  $\pm 0.5$ mGal and only 6.5% are larger than  $\pm 1$ mGal. There are no outliers in the formal sense of the term and it is clear that the residuals follow a mixture of *two* normal distributions: one with  $\mu=0.025$ mGal and  $\sigma=0.097$ mGal comprising approximately 43.6% of the total population (blue line), and one with  $\mu=0.245$ mGal,  $\sigma=0.489$ mGal comprising approximately 56.4% (red line), which can also be seen to associate with an overabundance of residuals with amplitudes greater than  $\pm 1$ mGal.

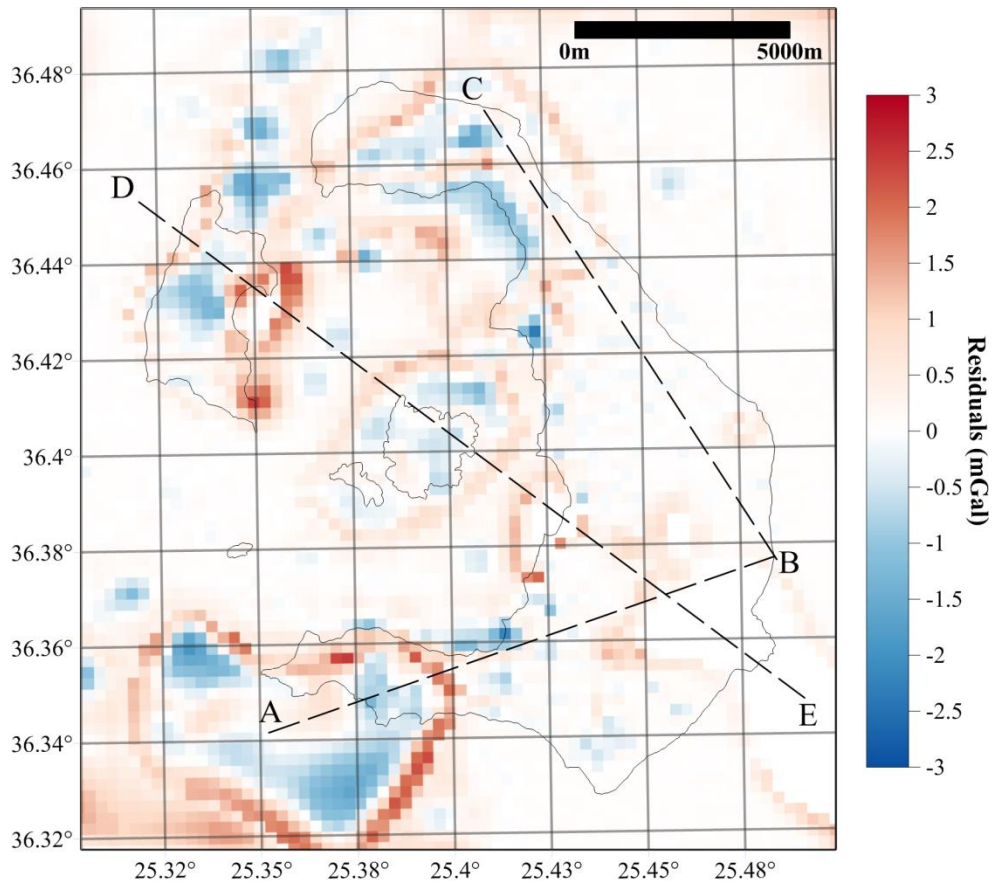


**Figure S2a.** Distribution of Bouguer anomaly residuals after stripping the gravity effect of the pyroclastic overburden and volcanic formations (see main article for details). The dashed lines indicate the locations of profiles AB, BC and DE shown in Fig. 6 of the main article.

Comparative study of Fig. S2a and S2b will show that the former (narrow) distribution emerges from areas in which the topography of the “Alpine basement” and the thickness  $Z_U^{(2)} - Z_L^{(2)}$  was *fixed* (south and central Thera, South and West Basin). Conversely, the latter (broader) distribution emerges from areas in which the thickness  $Z_U^{(2)} - Z_L^{(2)}$  was allowed to vary; it can thus be attributed to the stripping of

the volcanic formations and is rather easy to understand. To begin with, the density of volcanic formations may actually vary between volcanic centres, albeit not by large. However, it is also apparent that the larger residuals appear at locations at which the observed Bouguer anomaly exhibits high gradients *and* is inadequately constrained (offshore to the south of Akrotiri peninsula, offshore to the NE of north Thera, in the South Basin etc.). An additional cause may be the discretization of the model (200m grid spacing) with respect to the steepness of local terrain and/or Bouguer anomaly gradients, especially along the rim of the caldera and at places where anomaly gradients are inadequately constrained. Although these issues have small overall effect on the quality of the model, they are useful to bear in mind during interpretation. In a final comment, we note that due to the relative paucity of data, the resolution of surfaces  $\mathbf{Z}_L^{(1)}$  and  $\mathbf{Z}_L^{(2)}$  is marginal in the North Basin, but our relatively coarse discretization scheme, still allows interpretation. Conversely,  $\mathbf{Z}_L^{(1)}$  and  $\mathbf{Z}_L^{(2)}$  are *not* constrained in the West and South Basin and the topography of the basement is not easy to interpret with confidence.

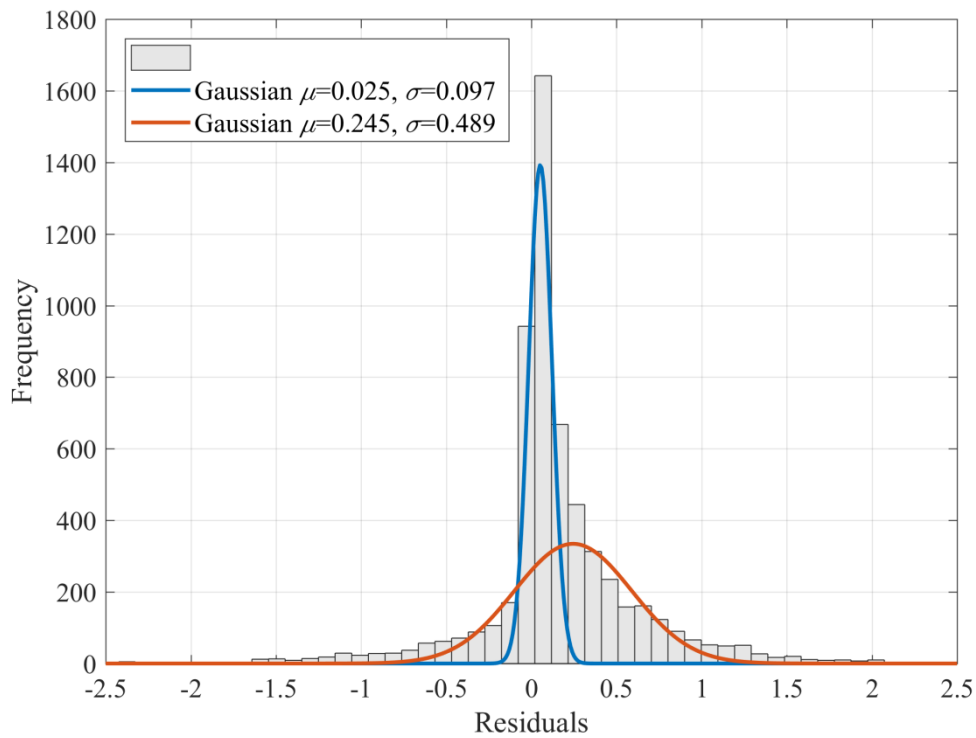


**Figure S2b.** Analysis of the statistical distribution of the residuals shown in Fig. S2a.

#### S4. The Magnetotelluric – Telluric Method and the Induction Vectors: Brief Introduction.

The Magnetotelluric (MT) survey was conducted during the summer of 1993 and comprised a total of 37 soundings (Sotiropoulos et al, 1996a,b). Measurements were carried out in the nominal frequency bandwidth 128Hz-100s using Pb/PbCl<sub>2</sub> electrodes and CM11E induction coils with the Short Period Automatic Magnetotelluric system (SPAM) Mk III developed in the University of Edinburgh by G.J.K Dawes (Ritter et al., 1998). Shortage of induction coils and the capacity of SPAM MkIII to measure data in multiple simultaneous stations compelled the application of the Magnetotelluric–Telluric (MT-T) measurement mode by using a 5-component Magnetotelluric configuration at a “*base*” site and 2-component telluric configuration at multiple nearby “*satellite*” (remote) sites. In the work reported herein, the MT-T clusters of soundings were numbered sequentially starting with 01; the base station was always denoted by a suffix 1 and the satellite stations by 2, 3, etc. Thus, site code 151 means base station 15, site code 133 means the 3<sup>rd</sup> satellite of base station 13 etc. (see Fig. 7 of main article).

The MT-T method demands uniformity of the source field over the base and satellite stations, which is prerequisite for Magnetotelluric sounding (Leontovich boundary condition) and is perfectly satisfied across distances of sub-kilometric to kilometric scale. At the base station (indicated by the subscript  $B$ ) one measures the horizontal (transverse) components of the total magnetotelluric field

$$\mathbf{E}_B = \begin{bmatrix} E_{xB} \\ E_{yB} \end{bmatrix} \quad \text{and} \quad \mathbf{H}_B = \begin{bmatrix} H_{xB} \\ H_{yB} \end{bmatrix}$$

whence the impedance tensor  $\mathbf{Z}_B$  can be computed. At the remote stations (indicated by the subscript  $R$ ), only the telluric field components are measured:

$$\mathbf{E}_R = \begin{bmatrix} E_{xR} \\ E_{yR} \end{bmatrix}.$$

The remote telluric field can be mapped onto the base telluric field by the *telluric transfer tensor*  $\mathbf{T}$ :

$$\begin{pmatrix} E_{xR} \\ E_{yR} \end{pmatrix} = \begin{pmatrix} T_{xx} & T_{xy} \\ T_{yx} & T_{yy} \end{pmatrix} \cdot \begin{pmatrix} E_{xB} \\ E_{yB} \end{pmatrix} \rightarrow \mathbf{E}_R = \mathbf{T} \cdot \mathbf{E}_B.$$

At the base station, the magnetic field is mapped onto the electric field by the *impedance tensor*  $\mathbf{Z}_B$  as

$$\begin{pmatrix} E_{xB} \\ E_{yB} \end{pmatrix} = \begin{pmatrix} Z_{xx} & Z_{xy} \\ Z_{yx} & Z_{yy} \end{pmatrix} \cdot \begin{pmatrix} H_{xB} \\ H_{yB} \end{pmatrix} \rightarrow \mathbf{E}_B = \mathbf{Z}_B \cdot \mathbf{H}_B$$

It follows that

$$\mathbf{E}_R = \mathbf{T} \cdot \mathbf{E}_B \Leftrightarrow \mathbf{E}_R = \mathbf{T} \cdot \mathbf{Z}_B \cdot \mathbf{H}_B \Leftrightarrow \mathbf{E}_R = \mathbf{Z}_M \cdot \mathbf{H}_B$$

where  $\mathbf{Z}_M$  is the *impedance transfer tensor* by which the *uniform* magnetic field  $\mathbf{H}_B$  measured at the base, is mapped onto the remote telluric field  $\mathbf{E}_R$ . The impedance transfer tensor can be estimated directly from the base magnetic and remote telluric fields.

The vertical component of the magnetic field is generated within the Earth by currents induced on the surfaces of lateral conductivity interfaces; it is therefore vital in providing information about the location and geometry of lateral interfaces. The Magnetic Transfer Function (MTF) comprises a rank 1 tensor that maps the horizontal (inducing) components of the total magnetic field onto the vertical (induced) component according to

$$H_z(\omega) = \mathbf{X}(\omega) \cdot \mathbf{H}(\omega) \quad \rightarrow \quad H_z(\omega) = X_{zx}(\omega) \cdot H_x(\omega) + X_{zy}(\omega) \cdot H_y(\omega).$$

Herein, the information conveyed by the MTF will be used in its Induction Vector (IV) form. An Induction Vector comprises a magnitude and an azimuth that defines the normal to the local strike of the anomalous concentration of current generating the anomalous vertical magnetic field. Two such vectors are defined for vertical fields responding in-phase (*real*) and out-phase (*imaginary*) with the horizontal component with which the vertical field exhibits maximum correlation. If  $\vec{\mathbf{x}}$  and  $\vec{\mathbf{y}}$  are unit vectors parallel to the  $x$  and  $y$  axes of the experimental coordinate frame, their respective definitions are:

$$\text{Real Induction Vector} \quad : \quad \mathbf{V}_R(\omega) = \Re\{X_{zx}(\omega)\} \cdot \vec{\mathbf{x}} + \Re\{X_{zy}(\omega)\} \cdot \vec{\mathbf{y}},$$

$$\text{Imaginary Induction Vector} \quad : \quad \mathbf{V}_I(\omega) = \Im\{X_{zx}(\omega)\} \cdot \vec{\mathbf{x}} + \Im\{X_{zy}(\omega)\} \cdot \vec{\mathbf{y}}.$$

For two-dimensional conductivity interfaces in which the vertical magnetic field is exclusively associated with induction in the Transverse Electric mode, the dot products ensure that  $\mathbf{V}_R$  and  $\mathbf{V}_I$  are mutually parallel or anti-parallel and always perpendicular to the strike of the interface (e.g. Rokityansky, 1982). For three-dimensional conductivity structures  $\mathbf{V}_R$  and  $\mathbf{V}_I$  can no longer be parallelism/ anti-parallel and their direction defines the normal to the local concentration of current that produces the anomalous magnetic field.

## S5. Characteristic States of the Magnetotelluric Impedance Tensor: Formulation

Details can be found in Tzanis (2014) and only a brief expose is given herein, so as to provide the interested reader with fairly complete information. To begin with, we are concerned with the (anti)diagonalization of the impedance tensor via rotation (coordinate system transformation). It is therefore imperative to clarify the geometry of the coordinate system(s) in which the impedance tensor is defined. Owing to the orthogonality of the electric and magnetic fields, the impedance tensor may be defined in one of two *right-handed* coordinate systems (Fig. S3).

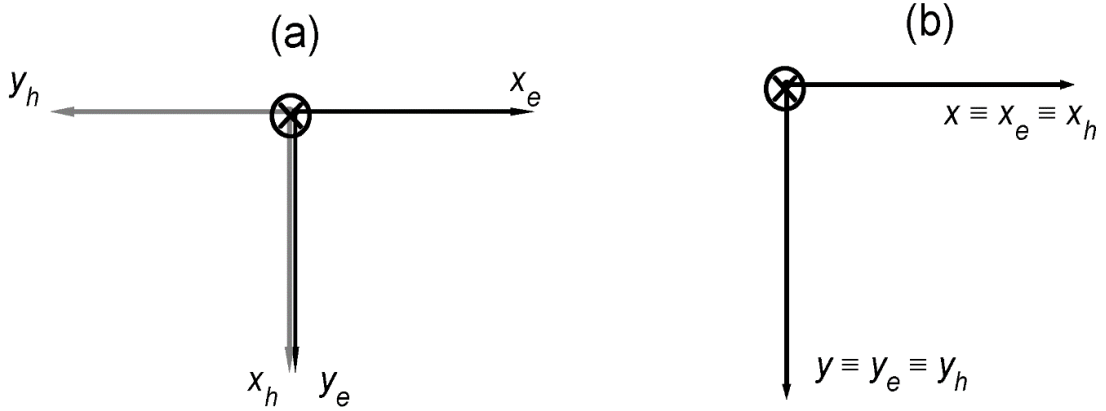


**Figure S3:** Two coordinate systems suitable for referencing the MT impedance tensor. **(a)** *Coordinate system 1:* the input magnetic and output electric fields are referenced to the transverse Cartesian coordinate frames  $(x_h, y_h)$  and  $(x_e, y_e)$  respectively. **(b)** *Coordinate System 2:* the input magnetic and output electric fields are referenced to the same Cartesian coordinate frame  $(x_h, y_h) \equiv (x_e, y_e) \equiv (x, y)$ .

- In *Coordinate System 1* (CS-1), the horizontal axes of the magnetic (input) coordinate frame  $(x_h, y_h)$  are rotated by  $90^\circ$  clockwise with respect to the horizontal axes of the electric (output) reference frame  $(x_e, y_e)$  according to

$$\begin{bmatrix} x_h \\ y_h \end{bmatrix} = \begin{bmatrix} 0 & -1 \\ 1 & 0 \end{bmatrix} \begin{bmatrix} x_e \\ y_e \end{bmatrix} = \mathbf{R}\left(\frac{\pi}{2}\right) \begin{bmatrix} x_e \\ y_e \end{bmatrix}$$

so that the  $x_h$ -axis is parallel to the  $y_e$ -axis and the  $y_h$ -axis anti-parallel to the  $x_e$ -axis (Fig. S3a). In this system, the relationship (mapping) between the transverse components of the magnetic input and electric output fields is

$$\begin{bmatrix} E_{x_e}(\omega) \\ E_{y_e}(\omega) \end{bmatrix} = \begin{bmatrix} Z_{x_e x_h}(\omega) & Z_{x_e y_h}(\omega) \\ Z_{y_e x_h}(\omega) & Z_{y_e y_h}(\omega) \end{bmatrix} \begin{bmatrix} H_{x_h}(\omega) \\ H_{y_h}(\omega) \end{bmatrix} \leftrightarrow \mathbf{E}(\omega) = \mathbf{Z}(\omega) \mathbf{H}(\omega)$$

and is apparently *symmetric*. CS-1 is seldom (if at all) used in Magnetotelluric practice but has been implemented in fundamental theoretical work because the symmetric input – output mapping facilitates the direct application of physical and mathematical concepts known from the analysis of symmetric physical systems, to the Magnetotelluric problem: it is the coordinate system used by Yee and Paulson (1987) and implicitly by LaTorraca et al. (1986).

- In the *Coordinate System 2* (CS-2), the input magnetic and output electric frames are identical, so that  $x_h \equiv x_e \equiv x$  and  $y_h \equiv y_e \equiv y$  (Fig. S3b). The transverse magnetic input and electric output field components are associated with the familiar relationship

$$\begin{bmatrix} E_x(\omega) \\ E_y(\omega) \end{bmatrix} = \begin{bmatrix} Z_{xx}(\omega) & Z_{xy}(\omega) \\ Z_{yx}(\omega) & Z_{yy}(\omega) \end{bmatrix} \begin{bmatrix} H_x(\omega) \\ H_y(\omega) \end{bmatrix} \leftrightarrow \mathbf{E}(\omega) = \mathbf{Z}(\omega)\mathbf{H}(\omega)$$

which is apparently *anti-symmetric*. CS-2 is the system commonly used in Magnetotelluric practice. The impedance tensors  $\mathbf{Z}(\omega)$  and  $\mathbf{Z}(\omega)$  are related as

$$\mathbf{Z}(\omega) = \mathbf{Z}(\omega)\mathbf{R}\left(\frac{\pi}{2}\right) \quad (1)$$

### S5.1 Rotation Matrices

The group SU(2) is a continuous, compact subset of the U(n) Lie group of  $n \times n$  unitary matrices with  $n^2-1$  independent parameters (for details see Arfken and Weber, 2005; Normand, 1980; Wigner, 1959) and Rose, 1957). The condition  $\det\{U(n)\}=+1$  imposes rotations only and defines the Special Unitary (Unimodular) group SU(n). For  $n=2$  there exist three independent parameters that amount to rotation angles. Our familiar three-dimensional space (3-space) is defined over the real field  $\mathbb{R}^3$ . Rotations in  $\mathbb{R}^3$  are specified by representations of the Special Orthogonal Lie group SO(3) of  $3 \times 3$  real valued unimodular matrices. It can be shown that from any Cartesian tensor in  $\mathbb{R}^3$ , one can define a mapping onto the set of  $2 \times 2$  complex matrices in the Hilbert space of complex valued  $L^2$  (squared) functions on  $\mathbb{R}^3$ , which for the purpose of spin (rotation) analysis *only*, reduces to  $\mathbb{C}^2$ ; this mapping we can visualize in the simple zero-trace Hermitian form

$$\mathbf{P}(x, y, z) = \mathbf{s}_1 x + \mathbf{s}_2 y + \mathbf{s}_3 z = \begin{vmatrix} \mathbf{z} & \mathbf{x} + i\mathbf{y} \\ \mathbf{x} - i\mathbf{y} & -\mathbf{z} \end{vmatrix}$$

with  $\det\{\mathbf{P}\} = \mathbf{x}^2 + \mathbf{y}^2 + \mathbf{z}^2 = 1$ . SU(2) enters as a symmetry group in  $\mathbb{C}^2$ . For any unimodular matrix  $\mathbf{U} \in \text{SU}(2)$ , an arbitrary unitary transformation  $\mathbf{P} \rightarrow \mathbf{Q} = \mathbf{U} \cdot \mathbf{P} \cdot \mathbf{U}^\dagger$  is also traceless Hermitian and since  $\det \mathbf{Q} = \det \mathbf{P}$ , the real linear transformation  $\{x, y, z\} \rightarrow \{x', y', z'\}$  induced by  $\mathbf{P} \rightarrow \mathbf{Q} = \mathbf{P}(x', y', z')$  is such that  $\mathbf{x}^2 + \mathbf{y}^2 + \mathbf{z}^2 = \mathbf{x}'^2 + \mathbf{y}'^2 + \mathbf{z}'^2$ . In other words, the unitary transformation  $\mathbf{P} \rightarrow \mathbf{Q}$  comprises a representation of group SO(3) by  $2 \times 2$  unitary matrices. However, SO(3) and SU(2) are only *locally* isomorphic meaning that as long as small rotations are considered, one cannot tell the difference. However, a rotation of  $360^\circ$  corresponds to an element of SU(2) that is not identity so that rotations are unique to within a symmetry of  $2\pi$ . Thus, SU(2) is the *universal covering space* of SO(3), with covering map  $2 \rightarrow 1$  (a double cover) and the topology of the 3-sphere  $S^3$  (i.e. four dimensional).

In a right-handed coordinate frame with  $x$ -top (North),  $y$ -right (East) and  $z$ -down (e.g. CS-2), it is easy to show that a clockwise rotation about the  $z$ -axis is performed by the operator

$$\mathbf{U}_z = \begin{bmatrix} \cos \varphi & -\sin \varphi \\ \sin \varphi & \cos \varphi \end{bmatrix} \in \text{SO}(2) \subset \text{SU}(2)$$

and a clockwise rotation about the  $x$ -axis by

$$\mathbf{U}_x = \exp\left(i \frac{\vartheta}{2} \mathbf{s}_1\right) \approx \begin{bmatrix} \cos \frac{\vartheta}{2} & i \sin \frac{\vartheta}{2} \\ i \sin \frac{\vartheta}{2} & \cos \frac{\vartheta}{2} \end{bmatrix}.$$

Thus, letting  $\theta = \vartheta/2$ , a clockwise rotation about the  $z$ -axis, followed by a clockwise rotation about the  $x$ -

axis is performed by

$$\mathbf{U}_{zx}(\varphi, \vartheta) = \mathbf{U}_z(\varphi)\mathbf{U}_x(\vartheta) = \begin{bmatrix} \cos \varphi & -\sin \varphi \\ \sin \varphi & \cos \varphi \end{bmatrix} \cdot \begin{bmatrix} \cos \theta & i \sin \theta \\ i \sin \theta & \cos \theta \end{bmatrix}$$

## S5.2 Decomposition

Let  $(\dagger)$  denote Hermitian transposition. In either system, a rotation by a single operator  $\mathbf{U}(\theta, \varphi) \equiv \mathbf{U}_{zx}(\theta, \varphi)$ , of the form  $\mathbf{U}^\dagger(\theta, \varphi) \cdot \mathbf{X} \cdot \mathbf{U}(\theta, \varphi)$  *cannot* reduce  $\mathbf{Z}(\omega)$  or  $\mathbf{Z}(\omega)$  to diagonal or anti-diagonal forms. The necessary and sufficient condition for a complex matrix  $\mathbf{X}$  to be diagonalizable by a single unitary operator is to be normal (symmetric) so that  $[\mathbf{X}, \mathbf{X}^\dagger] = 0$ . In the general case the impedance tensor is *regular* and depends on eight independent parameters (degrees of freedom/ dimensions), where each of  $\Re\{Z_{ij}\}$  and  $\Im\{Z_{ij}\}$  is assigned with one degree of freedom. Therefore, assuming that (anti)diagonalization could be done with such an operation, it would depend on a maximum of six independent parameters out of the eight existing in the tensor, i.e. four in the two complex principal impedances plus two rotation angles. Therefore, it would be *incomplete*. It follows that exactly two operators  $\mathbf{U}(\theta_1, \varphi_1)$  and  $\mathbf{V}(\theta_2, \varphi_2)$  are required to (anti)diagonalize the impedance tensor, thereby providing an eight parameter set that completely describes it (four in the two complex principal impedance and four rotation angles).

Let us first construct the diagonal (symmetric) decomposition of  $\mathbf{Z}(\omega)$ . The products  $\mathbf{C}_1(\omega) = \mathbf{Z}(\omega)\mathbf{Z}^\dagger(\omega)$  and  $\mathbf{C}_2(\omega) = \mathbf{Z}^\dagger(\omega)\mathbf{Z}(\omega)$  are normal (Hermitian) matrices and constitute mappings of  $\mathbf{Z}(\omega)$  onto  $\mathbb{C}^2$ . Their norms are equal, but  $[\mathbf{C}_1(\omega), \mathbf{C}_2^\dagger(\omega)] \neq \mathbf{0}$  while  $[\mathbf{C}_j(\omega), \mathbf{C}_j^\dagger(\omega)] = \mathbf{0}$ ; thus  $\mathbf{C}_1(\omega)$  and  $\mathbf{C}_2(\omega)$  encode different pieces of the geometrical information originally stored in  $\mathbf{Z}(\omega)$  and as will become clear later on, this pertains to the characteristic coordinate frames of the electric and magnetic field respectively. Moreover, each of  $\mathbf{C}$  depends on only four degrees of freedom, meaning that each can be diagonalized with a single unitary rotation operator of the form (5). Thus,  $\mathbf{C}_1(\omega)$  and  $\mathbf{C}_2(\omega)$  admit *eigenvalue-eigenvector* decompositions of the form

$$\mathbf{C}_1(\omega) = \mathbf{U}(\theta_1, \varphi_1, \omega) \cdot \mathbf{D}(\omega) \cdot \mathbf{U}^\dagger(\theta_1, \varphi_1, \omega) = \mathbf{U}(\theta_1, \varphi_1, \omega) \begin{bmatrix} r_1^2(\omega) & 0 \\ 0 & r_2^2(\omega) \end{bmatrix} \mathbf{U}^\dagger(\theta_1, \varphi_1, \omega) \quad (2a)$$

and

$$\mathbf{C}_2(\omega) = \mathbf{V}(\theta_2, \varphi_2, \omega) \cdot \mathbf{D}(\omega) \cdot \mathbf{V}^\dagger(\theta_2, \varphi_2, \omega) = \mathbf{V}(\theta_2, \varphi_2, \omega) \begin{bmatrix} r_1^2(\omega) & 0 \\ 0 & r_2^2(\omega) \end{bmatrix} \mathbf{V}^\dagger(\theta_2, \varphi_2, \omega) \quad (2b)$$

Now define the complex diagonal tensor

$$\tilde{\mathbf{Z}}(\omega) = \begin{bmatrix} \zeta_1(\omega) & 0 \\ 0 & \zeta_2(\omega) \end{bmatrix}, \quad |\zeta_1(\omega)| > |\zeta_2(\omega)|, \quad \zeta_j(\omega)\zeta_j^*(\omega) = r_j^2, \quad j=1,2$$

to be the *characteristic impedance* or, more precisely, the *eigen-impedance* tensor, so that

$$\tilde{\mathbf{Z}}(\omega)\tilde{\mathbf{Z}}^\dagger(\omega) = \tilde{\mathbf{Z}}^\dagger(\omega)\tilde{\mathbf{Z}}(\omega) = \mathbf{D}(\omega)$$

It follows that

$$\tilde{\mathbf{Z}}(\omega) = \mathbf{U}^\dagger(\theta_1, \varphi_1, \omega) \cdot \mathbf{Z}(\omega) \cdot \mathbf{V}(\theta_2, \varphi_2, \omega) \quad (2c)$$

whence it is straightforward to obtain (2a) and (2b) by direct multiplication. Eq. (2c) is precisely the Singular Value Decomposition of LaTorraca et al. (1986) *and* the Canonical Decomposition of Yee and Paulson (1987).

Now, right multiply Eq. (2c) by  $\mathbf{R}\left(-\frac{\pi}{2}\right) = \begin{bmatrix} 0 & 1 \\ -1 & 0 \end{bmatrix}$  to rotate the eigen-impedance tensor from CS-1 to

CS-2 and on substituting Eq. (1) obtain

$$\tilde{\mathbf{Z}}(\omega)\mathbf{R}\left(-\frac{\pi}{2}\right) = \mathbf{U}^\dagger(\theta_1, \varphi_1, \omega)\mathbf{Z}(\omega)\mathbf{R}\left(\frac{\pi}{2}\right)\mathbf{V}(\theta_2, \varphi_2, \omega)\mathbf{R}\left(-\frac{\pi}{2}\right), \quad (3)$$

with

$$\tilde{\mathbf{Z}}(\omega) = \tilde{\mathbf{Z}}(\omega)\mathbf{R}\left(-\frac{\pi}{2}\right) = \begin{bmatrix} 0 & \zeta_1(\omega) \\ -\zeta_2(\omega) & 0 \end{bmatrix}$$

comprising the eigen-impedance tensor in CS-2. Moreover,

$$\mathbf{R}\left(\frac{\pi}{2}\right)\mathbf{V}(\theta_2, \varphi_2, \omega)\mathbf{R}\left(-\frac{\pi}{2}\right) = \mathbf{R}\left(\frac{\pi}{2}\right)\mathbf{V}_z(\varphi_2, \omega)\mathbf{V}_x(\theta_2, \omega)\mathbf{R}\left(-\frac{\pi}{2}\right)$$

Because  $\mathbf{R}\left(\pm\frac{\pi}{2}\right) \in \text{SO}(2) \subseteq \text{SU}(2)$  and  $\mathbf{V}_z \in \text{SO}(2) \subseteq \text{SU}(2)$ , we have  $\left[\mathbf{R}\left(\pm\frac{\pi}{2}\right), \mathbf{V}_z\right] = 0$ : in a two-dimensional (sub)space the order of successive rotations does not matter. Thus, letting (\*) denote complex conjugation (*without* transposition),

$$\mathbf{R}\left(\frac{\pi}{2}\right)\mathbf{V}(\theta_2, \varphi_2, \omega)\mathbf{R}\left(-\frac{\pi}{2}\right) = \mathbf{V}_z(\varphi_2, \omega)\mathbf{R}\left(\frac{\pi}{2}\right)\mathbf{V}_x(\theta_2, \omega)\mathbf{R}\left(-\frac{\pi}{2}\right) = \mathbf{V}_z(\varphi_2, \omega)\mathbf{V}_x^*(\theta_2, \omega) = \mathbf{V}^*(\theta_2, \varphi_2, \omega)$$

Substituting in eq. (3),

$$\tilde{\mathbf{Z}}(\omega) = \begin{bmatrix} 0 & \zeta_1(\omega) \\ -\zeta_2(\omega) & 0 \end{bmatrix} = \mathbf{U}^\dagger(\theta_1, \varphi_1, \omega)\mathbf{Z}(\omega)\mathbf{V}^*(\theta_2, \varphi_2, \omega) \quad (4)$$

which is the anti-symmetric decomposition of  $\mathbf{Z}(\omega)$  in CS-2 and comprises an adaption of the generalized (complex) SVD to physical systems with anti-symmetric intrinsic geometry. Accordingly, it is referred to as the *Anti-symmetric SVD* or ASVD. It is also interesting to point out that owing to the topology of the  $\text{SU}(2)$  group, the difference between the SVD/CD in CS-1 and the ASVD in CS-2 reduces to a simple inversion in the sense of rotation about the  $x$ -axis!

### S5.3 The characteristic states of the Impedance Tensor.

Let us, henceforth concentrate on the ASVD formulation (4) whence one obtains

$$\mathbf{Z}(\omega) = \mathbf{U}(\theta_1, \varphi_1, \omega) \cdot \tilde{\mathbf{Z}}(\omega) \cdot \left[\mathbf{V}^*(\theta_2, \varphi_2, \omega)\right]^\dagger. \quad (5)$$

The substitution of eq. (5) in  $\mathbf{E}(\omega) = \mathbf{Z}(\omega) \cdot \mathbf{H}(\omega)$  yields

$$\mathbf{U}^\dagger(\theta_1, \varphi_1, \omega) \cdot \mathbf{E}(\omega) = \tilde{\mathbf{Z}}(\omega) \cdot \left[\mathbf{V}^*(\theta_2, \varphi_2, \omega)\right]^\dagger \cdot \mathbf{H}(\omega) \quad (6)$$

For obvious reasons use the notation  $\mathcal{E}(\theta_E, \varphi_E, \omega) \equiv \mathbf{U}(\theta_1, \varphi_1, \omega)$  and  $\mathcal{H}(\theta_H, \varphi_H, \omega) \equiv \mathbf{V}^*(\theta_2, \varphi_2, \omega)$  to summarize the decomposition (4) as

$$\tilde{\mathbf{Z}}(\omega) = \mathcal{E}^\dagger(\theta_E, \varphi_E, \omega) \cdot \mathbf{Z}(\omega) \cdot \mathcal{H}(\theta_H, \varphi_H, \omega). \quad (7)$$

Eq. (6) may be re-written as follows:

$$\mathcal{E}^\dagger(\theta_E, \varphi_E, \omega) \cdot \mathbf{E}(\omega) = \tilde{\mathbf{Z}}(\omega) \cdot \mathcal{H}^\dagger(\theta_H, \varphi_H, \omega) \cdot \mathbf{H}(\omega) \quad (8)$$

The column vectors of the rotation operators  $\mathcal{E}$  and  $\mathcal{H}$  describe rotations of opposite handedness and

constitute, in themselves, orthogonal rotation operators for two-component orthogonal vectors. Denote

$$\mathcal{E}(\theta_E, \varphi_E, \omega) = \left[ \mathbf{e}_1(\theta_E, \varphi_E, \omega) \quad \mathbf{e}_2(\theta_E, \varphi_E + \frac{\pi}{2}, \omega) \right] : \mathbf{e}_i^\dagger \cdot \mathbf{e}_j = \delta_{ij},$$

$$\mathcal{H}(\theta_H, \varphi_H, \omega) = \left[ \mathbf{h}_1(\theta_H, \varphi_H, \omega) \quad \mathbf{h}_2(\theta_H, \varphi_H + \frac{\pi}{2}, \omega) \right] : \mathbf{h}_i^\dagger \cdot \mathbf{h}_j = \delta_{ij}$$

whereupon eq. (8) yields

$$\mathbf{e}_1^\dagger \mathbf{E}(\omega) = \zeta_1(\omega) \cdot \mathbf{h}_2^\dagger \mathbf{H}(\omega) \rightarrow E_1(\theta_E, \varphi_E, \omega) = \zeta_1(\omega) \cdot H_2(\theta_H, \varphi_H, \omega) \quad (9)$$

$$\mathbf{e}_2^\dagger \mathbf{E}(\omega) = -\zeta_2(\omega) \cdot \mathbf{h}_1^\dagger \mathbf{H}(\omega) \rightarrow E_2(\theta_E, \varphi_E, \omega) = -\zeta_2(\omega) \cdot H_1(\theta_H, \varphi_H, \omega) \quad (10)$$

Equation (10) says that  $\mathbf{H}(\omega)$  rotated by  $\mathbf{h}_1^\dagger$  to the direction  $(\theta_H, \varphi_H)$  is mapped onto  $\mathbf{E}(\omega)$  rotated by  $\mathbf{e}_2^\dagger$  to the direction  $(\theta_E, \varphi_E + \pi/2)$  along the most conductive (slow) path inside the 3-D earth. This is the *minimum state* of  $\mathbf{Z}(\omega)$ . Likewise, equation (9) says that  $\mathbf{H}(\omega)$  rotated by  $\mathbf{h}_2^\dagger$  to  $(\theta_H, \varphi_H + \pi/2)$ , is mapped onto  $\mathbf{E}(\omega)$  rotated by  $\mathbf{e}_1^\dagger$  to  $(\theta_E, \varphi_E)$  along the least conductive (fast) path. This corresponds to the *maximum state* of  $\mathbf{Z}(\omega)$ . The mappings can be summarized as follows

$$\begin{bmatrix} E_1(\theta_E, \varphi_E, \omega) \\ E_2(\theta_E, \varphi_E + \frac{\pi}{2}, \omega) \end{bmatrix} = \begin{bmatrix} 0 & \zeta_1(\omega) \\ -\zeta_2(\omega) & 0 \end{bmatrix} \cdot \begin{bmatrix} H_1(\theta_H, \varphi_H, \omega) \\ H_2(\theta_H, \varphi_H + \frac{\pi}{2}, \omega) \end{bmatrix} \Leftrightarrow \tilde{\mathbf{E}} = \tilde{\mathbf{Z}} \cdot \tilde{\mathbf{H}} \quad (11)$$

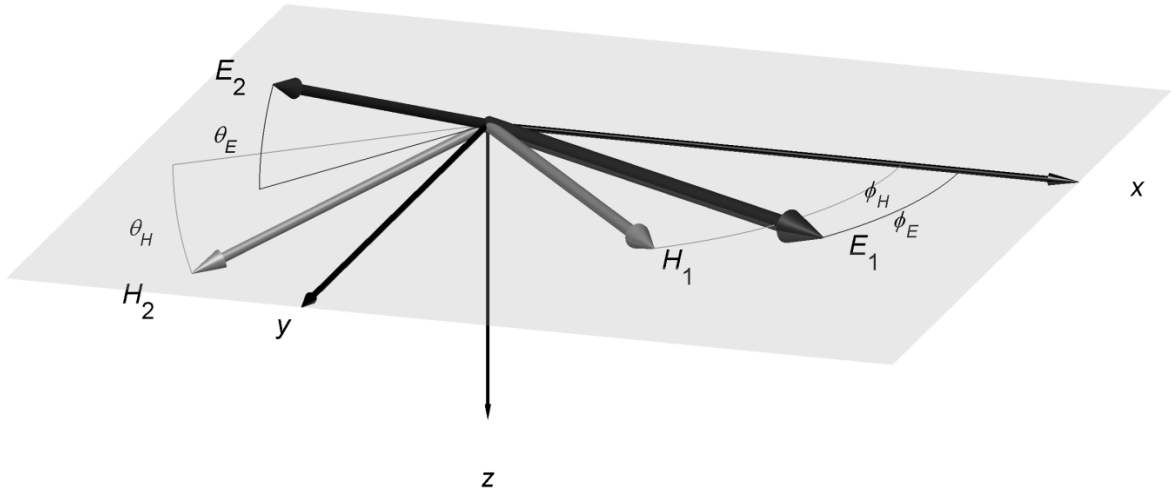


**Figure S4:** Pictorial representation of the characteristic states of the MT impedance tensor. The angles  $(\theta_E, \varphi_E)$  define a *characteristic coordinate frame (eigen-frame)* of the *electric eigen-field*, such that the maximum electric eigen-field ( $E_1$ ) rests at an angle  $\varphi_E$  clockwise with respect to the  $x$ -axis of the experimental coordinate frame, the minimum eigen-field ( $E_2$ ) at an angle  $90^\circ + \varphi_E$  and the plane  $\{E_1, E_2\}$  is tilted by an angle  $\theta_E$  measured clockwise with respect to the horizontal plane  $\{x, y\}$ . The angles  $(\theta_H, \varphi_H)$  define the characteristic eigen-frame of the *magnetic eigen-field* such that the maximum magnetic field ( $H_1$ ) rests at an angle  $\varphi_H$  clockwise with respect to the  $x$ -axis of the experimental coordinate frame, the minimum eigen-field ( $H_2$ ) at an angle  $90^\circ + \varphi_H$  and the plane  $\{H_1, H_2\}$  is tilted by an angle  $\theta_H$  measured clockwise with respect to the horizontal plane.

A pictorial (but simplified) representation of Eq. 17 is shown in Fig. S4. The angles  $(\theta_E, \varphi_E)$  define a *characteristic* coordinate frame or *eigen-frame*  $\{x_E, y_E, z_E\}$  of the *electric eigen-field*  $\tilde{\mathbf{E}}$ , such that  $x_E$  is rotated by  $\varphi_E$  clockwise with respect to the  $x$ -axis of the experimental coordinate frame and the plane  $\{x_E, y_E\}$  is tilted by an angle  $\theta_E$  clockwise with respect to the horizontal plane  $\{x, y\}$ . Likewise, the angles  $(\theta_H, \varphi_H)$  define the characteristic eigen-frame  $\{x_H, y_H, z_H\}$  of the *magnetic eigen-field*  $\tilde{\mathbf{H}}$ , such that  $x_H$  is rotated by  $\varphi_H$  clockwise with respect to the  $x$ -axis of the experimental coordinate frame and the plane  $\{x_H, y_H\}$  is tilted by an angle  $\theta_H$  clockwise with respect to the horizontal plane  $\{x, y\}$ . Each eigen-frame contains orthogonal, *linearly polarized* components. However,  $\varphi_E \neq \varphi_H$  in general and the electric and magnetic eigen-frames are not mutually orthogonal. It follows that in each characteristic state, the associated electric and magnetic eigen-fields are not mutually perpendicular. It is equally important that the electric and magnetic eigen-frames are not horizontal. This should be of no surprise because in 3-D Earth structures the total magnetic and induced electric fields are three dimensional and may be associated with significant gradients, especially in the vicinity of interfaces. Accordingly, they are locally orthogonal and anti-symmetric in complex 3-space and the tilt angles  $\theta_E$  and  $\theta_H$  of the electric and magnetic eigen-frames are a measure of the local landscape of the electric and magnetic field respectively. From eq. (11) it is also apparent that

$$\tilde{\mathbf{Z}}(\omega) = \begin{bmatrix} 0 & \frac{E_1(\theta_E, \varphi_E, \omega)}{H_2(\theta_H, \varphi_H + \frac{\pi}{2}, \omega)} \\ -\frac{E_2(\theta_E, \varphi_E + \frac{\pi}{2}, \omega)}{H_1(\theta_H, \varphi_H, \omega)} & 0 \end{bmatrix}, \quad (12)$$

so that the maximum and minimum eigen-impedances respectively comprise simple ratios of the maximum and minimum states' eigen-fields.

#### S5.4 Nature of the eigen-fields

It is now important to demonstrate how the characteristic states relate to the source (external) and induced (internal) magnetic and electric fields and also to justify the prefix “eigen-” attributed to the characteristic electric and magnetic fields. To this end, following Berdichevsky and Zhdanov (1984) and Egbert (1990), the tangential total magnetic and electric output fields at a given location on the surface of the Earth may be expressed as

$$\mathbf{H}(\omega) = \mathbf{H}_i(\omega) + \mathbf{H}_s(\omega) = [\mathbf{k}_H(\omega) + \mathbf{I}] \cdot \mathbf{H}_s(\omega), \quad (13a)$$

$$\mathbf{E}(\omega) = \mathbf{k}_E(\omega) \cdot \mathbf{H}_s(\omega) \quad (13b)$$

where  $\mathbf{H}_i(\omega)$  is the internal (induced) magnetic field and  $\mathbf{H}_s(\omega)$  is the source (external) magnetic field and  $\mathbf{k}_E(\omega)$ ,  $\mathbf{k}_H(\omega)$  are *excitation operators* that comprise rank 2 transfer functions of two-input, two-output linear systems and represent the electric properties of the Earth. Eq. (13a) yields

$$\mathbf{H}_s(\omega) = [\mathbf{k}_H(\omega) + \mathbf{I}]^{-1} \cdot \mathbf{H}(\omega), \quad (14)$$

whence, by substitution in eq. (13b) the impedance tensor is obtained as

$$\mathbf{Z}(\omega) = \mathbf{k}_E(\omega) \cdot [\mathbf{k}_H(\omega) + \mathbf{I}]^{-1}.$$

For clarity and brevity, denote  $\mathcal{E} \equiv \mathcal{E}(\theta_E, \varphi_E, \omega)$ ,  $\mathcal{H} \equiv \mathcal{H}(\theta_H, \varphi_H, \omega)$ ,  $E_1 \equiv E_1(\theta_E, \varphi_E, \omega)$ ,  $E_2 \equiv E_2(\theta_E, \varphi_E + \pi/2, \omega)$ ,  $H_1 \equiv H_1(\theta_H, \varphi_H, \omega)$  and  $H_2 \equiv H_2(\theta_H, \varphi_H + \pi/2, \omega)$ . On using the ASVD of  $\mathbf{Z}(\omega)$  from eq. (5) and substituting the explicit form of  $\tilde{\mathbf{Z}}(\omega)$  from eq. (12), one may see that

$$\mathbf{E} = \mathcal{E} \begin{bmatrix} 0 & E_1 \\ -E_2 & 0 \end{bmatrix} \cdot \begin{bmatrix} H_1^{-1} & 0 \\ 0 & H_2^{-1} \end{bmatrix} \cdot \mathcal{H}^\dagger \mathbf{H}.$$

This can be further developed to yield

$$\mathbf{E} = \left( \mathcal{E} \begin{bmatrix} 0 & E_1 \\ -E_2 & 0 \end{bmatrix} \mathcal{H}^\dagger \right) \cdot \left( \mathcal{H} \begin{bmatrix} H_1^{-1} & 0 \\ 0 & H_2^{-1} \end{bmatrix} \cdot \mathcal{H}^\dagger \mathbf{H} \right).$$

Therefore, letting

$$\mathbf{k}_E(\omega) = \mathcal{E} \begin{bmatrix} 0 & E_1 \\ -E_2 & 0 \end{bmatrix} \mathcal{H}^\dagger, \quad (15a)$$

one obtains

$$\mathbf{k}_E(\omega) \cdot \mathbf{k}_E^\dagger(\omega) = \mathcal{E} \begin{bmatrix} E_1^2 & 0 \\ 0 & E_2^2 \end{bmatrix} \mathcal{E}^\dagger, \quad E_j^2 = E_j E_j^*, \quad j=1,2,$$

which shows that the electric eigen-fields are the characteristic values of  $\mathbf{k}_E(\omega)$  and, at the same time, eigen-values of the electric field. Also letting

$$[\mathbf{k}_H(\omega) + \mathbf{I}]^{-1} = \mathcal{H} \begin{bmatrix} H_1^{-1} & 0 \\ 0 & H_2^{-1} \end{bmatrix} \cdot \mathcal{H}^\dagger \quad (15b)$$

shows that the magnetic eigen-fields are the eigenvalues of  $[\mathbf{k}_H(\omega) + \mathbf{I}]$ , namely the eigenvalues of the total magnetic field.

### S5.5 Elliptical polarization

It is important to point out that the *projection* of the electric and magnetic eigen-frames on the *horizontal plane* generates elliptically polarized field components. The rotation  $\mathcal{E}^\dagger(\theta_E, \varphi_E)\mathbf{E}$  is written as:

$$\begin{bmatrix} E_1 \\ E_2 \end{bmatrix} = \begin{bmatrix} (E_x \cos \varphi_E + E_y \sin \varphi_E) \cos \theta_E - i(E_x \sin \varphi_E - E_y \cos \varphi_E) \sin \theta_E \\ -(E_x \sin \varphi_E - E_y \cos \varphi_E) \cos \theta_E + i(E_x \cos \varphi_E + E_y \sin \varphi_E) \sin \theta_E \end{bmatrix}. \quad (16)$$

For a given  $\theta_E$ , the variation of the azimuthal angle  $\varphi_E$  forces the rotating field vector to trace an ellipse on the *horizontal* frame  $\mathbf{x} \pm i\mathbf{y}$ , so that the normalized vector will have a major axis equal to  $\cos \theta_E$  and a minor axis equal to  $\sin \theta_E$ . The ratio of the minor to the major axis is the *ellipticity*, given by  $b_E = \tan \theta_E$ . The same holds for the rotation of the magnetic field vector so that  $b_H = \tan \theta_H$ . In either case  $\theta > 0$  implies a counter-clockwise sense of rotation and  $\theta < 0$  a clockwise sense. Thus, ellipticity on the horizontal plane is defined in terms of a rotation in higher dimensional space! This also provides a heuristic means of determining bounds for the variation for  $\theta_E$  and  $\theta_H$ : they are  $-\pi/4 \leq \theta_E \leq \pi/4$  and  $-\pi/4 \leq \theta_H \leq \pi/4$ , because in a given ellipse, the range of the minor axis is bounded by the maximum value of the major axis.

## S6. Characteristic State analysis and Induction Vectors of a Typical Magnetotelluric Sounding.

Fig. S5a-d shows an example of the ASVD decomposition applied to the typical Sounding 151 which is located approximately 750m east of Akrotiri town. Estimation uncertainties are “acceptable” but the Earth response is not smooth, especially at periods longer than 1s. This is attributed to high levels of coherent noise that cannot be suppressed by single-site robust estimation methods. Moreover, it has not been possible to reliably estimate the tensor at any at period longer than 10s. Some residual effects of interference by the power distribution grid are evident near 0.01s (first harmonic) and 0.04s (first sub-harmonic) in both the phase and strike angle functions (Fig. S5b and S5c respectively).

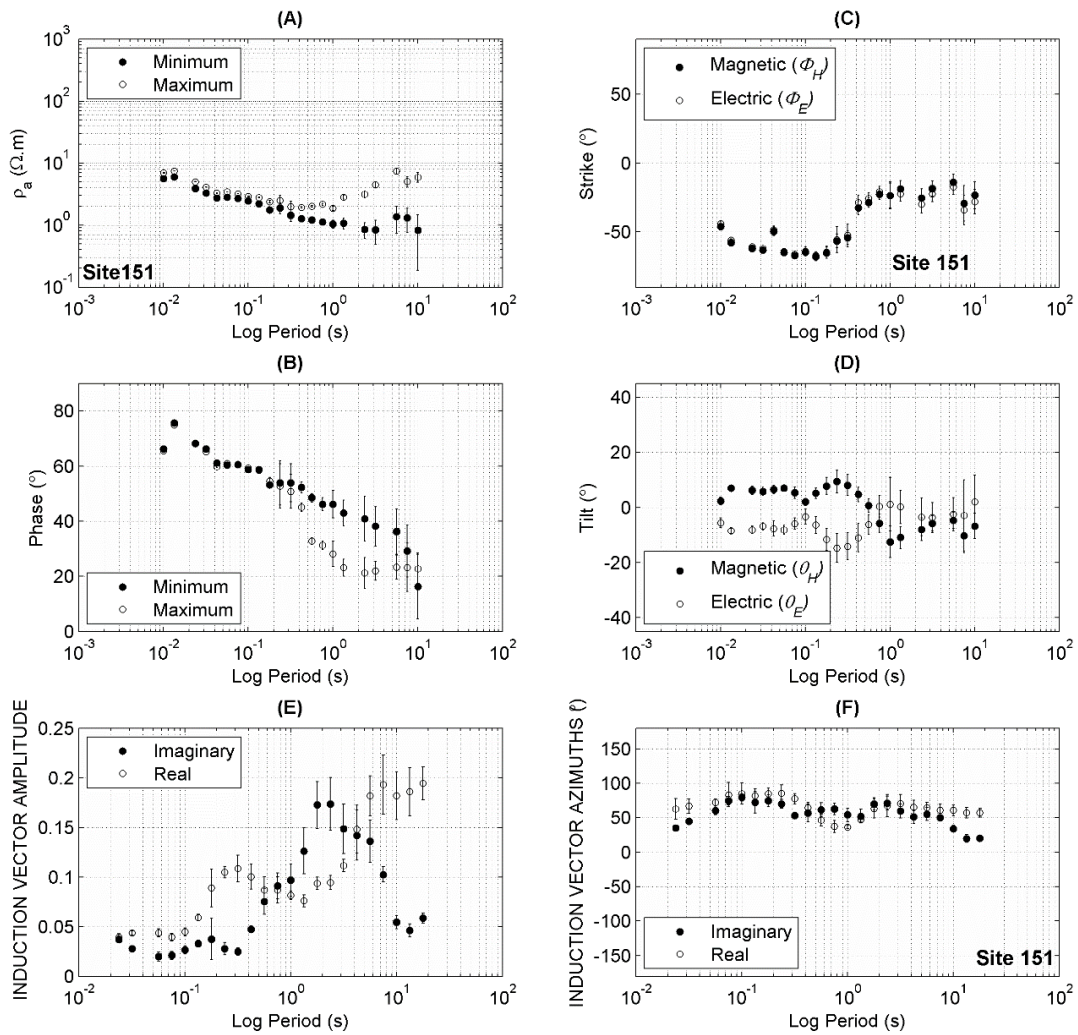


**Figure S5:** Panels (a)-(d) demonstrate the characteristic states of the impedance tensor measured at the Site 151, east of Akrotiri town (see Fig. 7 of main article); (a) apparent resistivities and (b) phases derived from the maximum and minimum impedances; (c) azimuths of the maximum and minimum characteristic states; (d) tilt angles (ellipticities) of the characteristic states. Panel (e) illustrates the amplitudes and (f) the azimuths of the real and imaginary induction vectors.

The electric ( $\Phi_E$ ) and magnetic ( $\Phi_H$ ) strike angles coincide and they both rotate from approximately  $-60^\circ$  (N300°) when  $T < 0.2s$  to approximately  $-25^\circ$  (N335°) when  $T > 0.5s$  (Fig. S5c). At the same time, the

ellipticities exhibit local extremes ( $\theta_E=-14^\circ$  and  $\theta_H=9.4^\circ$  at  $T=0.24s$ , see Fig. S5d), while the maximum and minimum apparent resistivity and phase curves split. All this is evidence of (weak) three-dimensionality associated with a clockwise rotation of the dominant geoelectric strike from a shallow/local N300° to a deeper/broader N335°. Such behaviour is observed throughout the SVC. At periods longer than 1s the ellipticities are generally less than  $-5^\circ$  and the strike angles very comparable, thus demonstrating the predominantly 2-D nature of the deeper geoelectric structure.

The Induction Vectors obtained at Site 151 are shown in Fig. S5e-f. They apparently sense the rotation of the local geoelectric strike in the interval 0.2s – 0.8s, as evident in the variation of their amplitudes and azimuths. In addition, their azimuths indicate that the Real and Imaginary IVs are practically parallel. For periods longer than 2s the azimuth of the Real IV is approx. N55° and nearly at right angles to the electric strike angle  $\Phi_E$  (~N335°), consistently with a NNW-SSE dominantly two-dimensional local geoelectric structure.

## S7. Regional Geoelectric Strike by Simultaneous Analysis of the Impedance Tensor Ensemble

Banks and Wright (1998) proposed a “holistic” approach to the determination of *regional* geoelectric structural trends, based on the simultaneous analysis of all impedance tensor observations. These authors expand on the fact that the presence of a regional two-dimensional structure will manifest itself in the common phase of impedance tensor elements belonging to the same column vector; these are the electric fields produced by a unit magnetic field parallel or perpendicular to the regional strike. Accordingly, if a group of MT soundings shares the same regional response, the real and imaginary parts of electric fields rotated to the direction of the regional response will plot on a line of constant phase in the complex plane, regardless of the amount of distortion experienced by individual soundings. Conversely, the direction parallel to which we find the best of all straight lines fitted to the real vs. imaginary parts indicates the direction of the regional strike.

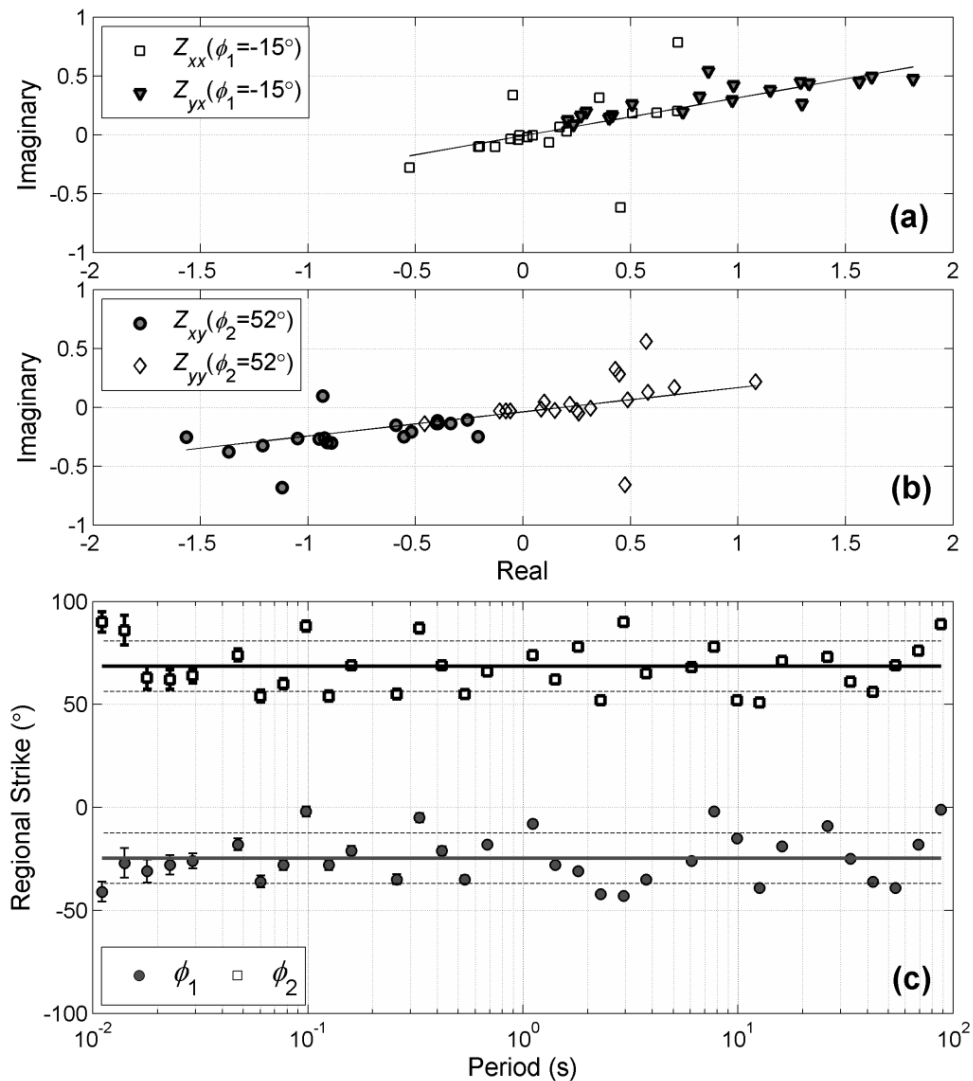


**Figure S6:** Determination of the regional strike from the MT Tensor Impedance data after Banks and Wright (1998). **(a)** The best fitting of all straight lines fitted to the Argand diagram of the rotated elements  $Z_{xx}(\omega_n, \phi) \cup Z_{yx}(\omega_n, \phi)$  for the frequency  $f_i = 0.1012\text{Hz}$ ; it is found at the direction of N345°. **(b)** The same for the rotated elements  $Z_{xy}(\omega_n, \phi) \cup Z_{yy}(\omega_n, \phi)$ ; the direction here is N52°. **(c)** The frequency dependent regional strike angles  $\phi_1$  and  $\phi_2$ .

This concept is implemented by rotating all observed impedance tensors  $\mathbf{Z}(\omega_n)$  by an angle  $\phi_t(\omega_n) = \phi_{t-1}(\omega_n) + \Delta\phi$ ,  $\phi_t \in [-90^\circ, 90^\circ]$  and fitting a straight line to the ensembles of the Argand diagrams formed by all left column vector elements  $\{Z_{xx}(\omega_n, \phi_t)\} \cup \{Z_{yx}(\omega_n, \phi_t)\}$  on one hand, and all right column vector elements  $\{Z_{xy}(\omega_n, \phi_t)\} \cup \{Z_{yy}(\omega_n, \phi_t)\}$  on the other. In either case, the angle  $\phi_M(\omega_n)$  at which the minimum of all misfits is found should be the direction at which the elements of each column vector have the same (regional) phase  $\psi_M(\omega_n)$ ; the regional phase is the arctangent of the best fitting of all lines. As illustrated in Fig. S6a and S6b, at the frequency  $f_n = 0.1012\text{Hz}$ , the best fitting of all lines is found at the direction  $\phi_1 = \text{N-}15^\circ$  ( $\text{N}345^\circ$ ) for the ensemble  $\{Z_{xx}(\omega_n, \phi_1)\} \cup \{Z_{yx}(\omega_n, \phi_1)\}$  and at the direction  $\phi_2 = \text{N}52^\circ$  for the ensemble  $\{Z_{xy}(\omega_n, \phi_2)\} \cup \{Z_{yy}(\omega_n, \phi_2)\}$ . By repeating the procedure over all frequencies one may derive the frequency dependent curve of the strike directions  $\phi_1$  and  $\phi_2$ , as shown in Fig. S6c. It is apparent that the regional strike curves  $\phi_1(T)$  and  $\phi_2(T)$  are not smooth functions, which is rather understandable given the high level of ambient noise. However, both curves vary randomly about the expectation  $\langle\phi_1(T)\rangle = 24.73^\circ \pm 12.26^\circ$  (roughly  $\text{N}335^\circ$ ) and  $\langle\phi_2(T)\rangle = 68.52^\circ \pm 12.21^\circ$  (roughly  $\text{N}70^\circ$ ). Evidently,  $\langle\phi_1(T)\rangle$  is almost perpendicular to  $\langle\phi_2(T)\rangle$  as would have been expected of two-dimensional structures. Moreover,  $\langle\phi_1(T)\rangle$  compares very well to the average geoelectric strike determined by spatial analysis of individual impedance tensors (see main article).

## S8. Residuals Analysis of 2-D Magnetotelluric Modelling at Akrotiri Peninsula.

Fig. S7 compares the observed and residual apparent resistivities (top row) and phases (bottom row) of all TE (left column) and TM (right column) data used for construction of the 2-D electric resistivity model shown in Fig. 9 of the main article. The model was obtained by 2-D joint TE/TM mode inversion along a 4.3km profile of approx. W-E orientation between sites 091 and 121 (Akrotiri peninsula, see Fig. 7 of main article); inversion was carried out with the algorithm of Rodi and Mackie (2001). The quality of the solution is marginal in terms of the  $\chi^2$  metric: while  $E\{\chi^2\} = 348$ , the observed value was almost twice as high ( $\chi^2 \cong 664$ ). However, the fractional error is only 6.77% and the goodness of fit  $R^2=0.93$ . In Fig. S7, the 8 soundings used in the inversion are plotted sequentially, hence the jagged appearance of the “observed data” curves in which high apparent resistivities and phases generally correspond to higher frequencies and lows resistivities/phases to lower frequencies. It is also evident that large residuals are few and as easily verifiable, mostly associated with the highest frequencies which are more heavily distorted by ambient (mains) noise. Accordingly and in terms of “expert judgement”, the model is useful for interpretation.

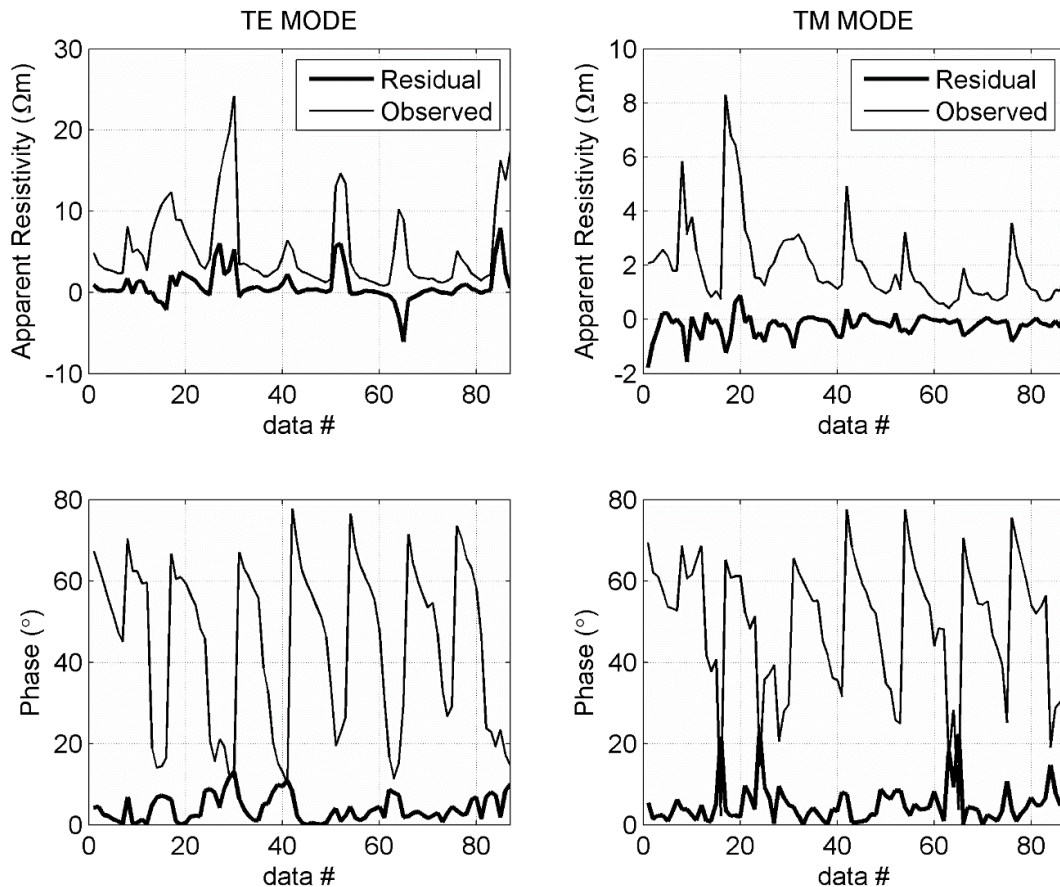


**Figure S7.** Comparison of the observed and residual apparent resistivities (top row) and phases (bottom row) of all TE (left column) and TM (right column) data used in the construction of the electric resistivity model shown in Fig. 9 of the main article.

### S9. Typical Example of 1-D Inversion at North Thera.

As stated in the main article the electric structure of the SVC is not resolvable at depths greater than 3km, presumably because the very high near-surface conductivity severely attenuates the magnetotelluric field and reduces the depth of penetration. In addition to the 2-D resistivity section presented in the main article, this assertion is corroborated by one-dimensional inversions in the Oia – Cape Columbo and Vourvoulos areas. A typical example is shown in Fig. S8, of the sole MT sounding available in the vicinity of Vourvoulos (Fig. 8 of main article), for which the trace invariant (or average, or Berdichevsky) of the impedance tensor

$$Z = (Z_{xy} - Z_{yx})/2$$

was inverted with the Jupp and Vozoff (1975) scheme. The fractional error associated with the solution is 5.72% and the goodness of fit ( $R^2$ ) is 0.98. Sea level is located at approx. 70m below the surface. It is quite clear that resistivity is relatively high ( $>100\Omega\text{m}$ ) down to approx. 95m and thereafter drops by 1 – 2 orders of magnitude and remains at such levels for at least several kilometres, gradually increasing with depth.

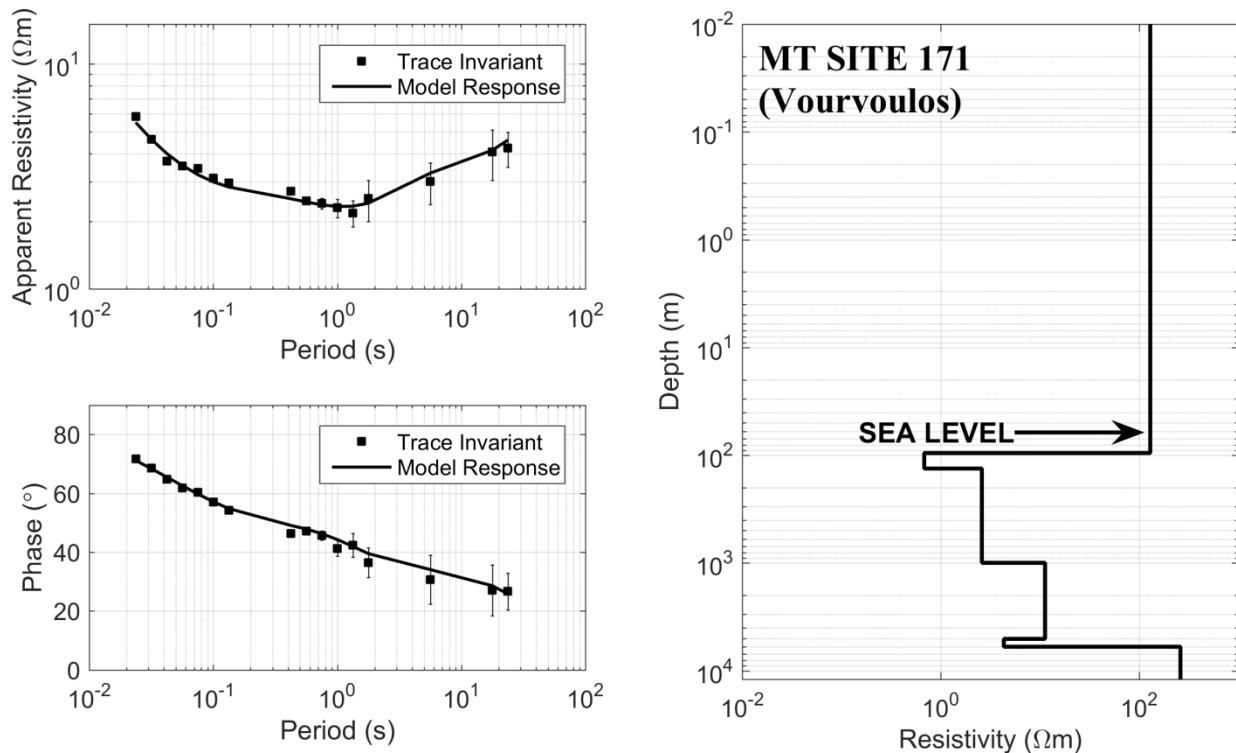


**Figure S8:** One dimensional inversion of the trace invariant impedance measured in the vicinity of Vourvoulos town, north Thera; the inversion was performed with the efficient algorithm of Jupp and Vozoff (1975).

### S10. DGPS Modelling: Misfit obtained for the 1×1 km discretization scheme.

The fault model is shown in Fig. S9 as well as in Fig. 16 of the main article. It comprises: **(i)** One oblique-slip fault labelled AB, almost coincident with the Trans-Santorin Divide; it has  $\varphi = N331^\circ \pm 5^\circ$ ,  $\delta = 85^\circ \pm 10^\circ$ , a width of 6km and total length of 16km (from Vlychada, through the Nea and Palaea Kammeni channel to exactly east of Therassia islet). The net slip along the fault plane was constrained by the maximum displacements observed along the TSD during 1994-2005: the strike-slip component was allowed to vary between 10mm left-lateral and 30mm right lateral and the dip-slip component was allowed to vary between 0mm and 20mm down-dip (normal fault). **(ii)** A zone of two parallel oblique-slip faults labelled CD and EF, respectively coincident with the Cape Columbo (CCF) and Mikros Prof. Elias (MPEF) faults; they both  $\varphi = N47^\circ \pm 3^\circ$ ,  $\delta = 80^\circ \pm 5^\circ$ , width of 6km and total length of 9km. The net slip was also constrained by the maximum displacements observed in the vicinity of the CFZ, but the strike-slip component was allowed to vary between 30mm left-lateral and 30mm right-lateral, while the dip-slip component from 30mm up-dip (thrust) to 30mm down-dip (normal).

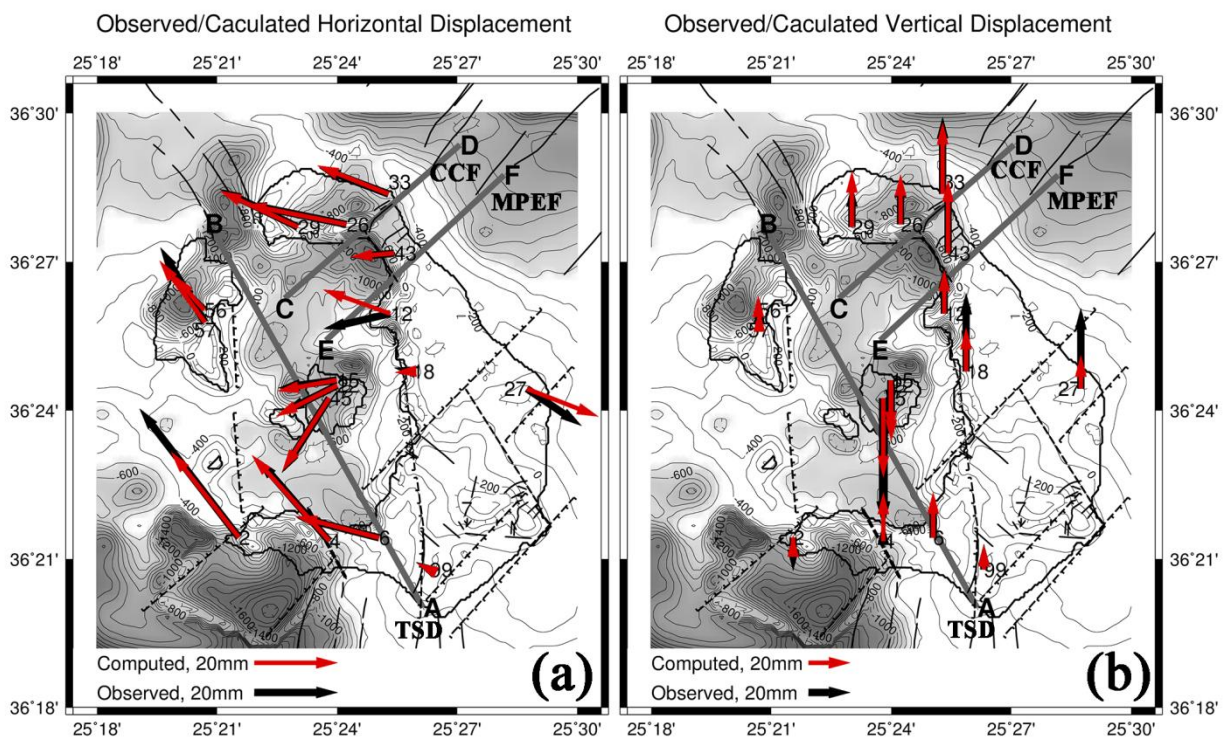


**Figure S9:** Observed (black) and computed (red) displacement vectors for **(a)** the horizontal and **(b)** the vertical displacement field over the period 1994-2005 and relative to Station 7. The computed (red) displacement field is based on a 1×1 km tiling scheme and comprises the combined action of faults AB (TSD), CD (CCF) and EF (MPEF). All displacement vectors are superimposed on the model of the surface of the Alpine basement. Solid black lines indicate the traces of mapped (known) faults. Dashed lines mark the traces of inferred faults with throw/dip direction indicated when possible.

In all cases a small tensile component of  $\pm 1$ mm was allowed, although it did not affect the results. The width of the faults was determined by our estimation of the local thickness of the schizosphere (see main article for details). As the distribution of slip on real fault planes is not uniform, the model fault planes were tiled so as to comprise 1×1 km arrays with each tile allowed to slip on its own. To obtain physically

meaningful results, tiles were not allowed to slide independently but constrained by the dislocation of their neighbours so as to ensure smooth variation of slip across the fault plane. This is possible by the regularization or smoothing factor  $k$ , which determines the degree of independence between adjacent tiles and regulates the roughness of the fault model. In the solution shown herein,  $k=1000$  and was adopted on the basis that it yielded an acceptable RMS misfit at the inflection of the curve tracing the trade-off between model roughness and misfit. The observed (black) and calculated (red) horizontal displacement vectors are shown in Fig. S9a, and the corresponding vertical displacement vectors in Fig. S9b. The fit is excellent and very similar to the one obtained for the coarser discretized fault planes and shown in Fig. 13 of the main article, so that absolutely analogous comments should apply.

## S11. Additional references

- Arfken, G.B. and Weber, H.J., 1985. *Mathematical methods for physicists*, 6th edition, Elsevier – Academic Press.
- Berdichevsky, M. N. and Zhdanov, M. S., 1984. *Advanced Theory of Deep Geomagnetic Sounding*, Elsevier, Amsterdam, pp 136-155.
- Chailas, S. and Lagios, E., 1996. Monitoring of the Local Gravity Field in Santorin Volcano, 1984-1995. Volcanoes of Europe, in Proceedings of the 2nd workshop on European laboratory volcanoes 2-4 May 1996, Santorin, Greece, 297-309.
- Egbert, G.D., 1990. Comments on 'Concerning dispersion relations for the magnetotelluric impedance tensor' by E. Yee and K. V. Paulson, *Geophys. I. Int.*, 102, 1-8.
- Jupp D.L.B. and Vozoff K., 1975. Stable Iterative Methods for the Inversion of Geophysical Data, *Geophys. J. Int.*, 42 (3), 957–976. Doi: <https://doi.org/10.1111/j.1365-246X.1975.tb06461.x>
- Lagios, E. 1995. High precision study of gravity variations over Thera Volcano, Greece. Proc. Intern. Workshop "New Challenges for Geodesy in Volcanoes Monitoring", June 14-16 (1993), Walferdange, Luxemburg. Tire a part des Cahiers du Centre Europeen de Geodynamique et de Seismologie, Vol. 8, 293-305.
- Lagios, E., Drakopoulos J., Hipkin, R.G., Gizeli, C. 1988. Microgravimetry in Greece: applications to earthquake and Volcano - eruption prediction. *Tectonophysics*, 152, 197-207.
- Lagios, E., Tzanis, A., Hipkin, R.G., Delibasis, N., Drakopoulos, J. 1989. Surveillance of Thera Volcano - Monitoring of the local gravity field. Proc. 3rd Intern. Congr. "Thera and the Aegean World", Sept. 3-9, Santorini, Greece, Vol. 2, 216-223.
- LaTorraca G., Madden T. and Korringa J., 1986. An analysis of the magnetotelluric impedance tensor for three-dimensional structures. *Geophysics*. 51, 1819–1829.
- Normand, J.M., 1980. *A Lie Group: Rotations in Quantum Mechanics*, North-Holland, Amsterdam.
- Rose, M.E., 1957. *Elementary theory of angular momentum*, Wiley, New York.
- Wigner, E.P., 1959. *Group theory and its applications to the Quantum Mechanics of atomic spectra*, Academic Press, New York.
- Yee, E. and Paulson K.V., 1987. The canonical decomposition and its relationship to other forms of magnetotelluric impedance tensor analysis. *J. Geophys.*, 61, 173–189.